

Abstract

Measurement of the ν_μ charged current π^+ to quasi-elastic cross section ratio on mineral oil in a 0.8 GeV neutrino beam

Steven K. Linden

2011

Charged current single pion production ($CC\pi^+$) and charged current quasi-elastic scattering ($CCQE$) are the most abundant interaction types for neutrinos at energies around 1 GeV, a region of great interest to oscillation experiments. The cross-sections for these processes, however, are not well understood in this energy range. This dissertation presents a measurement of the ratio of $CC\pi^+$ to $CCQE$ cross-sections for muon neutrinos on mineral oil (CH_2) in the MiniBooNE experiment. The measurement is presented here both with and without corrections for hadronic re-interactions in the target nucleus and is given as a function of neutrino energy in the range $0.4 \text{ GeV} < E_\nu < 2.4 \text{ GeV}$. With more than 46,000 $CC\pi^+$ events collected in MiniBooNE, and with a fractional uncertainty of roughly 11% in the region of highest statistics, this measurement represents a dramatic improvement in statistics and precision over previous $CC\pi^+$ and $CCQE$ measurements.

Measurement of the ν_μ charged current π^+ to
quasi-elastic cross section ratio on mineral oil in a
0.8 GeV neutrino beam

A Dissertation
Presented to the Faculty of the Graduate School
of
Yale University
in Candidacy for the Degree of
Doctor of Philosophy

by
Steven K. Linden

Dissertation Director: Bonnie Fleming

2010

Contents

| | | |
|----------|--|-----------|
| 1 | Introduction | 4 |
| 1.1 | Outline | 4 |
| 1.2 | The History of Neutrinos | 5 |
| 1.3 | Neutrinos in the Standard Model | 7 |
| 1.4 | Neutrinos Masses and Mixing | 11 |
| 1.5 | Neutrino Cross-sections | 15 |
| 1.5.1 | Charged Current π^+ Production | 16 |
| 1.5.2 | Charged Current Quasi-Elastic Scattering | 22 |
| 1.5.3 | Neutrino Cross-section Measurements | 24 |
| 1.6 | The $CC\pi^+$ to $CCQE$ Ratio | 25 |
| 2 | The MiniBooNE Experiment | 28 |
| 2.1 | The Booster Neutrino Beam | 29 |
| 2.2 | The MiniBooNE Detector | 32 |
| 2.2.1 | PMTs and Mineral Oil | 32 |
| 2.2.2 | Electronics and Data Acquisition | 35 |
| 2.2.3 | Calibration | 38 |
| 3 | Event Simulation | 41 |
| 3.1 | Neutrino Flux Prediction | 41 |
| 3.2 | NUANCE | 46 |

| | | |
|----------|--|-----------|
| 3.3 | Detector Simulation | 47 |
| 4 | Event Reconstruction | 53 |
| 4.1 | Events and Sub-events | 53 |
| 4.2 | The S-Fitter | 55 |
| 4.2.1 | Fast Fit | 56 |
| 4.2.2 | Full Fit | 57 |
| 4.2.3 | Flux Fit | 58 |
| 4.2.4 | Electron-like and Muon-like Sub-events | 59 |
| 4.3 | The P-Fitter | 59 |
| 4.4 | Reconstruction of Event Kinematics | 62 |
| 5 | $CC\pi^+$ to $CCQE$ Cross Section Ratio | 64 |
| 5.1 | Analysis Method | 64 |
| 5.2 | Observed and FSI-Corrected Ratios | 66 |
| 5.3 | Event Selection | 69 |
| 5.4 | Signal Fraction and Cut Efficiency | 72 |
| 5.5 | Neutrino Energy Unfolding | 76 |
| 5.6 | Systematic Uncertainties | 85 |
| 5.6.1 | Cross section and flux uncertainties | 88 |
| 5.6.2 | Optical model uncertainties | 94 |
| 5.6.3 | Additional unisims | 96 |
| 5.6.4 | Total Uncertainties | 96 |
| 5.7 | Cross-checks | 98 |
| 5.7.1 | Alternative Cuts | 98 |
| 5.7.2 | Alternative Energy Reconstructions | 100 |
| 5.7.3 | Q^2 Reweighting | 113 |
| 5.7.4 | Pion Momentum | 116 |
| 5.7.5 | Nucleon Momentum | 116 |

| | |
|-----------------------|------------|
| 5.8 Results | 122 |
| 6 Conclusion | 135 |

Chapter 1

Introduction

1.1 Outline

This thesis presents a measurement of the ratio of neutrino $CC\pi^+$ to $CCQE$ cross-sections. Sections 1.2, 1.3, and 1.4 present an overview of the neutrino: the history of its discovery (1.2), its place in the Standard Model of particle physics (1.3), and open questions concerning it that lead beyond the Standard Model (1.4). Section 1.5 introduces the two interactions with which the present analysis is concerned, discusses the standard ways of modelling these interactions, and briefly reviews our current experimental knowledge of these quantities. Section 1.6 addresses the importance of the measurement presented here, the ratio of the $CC\pi^+$ and $CCQE$ cross-sections.

Chapters 2-4 discuss the technology, software, and analysis tools used in making the ratio measurement. The physical setup of the MiniBooNE experiment, including both the Booster Neutrino Beam (BNB) and the MiniBooNE detector, is discussed in chapter 2. Chapter 3 discusses the Monte Carlo (MC) simulation of the neutrino beam, neutrino interactions in the detector, and the detector response. This simulation provides predictions for various quantities that are used in the analysis. Chapter 4 discusses the algorithms used to reconstruct neutrino events from the raw data and obtain kinematic information for each event.

The ratio analysis itself is discussed in chapter 5. Section 5.1 presents an overview of the method used to extract the cross-section ratio. In section 5.2, the ratio we measure is more precisely defined, and the observed and FSI-corrected ratios are distinguished. The selection of $CC\pi^+$ and $CCQE$ event samples is discussed in section 5.3. Sections 5.4 and 5.5 cover the correction factors obtained from MC: the signal fractions, cut efficiencies, and energy unfolding matrix. Calculation of the systematic uncertainties on the ratio is discussed in section 5.6. Section 5.7 goes through a number of studies and alternative analyses that were performed as checks that the main analysis is adequate. The results of the main analysis are presented in section 5.8. Chapter 6 offers some concluding remarks on the measurement and its importance in the wider field of neutrino physics.

1.2 The History of Neutrinos

When nuclear beta decay was first studied in the 1910s and 1920s, it raised two puzzles. First, the energy spectrum of the emitted electron was found to be continuous; however, for a two-body decay energy conservation required the spectrum to be discrete. Second, the decay appeared not to conserve angular momentum. In 1930, Wolfgang Pauli proposed what he called a “desperate remedy” for these problems: that in addition to an electron, beta decay produced an undetected neutral particle that carried the missing energy and angular momentum. In 1932, James Chadwick discovered the neutron [1]; however, Chadwick’s particle was too massive to be the particle hypothesized by Pauli. In 1934, Hans Bethe and Rudolf Peierls calculated an upper limit on the cross section of Pauli’s neutral particle of about 10^{-34} cm² [2], which rendered it undetectable by conventional means. The idea of an undetectable particle caused great uneasiness in the empirically-minded physics community, not least to Pauli himself, is reported to have said: “I have done a terrible thing, I have postulated a particle that cannot be detected”. Nonetheless, this solution was accepted in order to preserve energy conservation as a fundamental property of nature. The particle was dubbed the “neutrino” by Enrico Fermi, who developed the

first model of weak interactions [3]. Fermi’s model included the neutrino, thus putting the particle, which had formerly been an *ad hoc* addition to the particle zoo, on firmer theoretical footing.

Neutrinos were first detected by Clyde Cowan and Frederick Reines in 1956 [4] (much to the relief of Wolfgang Pauli, who died just two years later). Cowan and Reines used a tank of water lined with scintillating material to detect anti-neutrinos produced by a nuclear reactor. The anti-neutrinos interacted with protons in the water to produce neutrons and positrons. A neutron from the reaction would subsequently be captured by a nucleus, emitting a photon; a positron would annihilate with an electron in the water, producing a pair of photons. These photons stimulated light emission from the scintillators, which was then detected by photomultiplier tubes. The coincidence of the signals from the positron annihilation and the neutron capture indicated an anti-neutrino event.

In 1962, the detection of muon neutrinos by Leon Lederman, Melvin Schwartz, and Jack Steinberger demonstrated that multiple “flavors” of neutrino exist [5]. When the tau lepton was discovered at SLAC in the 1970s, a corresponding third flavor of neutrino was also proposed. The tau neutrino was eventually observed by the DONUT collaboration in 2000 [6].

Neutrinos produced by the nuclear reactions that power the sun (solar neutrinos) were observed by Ray Davis at Homestake in the 1960s [7]. In the Homestake experiment, neutrinos were captured on chlorine nuclei, producing an isotope of argon; these argon atoms could then be extracted from the tank and counted. The flux of solar neutrinos measured by Davis was consistently about a third of the flux predicted by John N. Bahcall in the standard solar model [8]. This became known as the “solar neutrino problem”; it is now understood to be the first hint that neutrinos oscillate.

Further evidence for neutrino oscillations was found in 1988 by the Kamiokande experiment [9], which observed a deficit of muon neutrinos from atmospheric cosmic ray interactions; this deficit was confirmed in 1992 by the IMB experiment [10]. The successor to Kamiokande was the Super-Kamiokande experiment, which in 1998 found strong evi-

dence for muon neutrino oscillations [11, 12]. Evidence for the oscillation of solar neutrinos was seen by the Kamiokande-II [13], GALLEX [14], SAGE [15], and SNO [16] experiments; their findings were consistent with the hypothesis that the solar neutrino problem is due to neutrino oscillations. The discovery of these flavor-changing oscillations has led to a vigorous and diverse research program in neutrino physics over the past decade, aimed at understanding the oscillations and their implications.

1.3 Neutrinos in the Standard Model

The Standard Model (SM) is a quantum field theory with the symmetry group:

$$U(1) \times SU(2) \times SU(3) \tag{1.1}$$

The $SU(3)$ group, associated with the conserved color charge, corresponds to the strong force; the $U(1)$ group, associated with weak hypercharge, and the $SU(2)$ group, associated with weak isospin, together correspond to the unified electroweak force.

The SM contains twelve spin- $\frac{1}{2}$ fermions and twelve spin-1 gauge bosons. The gauge bosons of the SM are eight gluons, which mediate the strong interaction, one photon, mediating the electromagnetic interaction, and three intermediate vector bosons (the W^\pm and the Z^0), mediating the weak interaction. The fermions in the SM are six quarks, which couple to all three of the fundamental forces, three charged leptons, which couple to the electromagnetic and weak forces, and three neutral leptons, the neutrinos, which couple only to the weak force. The SM also includes a single scalar (spin-0) particle, the Higgs boson, which is associated with spontaneous electroweak symmetry breaking and is the only SM particle that remains undetected. Every particle is also expected to couple to the graviton, which carries the gravitational force, but this coupling is not part of the SM.

The electroweak Lagrangian after symmetry breaking can be written as the sum of several terms:

$$\mathcal{L}_{EW} = \mathcal{L}_K + \mathcal{L}_{Higgs} + \mathcal{L}_{Gauge} + \mathcal{L}_{HG} + \mathcal{L}_{Yukawa} + \mathcal{L}_{NC} + \mathcal{L}_{CC} \quad (1.2)$$

\mathcal{L}_K contains the kinetic terms, \mathcal{L}_{Higgs} contains the three-point and four-point self-interactions of the Higgs boson, \mathcal{L}_{Gauge} contains the three-point and four-point self-interactions of the gauge bosons, \mathcal{L}_{HG} contains the coupling of the Higgs boson with the gauge bosons, \mathcal{L}_{Yukawa} contains the Yukawa coupling of the Higgs boson with the fermions, and \mathcal{L}_{NC} and \mathcal{L}_{CC} contain the neutral current and charged current couplings, respectively, of the fermions with the gauge bosons.

The neutral current coupling term is:

$$\mathcal{L}_{NC} = e J_\mu^{em} A^\mu + \frac{g}{\cos \theta_W} (J_\mu^3 - \sin^2 \theta_W J_\mu^{em}) Z^\mu \quad (1.3)$$

where g is the weak coupling constant, θ_W is the Weinberg (weak mixing) angle, e is the charge of the electron, A represents the gauge field associated with the photon, and Z represents the gauge field associated with the Z^0 . J_μ^{em} and J_μ^3 are the electromagnetic and neutral weak currents, defined as:

$$J_\mu^{em} = \sum_f q_f \bar{f} \gamma_\mu f \quad (1.4)$$

$$J_\mu^3 = \sum_f I_f \bar{f}_L \gamma_\mu f_L \quad (1.5)$$

where f are the spinors representing the fermions of the Standard Model, γ_μ are the Dirac matrices, q_f is the electric charge of the fermion f , and I_f is its weak isospin. The subscript L denotes the left-handed component of a spinor, which can be projected using the fifth Dirac matrix:

$$\psi_L = \frac{1 - \gamma^5}{2} \psi \quad (1.6)$$

The charged current coupling term is:

$$\mathcal{L}_{CC} = \frac{g}{\sqrt{2}}(J_\mu^+ W^{-,\mu} + J_\mu^- W^{+,\mu}) \quad (1.7)$$

where W^\pm are the gauge fields associated with the W^\pm bosons and J^\pm are the charged weak currents:

$$J_\mu^+ = \sum_{i=1,2,3} \bar{u}_{i,L} \gamma_\mu d_{i,L} + \bar{\nu}_{i,L} \gamma_\mu l_{i,L} \quad (1.8)$$

$$J_\mu^- = \sum_{i=1,2,3} \bar{d}_{i,L} \gamma_\mu u_{i,L} + \bar{l}_{i,L} \gamma_\mu \nu_{i,L} \quad (1.9)$$

where u_i , d_i , l_i , and ν_i are the up-type quark, down-type quark, charged lepton, and neutrino, respectively, in the i th generation.

As seen above, the weak interaction couples only to the left-handed component of the fermions; it is thus not parity-conserving (in fact it is maximally parity-violating). Because the neutrinos couple only to the weak force, only the left-handed components of their spinors are included in the Standard Model; a right-handed neutrino would be *sterile*.

Quarks are included in the currents J^+ , J^- , and J^3 given above and are thus coupled to the weak interaction by the charged and neutral current Lagrangians just as leptons are. However, it has been found that the quark flavor eigenstates that enter these currents are not identical to the quarks' mass eigenstates (which are the eigenstates that enter the strong interaction), but are instead linear combinations of them. The weak eigenstates (indicated by a prime) of the down-type quarks can be related to their mass eigenstates by the Cabibbo-Kobayashi-Maskawa (CKM) matrix:

$$\begin{bmatrix} |d'\rangle \\ |s'\rangle \\ |b'\rangle \end{bmatrix} = \begin{bmatrix} V_{ud} & V_{us} & V_{ub} \\ V_{cd} & V_{cs} & V_{cb} \\ V_{td} & V_{ts} & V_{tb} \end{bmatrix} \begin{bmatrix} |d\rangle \\ |s\rangle \\ |b\rangle \end{bmatrix} \quad (1.10)$$

If this matrix were diagonal, then the weak eigenstates would be identical to the mass eigenstates. In fact, the off-diagonal elements are smaller than the diagonal elements but

are non-zero, meaning that each weak eigenstate consists primarily of the corresponding mass eigenstate but with smaller contributions from the others. The result is that the couplings between the up-type and down-type quarks in eqs. 1.8 and 1.9 do not couple mass eigenstates exclusively within one generation. For example, the u quark couples with the d' weak eigenstate, which means that it couples with the d , s , and b mass eigenstates with strengths given by V_{ud} , V_{us} , and V_{ub} .

The choice to write the down-type weak eigenstates as linear combinations of their mass eigenstates, leaving the up-type weak eigenstates and mass eigenstates identical, is arbitrary. One could, equivalently, define the up-type weak eigenstates in this way and leave the down-type weak eigenstates and mass eigenstates identical. The physical effect is the same: couplings between up-type and down-type mass eigenstates of different generations are introduced.

The CKM matrix must be unitary, and due to this requirement it contains only four free parameters. It can be parametrized in various ways, but frequently three mixing angles and one CP-violating phase are used:

$$U_{\alpha i} = \begin{pmatrix} 1 & 0 & 0 \\ 0 & \cos \theta_{23} & \sin \theta_{23} \\ 0 & -\sin \theta_{23} & \cos \theta_{23} \end{pmatrix} \begin{pmatrix} \cos \theta_{13} & 0 & \sin \theta_{13} e^{-i\delta} \\ 0 & 1 & 0 \\ -\sin \theta_{13} e^{i\delta} & 0 & \cos \theta_{13} \end{pmatrix} \begin{pmatrix} \cos \theta_{12} & \sin \theta_{12} & 0 \\ -\sin \theta_{12} & \cos \theta_{12} & 0 \\ 0 & 0 & 1 \end{pmatrix} \quad (1.11)$$

The angle θ_{12} , which governs the mixing of the three light quarks, is also called the Cabibbo angle, θ_c .

Note that if neutrinos are massless, this CKM mixing occurs in the quark sector but not in the lepton sector. This is done for the simple reason that CKM-like mixing of the leptons cannot be meaningfully defined with massless neutrinos. What it means to say that CKM mixing occurs among the quarks is that the flavor eigenstates (those that play a role in the weak interaction) are linear combinations, or mixtures, of the mass eigenstates. If neutrinos are massless, they have no mass eigenstates to be mixed. However, if, as is now

believed, neutrinos do have non-zero mass, leptonic mixing can occur in exact analogy to the CKM mixing of the quarks described above; this will be discussed in the next section.

1.4 Neutrinos Masses and Mixing

Over the past ten years, a preponderance of evidence has built up showing that neutrinos can change flavor, or “oscillate”. That is, neutrinos that are produced via reactions involving charged leptons of one flavor may, after travelling a long distance, interact to produce charged leptons of another flavor. It should be noted that this does not invalidate the idea of neutrino flavor, because oscillations only occur over suitably long distances. In other words, in the limit where the distance travelled by the neutrinos goes to zero, flavor is conserved.

The mechanism responsible for flavor oscillation is believed to be neutrino mixing. If this is the case, then the flavor eigenstates of the three neutrinos are not the same as the mass eigenstates; rather, the flavor eigenstates are linear combinations of the mass eigenstates. This is exactly analogous to the CKM mixing of the quark mass eigenstates. This implies that neutrinos must have three non-degenerate masses, implying that at least two of the neutrino masses are non-zero. The Standard Model can be extended in a straightforward way to include massive neutrinos and to describe neutrino oscillation.

A given flavor eigenstate can then be written as a linear combination of mass eigenstates:

$$|\nu_\alpha\rangle = \sum_i U_{\alpha i}^* |\nu_i\rangle \quad (1.12)$$

Here α indexes flavor eigenstates and i indexes mass eigenstates. $U_{\alpha i}$ is the Maki-Nakagawa-Sakata (MNS) neutrino mixing matrix, analogous to the CKM matrix for quarks. Like the CKM matrix, the MNS matrix is typically parametrized with three angles and a CP-violating phase. In addition, two Majorana phases, α_1 and α_2 , are needed if neutrinos are Majorana fermions.

$$U_{\alpha i} = \begin{pmatrix} 1 & 0 & 0 \\ 0 & \cos \theta_{23} & \sin \theta_{23} \\ 0 & -\sin \theta_{23} & \cos \theta_{23} \end{pmatrix} \begin{pmatrix} \cos \theta_{13} & 0 & \sin \theta_{13} e^{-i\delta} \\ 0 & 1 & 0 \\ -\sin \theta_{13} e^{i\delta} & 0 & \cos \theta_{13} \end{pmatrix} \begin{pmatrix} \cos \theta_{12} & \sin \theta_{12} & 0 \\ -\sin \theta_{12} & \cos \theta_{12} & 0 \\ 0 & 0 & 1 \end{pmatrix} \times \begin{pmatrix} e^{\frac{i\alpha_1}{2}} & 0 & 0 \\ 0 & e^{\frac{i\alpha_2}{2}} & 0 \\ 0 & 0 & 1 \end{pmatrix} \quad (1.13)$$

The time-evolution of a mass eigenstate i can be written as a plane wave:

$$|\nu_i(x_\mu)\rangle = e^{-i(p_i^\mu x_\mu)} |\nu_i(0)\rangle \quad (1.14)$$

Here x^μ denotes the neutrino's position four-vector and p_i^μ the momentum four-vector of its i th mass eigenstate. Note that in the ultrarelativistic limit, $p_i^\mu x_\mu \approx \frac{m_i^2 L}{2E}$, where $L = |\vec{x}|$ is the distance the neutrino has traveled and E is its energy. Because the mass eigenstates are non-degenerate, the amplitude of each eigenstate will vary at a different rate. Thus, for a neutrino that is in a flavor eigenstate at $t = 0$, the relative amplitudes of its component mass eigenstates will change as it propagates. Specifically, a neutrino in flavor eigenstate α at $t = 0$ can be written as:

$$|\nu_\alpha(x_\mu)\rangle = \sum_i U_{\alpha i}^* e^{-i\frac{m_i^2 L}{2E}} |\nu_i(0)\rangle \quad (1.15)$$

We can then write the probability that a neutrino in flavor state α at $t = 0$ will be observed in flavor state β after having traveled a distance L as:

$$P_{\alpha \rightarrow \beta} = |\langle \nu_\beta | \nu_\alpha(0) \rangle|^2 = \left| \sum_i U_{\alpha i}^* U_{\beta i} e^{-i\frac{m_i^2 L}{2E}} \right|^2 \quad (1.16)$$

The parametrization of the mixing matrix given in equation 1.13 can be substituted above to obtain the oscillation probability in terms of the mixing angles and CP-violating

phase, but the resulting expression is very cumbersome. However, in cases where only two neutrinos mix, all but one of the mixing angles may be neglected. In this case, the oscillation probability is, in terms of the remaining mixing angle θ and the mass difference between the two neutrinos Δm^2 :

$$P_{\alpha \rightarrow \beta} = \sin^2 2\theta \sin^2 \frac{\Delta m^2 L}{4E} \quad (1.17)$$

This two-neutrino mixing expression is a valid approximation in experiments that, due to their particular $\frac{L}{E}$, are only sensitive to one mass splitting. This is the case for atmospheric neutrinos, oscillations of which are dominated by θ_{23} and $\nu_\mu \leftrightarrow \nu_\tau$ mixing. It is also the case for solar neutrinos, for which mixing is dominantly between ν_e and a superposition of ν_μ and ν_τ ; the relevant mixing angle in this case is θ_{12} . Measurements using solar [17] and atmospheric [18] neutrinos have shown that $\theta_{12} = 33.9 \pm 2.4^\circ$ and $\theta_{23} = 45 \pm 7^\circ$. In addition, these measurements have found the mass splittings to be $\Delta m_{12} = 8.0 \pm 0.6 \cdot 10^{-5}$ eV and $\Delta m_{23} \approx \Delta m_{13} = 2.4 \pm 0.6 \cdot 10^{-3}$ eV.

Although these parameters have been reasonably well measured, a large number of open questions relating to neutrino oscillations remain. θ_{13} is known, from reactor experiments, to be less than 3.2° , but no measurement of its value has yet been made. The CP-violating phase δ only enters the oscillation probability expression in combination with θ_{13} and cannot be measured until θ_{13} is known (if θ_{13} is non-zero). Thus the larger question of whether neutrinos violate CP symmetry depends upon the determination of the last mixing angle. The mass hierarchy also presents an unsolved question. We know from measurements of the mass splitting in solar and atmospheric neutrinos that two of the masses are much closer to one another than to the third mass. We do not, however, know whether the outlier mass is above (the so-called “normal hierarchy”) or below (“inverted hierarchy”) the close pair. We also do not know the absolute scale of the neutrino masses, though an upper limit of about 0.63 eV have been obtained from cosmology [19] and a somewhat weaker upper limit of 2.2 eV from tritium beta decay experiments [20, 21].

A further question posed by the non-zero mass of the neutrino is whether the neutrino is a Dirac or a Majorana fermion, that is, whether they obey the Dirac equation (eq. 1.18) or the Majorana equation (eq. 1.19):

$$(i\gamma^\mu \partial_\mu - m)\psi(x) = 0 \tag{1.18}$$

$$i\gamma^\mu \partial_\mu \psi(x) - m\psi_c(x) = 0 \tag{1.19}$$

where γ are the Dirac matrices, ψ is the spinor representing the neutrino, and ψ_c is the charge conjugate of the spinor.

A Majorana fermion has the interesting property that it is its own anti-particle; in terms of the spinor, $\psi = -i\gamma^2\psi$. Thus, if neutrinos are Majorana particles, then anti-neutrinos are simply neutrinos with right-handed helicity. In this case, the emission of a neutrino is identical to the absorption of an anti-neutrino, and *vice versa*. This property implies that neutrinoless double beta decay is allowed if the neutrino is a Majorana particle. Whereas ordinary double beta decay involves the emission of two neutrinos, if the neutrino is its own anti-particle then this can be replaced with the exchange of a (virtual) neutrino; equivalently, one can think of this as the two emitted neutrinos annihilating with each other. Searches for neutrinoless double beta decay are thus the most promising path to determining the nature of the neutrino mass.

Note that we have so far assumed that the three neutrino masses are parameters that must be determined empirically and added to the Standard Model “by hand”. It is, however, possible to posit additional beyond the Standard Model physics that leads to the neutrino masses arising naturally and thus “explains” why they have the values they do. Of particular interest is the so-called “see-saw mechanism” [22, 23], which posits heavy, right-handed (sterile) partners for each of the three light neutrinos. These light and heavy neutrino masses arise from the two eigenvalues of the neutrino mass matrix. In particular, if neutrinos have a Majorana mass on the order of the GUT scale and a Dirac mass on the

order of the electroweak scale, the light neutrino will have a mass on the order of 1 eV. The small size of the neutrino masses would thus arise in a natural way. Note, however, that this mechanism only works if neutrinos have both Dirac and Majorana mass terms. This is one reason for the current interest in determining whether neutrinos are Dirac or Majorana fermions.

1.5 Neutrino Cross-sections

The charged current and neutral current electroweak Lagrangians (eqs. 1.3, 1.7) can be used to exactly calculate the cross-sections for interactions between neutrinos and charged leptons. Cross-sections for neutrino interactions with free quarks can also be calculated exactly, but this is of limited use because free quarks do not occur in nature. In practice, most neutrino interactions with matter are with protons and neutrons, baryons containing three valence quarks. At high interaction energies, these quarks can be treated as free, and the cross-sections calculated for interactions with free quarks are a good approximation. At lower energies, however, strong interactions play a significant role, and due to the non-perturbative nature of QCD, the cross-sections cannot be calculated exactly.

A charged current interaction between a neutrino and a nucleon has the general form $\nu N \rightarrow lX$, where N can be either a proton or neutron, l is a charged lepton, and X represents the hadronic final state. Using the charged current weak Lagrangian (eq. 1.7) and the Feynman rules, we can write the transition amplitude for such a process as:

$$T_{CC}(\nu N \rightarrow lX) = \frac{g^2 \cos \theta_c}{8} [\bar{l} \gamma^\mu (1 - \gamma^5) \nu_\mu] \frac{g_{\mu\nu} - \frac{q_\mu q_\nu}{M_W^2}}{q^2 - M_W^2} \langle X | J^\mu | N \rangle \quad (1.20)$$

where θ_C is the Cabibbo angle, q^μ is the four-momentum of the W , and M_W is the mass of the W . For $q^2 \ll M_W^2$, this simplifies to:

$$T_{CC}(\nu N \rightarrow lX) = \frac{G_F \cos \theta_c}{\sqrt{2}} [\bar{l} \gamma^\mu (1 - \gamma^5) \nu_\mu] \langle X | J^\mu | N \rangle \quad (1.21)$$

where we have also used the Fermi constant $G_F = \frac{\sqrt{2}g^2}{8M_W^2}$ to simplify notation.

The leptonic current term $T_l = [\bar{l}\gamma^\mu(1 - \gamma^5)\nu_\mu]$ involves no strong interactions and can be calculated exactly. The hadronic term $T_H = \langle X|J_H^\mu|N\rangle$ cannot be calculated exactly; however, various models exist for parametrizing this term for different hadronic final states X .

1.5.1 Charged Current π^+ Production

Charged current π^+ production ($CC\pi^+$) refers to any charged current interaction that produces a single positively charged pion. The dominant mode for this interaction is *resonant* pion production, in which the neutrino interacts with a nucleon, exciting that nucleon into a resonant state which subsequently produces a pion in its decay. At low energies, the dominant resonance is the Δ , a spin- $\frac{3}{2}$ state: $\nu N \rightarrow l^- \Delta \rightarrow l^- N \pi^+$.

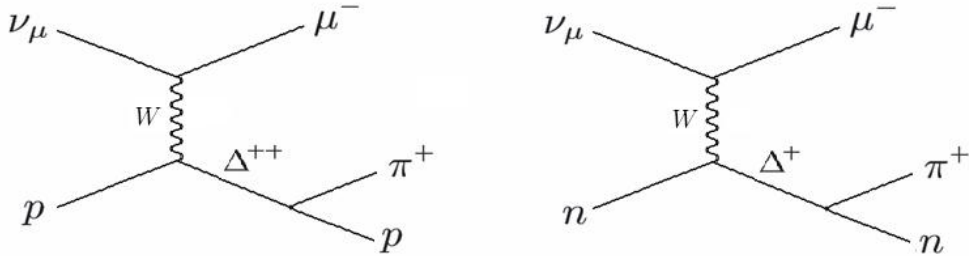


Figure 1.1: Feynman diagrams for the most common $CC\pi^+$ resonant modes on a proton and on a neutron.

The model most frequently used for resonant pion production is the Rein-Sehgal (RS) model. This model forms the basis of the $CC\pi^+$ simulation used by MiniBooNE. A brief overview of the model is given here; details can be found in [24].

The expression given for the charged current transition amplitude in eq. 1.21 contains a leptonic current term and a hadronic current term. The leptonic current represents the polarization vector of the exchanged boson (in this case, the W). It can be written in terms of its left-handed, right-handed, and scalar components. In the rest frame of the hadronic final state (the resonance rest frame, RRF), ignoring the lepton mass, the leptonic current

is:

$$T_l^\mu = -2\sqrt{2}E_\nu \sqrt{\frac{-q^2}{Q^2}} (ue_L^\mu - ve_R^\mu + \sqrt{2uv}e_0^\mu) \quad (1.22)$$

where $Q = |\vec{q}|$ is the momentum of the W in the lab frame and the following definitions are used:

$$u = \frac{E_\nu + E_l + Q}{2E_\nu} \quad (1.23)$$

$$v = \frac{E_\nu + E_l - Q}{2E_\nu} \quad (1.24)$$

$$e_L^\mu = \frac{1}{\sqrt{2}}(0, 1, -i, 0) \quad (1.25)$$

$$e_R^\mu = \frac{1}{\sqrt{2}}(0, -1, -i, 0) \quad (1.26)$$

$$e_0^\mu = \frac{1}{\sqrt{2}}(1, 0, 0, 0) \quad (1.27)$$

The hadronic current J_μ^H can also be transformed into the basis of the unit vectors e_L^μ , e_R^μ , and e_0^μ . At the same time, we will take a factor of the Δ mass out of the hadronic current:

$$F_\mu = \frac{J_\mu^H}{m_\Delta} = (F_t, F_x, F_y, F_z) \quad (1.28)$$

$$F_+ = e_R^\mu F_\mu = -\frac{1}{\sqrt{2}}(F_x + iF_y) \quad (1.29)$$

$$F_- = e_L^\mu F_\mu = \frac{1}{\sqrt{2}}(F_x - iF_y) \quad (1.30)$$

$$F_0 = \sqrt{\frac{-q^2}{Q_{RRF}^2}} e_0^\mu F_\mu = F_t + \frac{E_{q,RRF}}{Q_{RRF}} F_z \quad (1.31)$$

where $E_{q,RRF}$ and Q_{RRF} are the W energy and momentum, respectively, in the resonance rest frame, which are related to the lab-frame quantities by:

$$Q_{RRF} = \frac{m_N}{m_\Delta} Q, \quad q^2 = E_q^2 - Q^2 = E_{q,RRF}^2 - Q_{RRF}^2 \quad (1.32)$$

Using these definitions, the full neutrino matrix element for the excitation can be writ-

ten:

$$T_{CC}(\nu N \rightarrow l\Delta) = -4G_F \cos \theta_c E_\nu \left(\sqrt{\frac{-q^2}{Q^2}} \langle \Delta | uF_- - vF_+ | N \rangle + \frac{m_N}{m_\Delta} \sqrt{2uv} \langle \Delta | F_0 | N \rangle \right) \quad (1.33)$$

To obtain the differential cross-section for this resonance, we include the phase space factors:

$$\frac{\partial \sigma}{\partial q^2 \partial E_q} = \frac{1}{64\pi m_N E_\nu^2} \sum_{spins} |T_{CC}(\nu N \rightarrow l\Delta)|^2 \frac{1}{2\pi} \frac{\Gamma}{(W - M_\Delta)^2 + \frac{\Gamma^2}{4}} \quad (1.34)$$

The term $\frac{1}{2\pi} \frac{\Gamma}{(W - M_\Delta)^2 + \Gamma^2/4}$ is the Breit-Wigner factor, where W is the observed invariant mass of the resonance and Γ is the width of the resonance (for a resonance of negligible width, this could be approximated with $\delta(W - M)$).

Writing the transition amplitude in terms of its helicity components, this is:

$$\frac{\partial \sigma}{\partial q^2 \partial E_q} = \frac{-G_F^2 \cos^2 \theta_c}{8\pi^2} \frac{q^2}{Q^2} \frac{\Gamma}{(W - M_\Delta)^2 + \frac{\Gamma^2}{4}} (u^2 \sigma_- + v^2 \sigma_+ + 2uv \sigma_0) \quad (1.35)$$

where σ_k are the partial cross-sections for absorption of a W of helicity k :

$$\sigma_\pm = \frac{m_\Delta}{m_N} \frac{1}{2} \sum_{j_z} f_{\pm, j_z}^2 \quad (1.36)$$

$$\sigma_0 = -\frac{m_N}{m_\Delta} \frac{Q^2}{q^2} \sum_{j_z} f_{0, j_z}^2 \quad (1.37)$$

$$f_{k, j_z} = \langle N, j_z + k | F_k | \Delta, j_z \rangle \quad (1.38)$$

Equation 1.35 gives the differential cross section for a single resonance (in this case, the Δ). However, a number of other resonances contribute to pion production, and these resonances and their interferences must be taken into account. In the case of $CC\pi^+$, we are interested in any processes that contribute to either the $\mu^- \pi^+ p$ or $\mu^- \pi^+ n$ final states.

We can decompose the hadronic final states using Clebsch-Gordon coefficients:

$$|\pi^+ p\rangle = |1, 1\rangle \otimes \left| \frac{1}{2}, \frac{1}{2} \right\rangle = \left| \frac{3}{2}, \frac{3}{2} \right\rangle \quad (1.39)$$

$$|\pi^+ n\rangle = |1, 1\rangle \otimes \left| \frac{1}{2}, -\frac{1}{2} \right\rangle = \frac{1}{\sqrt{3}} \left| \frac{3}{2}, \frac{1}{2} \right\rangle + \sqrt{\frac{2}{3}} \left| \frac{1}{2}, \frac{1}{2} \right\rangle \quad (1.40)$$

Modes of $CC\pi^+$ production thus include resonances of isospin $\frac{3}{2}$ (Δ resonances) and resonances of isospin $\frac{1}{2}$ (N resonances). Using the Clebsch-Gordon coefficients, the transition amplitude for a given final state can be written in terms of the transition amplitudes for each Δ and each N resonance. Resonances with the same spin and total angular momentum must be allowed to interfere. The squared amplitudes for the $\pi^+ p$ and $\pi^+ n$ final states are thus:

$$\begin{aligned} |T_{CC}(\nu_\mu p \rightarrow \mu^- \pi^+ p)|^2 &= \left| \sum T_{CC}(\Delta_{01}^+) \right|^2 + \sum_{j=1,3} \left| \sum T_{CC}(\Delta_{1j}^+) \right|^2 \\ &+ \sum_{j=3,5} \left| \sum T_{CC}(\Delta_{2j}^+) \right|^2 + \sum_{j=5,7} \left| \sum T_{CC}(\Delta_{3j}^+) \right|^2 \end{aligned} \quad (1.41)$$

$$\begin{aligned} |T_{CC}(\nu_\mu n \rightarrow \mu^- \pi^+ n)|^2 &= \left| \sqrt{\frac{1}{3}} \sum T_{CC}(\Delta_{01}^+) + \sqrt{\frac{2}{3}} \sum T_{CC}(N_{01}^+) \right|^2 \\ &+ \sum_{j=1,3} \left| \sqrt{\frac{1}{3}} \sum T_{CC}(\Delta_{1j}^+) + \sqrt{\frac{2}{3}} \sum T_{CC}(N_{1j}^+) \right|^2 \\ &+ \sum_{j=3,5} \left| \sqrt{\frac{1}{3}} \sum T_{CC}(\Delta_{2j}^+) + \sqrt{\frac{2}{3}} \sum T_{CC}(N_{2j}^+) \right|^2 \\ &+ \sum_{j=5,7} \left| \sqrt{\frac{1}{3}} \sum T_{CC}(\Delta_{3j}^+) + \sqrt{\frac{2}{3}} \sum T_{CC}(N_{3j}^+) \right|^2 \end{aligned} \quad (1.42)$$

where Δ_{lj} and N_{lj} indicate the isospin $\frac{3}{2}$ and isospin $\frac{1}{2}$ resonances, respectively, with orbital angular momentum l and spin $\frac{j}{2}$. In the RS model, all resonances with mass less than 2 GeV are included in the summations.

The amplitude for each resonance can be split into a factor for production of the resonance and a factor for decay of the resonance to a π^+N final state:

$$T_{CC}(N^*) = f(N^*)\eta(N^*) \quad (1.43)$$

where N^* denotes a given resonance (either an N or a Δ), f is the production amplitude, and η is the decay amplitude. The production amplitudes are the same as those given in eq. 1.38. The decay amplitudes consist of a Breit-Wigner factor and a factor of the branching ratio for decay of the resonance to π^+N .

This completes the kinematics of the interaction. What remains is to complete the dynamical part by obtaining the production and decay amplitudes. Rein and Sehgal use the Feynman-Kislinger-Ravndal (FKR) quark model for hadrons to compute these amplitudes. The FKR model treats a hadron as a relativistic harmonic oscillator with the Hamiltonian:

$$\mathcal{H} = 3(p_a^2 + p_b^2 + p_c^2) + \frac{\Omega^2}{36}[(u_a - u_b)^2 + (u_b - u_c)^2 + (u_c - u_a)^2] + C \quad (1.44)$$

where p_x is the 4-momentum of quark x and u_x is its 4-position; Ω is a constant that must be determined empirically. The propagator for baryons is $\frac{1}{\mathcal{H}}$. Using this Hamiltonian, Rein and Sehgal write creation and annihilation operators for the oscillators. This Hamiltonian includes only the strong interactions of the quarks, but electroweak interactions are included by adding vector and axial vector interaction terms:

$$e^\mu j_\mu^V = e^\mu \cdot 3 \sum_a Q_a (\not{p}_a \gamma_\mu e^{iqu_a} + \gamma_\mu e^{iqu_a} \not{p}_a) \quad (1.45)$$

$$e^\mu j_\mu^A = e^\mu \cdot 3 \sum_a Q_a (Z \not{p}_a \gamma_\mu \gamma_5 e^{iqu_a} + Z \gamma_\mu \gamma_5 e^{iqu_a} \not{p}_a) \quad (1.46)$$

where e^μ is the polarization vector, Q_a is a unitary spin matrix, q is the momentum transfer, Z is an empirical renormalization constant for the axial vector current, and \not{p} is the usual Feynman slash notation: $\not{p} = \gamma^\mu p_\mu$.

Using this coupling and the creation operators for excited states of the baryon oscillator, Rein and Sehgal compute the transition amplitudes and cross-sections for production of all nuclear resonances below 2 GeV. The resulting expressions are long and are not reproduced here. The transition amplitudes include separate vector and axial vector form factors, which are assumed to have the form:

$$G^{V,A}(q^2) = \left(1 - \frac{q^2}{4m_N^2}\right)^{\frac{1}{2}-n} \left(\frac{1}{1 - \frac{q^2}{m_{V,A}^2}}\right)^2 \quad (1.47)$$

where n is the number of oscillator quanta in the final resonance and m_V and m_A are constants that must be obtained empirically. The vector mass, m_V , has been measured in electron scattering experiments to be 0.84 MeV [25]; the axial mass, m_A , can only be measured in neutrino interactions. Note that m_V and m_A do not refer to the physical mass of any particles but are merely parameters of the model with units of mass.

The RS model shows significant disagreement with pion production data, particularly at low Q^2 . A variety of modifications to the RS model have been proposed to give a better fit to data. In the original RS calculation, the mass of the muon was ignored. Several extensions of the model to include muon mass have been described [26, 27, 28, 29]. Including the muon mass improves the model's agreement with data at low Q^2 [30].

Newer models replace the vector and axial form factors with more general expressions derived from the Rarita-Schwinger formalism [31, 32, 33], which include several form factors $C_i^{V,A}$. Fits to resonant production data from previous experiments have been performed [30, 34], but in general new data is needed to test these models.

In the resonant processes described above, the neutrino effectively interacts with a single nucleon. Coherent interactions of a neutrino with a whole nucleus can also result in pion production. In the charged current case, this results in another $CC\pi^+$ channel, $\nu A \rightarrow l^- \pi^+ A$, where A represents the target nucleus. A variety of models exist for coherent pion production [35, 36, 37, 38], but this interaction channel remains poorly understood and the models' predictions for the coherent pion production cross-sections vary by an order of

magnitude. Recent results from K2K and SciBooNE [39, 40] show no evidence for charged current coherent pion production; however, results from MiniBooNE and SciBooNE [41, 42, 43] do favor a coherent contribution to neutral current pion production, MiniBooNE obtaining a $19.5 \pm 3.6\%$ coherent fraction and SciBooNE $17.9 \pm 4.1\%$.

In addition to creating the possibility of coherent pion production, the use of a nuclear medium as the target in a neutrino scattering experiment introduces some complications for resonant interactions. The RS model assumes interactions of a neutrino with a free nucleon; the cross-section is modified by the binding of the target nucleon within a nucleus. Further, interior nucleons are screened by the nucleons on the surface, again modifying the cross-section. These effects are typically treated using the relativistic Fermi gas model. This model characterizes a nucleus with two parameters, the binding energy E_B and the Fermi momentum p_F . The nucleons are treated as a degenerate gas, with all energy levels up to p_F filled. The struck nucleon must therefore have a momentum greater than p_F in the final state; this is known as Pauli blocking, and has the effect of reducing the cross section at low Q^2 , where lower momenta for the outgoing nucleon are favored. The kinematics of the interaction are also affected by the nucleon's binding energy. Again, this decreases the cross section at low Q^2 , because it restricts the available phase space of the final state by requiring some of the transferred energy to be used to free the nucleon.

If a resonant interaction does occur, the products must first propagate through the nucleus before they can be detected. Several more nuclear effects come into play at this stage. First, the excited nucleon may de-excite through re-interaction, $\Delta N \rightarrow NN$, rather than through decay. If the struck nucleon does decay and produce a pion, that pion must then propagate through the nucleus and may either be absorbed or exchange charge with a nucleon. All of these effects decrease the number of observable $CC\pi^+$ events.

1.5.2 Charged Current Quasi-Elastic Scattering

Charged current quasi-elastic scattering ($CCQE$) refers to an interaction wherein a neutrino exchanges charge with a nucleon. The only such process possible for a neutrino is

$\nu n \rightarrow l^- p$ (the corresponding anti-neutrino process is $\bar{\nu} p \rightarrow l^+ n$). This interaction is called “quasi-elastic” because both the initial and final states contain one lepton and one nucleon.

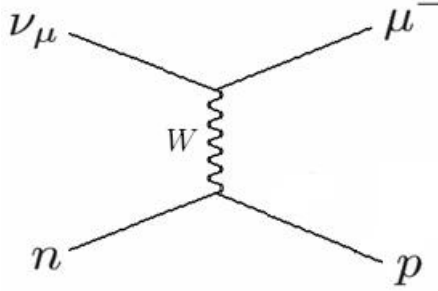


Figure 1.2: Feynman diagram for charged current quasi-elastic scattering.

$CCQE$ scattering is the dominant interaction channel for neutrino energies on the order of 1 GeV (about 40% of neutrino events in MiniBooNE are expected to be $CCQE$). As with the $CC\pi^+$ cross section, the amplitude for $CCQE$ scattering can be divided into leptonic and hadronic terms. A parametrization of this amplitude is given by the Llewellyn-Smith formalism [44]; it is of the form:

$$\frac{d\sigma}{dQ^2} = \frac{M^2 G_F \cos^2 \theta_C}{8\pi E_\nu^2} \left(A(Q^2) \pm B(Q^2) \frac{s-u}{M^2} + C(Q^2) \frac{(s-u)^2}{M^4} \right) \quad (1.48)$$

where E_ν is the energy of the incident neutrino, M is the mass of the nucleon, and s and u are the Mandelstam variables. The expressions for the coefficients A , B , and C in terms of form factors are long, but assuming no T-violation in the neutrino-nucleon interaction, no parity violation in the electromagnetic and strong interactions, and a leptonic mass much smaller than the nucleon mass, they can be simplified to:

$$\begin{aligned} A(Q^2) &= \frac{Q^2}{M^2} \left(\left(1 - \frac{Q^2}{4M^2}\right) F_A^2 - \left(1 - \frac{Q^2}{4M^2}\right) F_1^2 + \frac{Q^2}{4M^2} \left(1 - \frac{Q^2}{4M^2}\right) F_2^2 + 4 \frac{Q^2}{4M^2} F_1 F_2 \right) \\ B(Q^2) &= \frac{Q^2}{M^2} F_A (F_1 - F_2) \\ C(Q^2) &= \frac{1}{4} (F_A^2 + F_1^2 + \frac{Q^2}{4M^2} F_2^2) \end{aligned} \quad (1.49)$$

The amplitude thus depends on three form factors, F_1 and F_2 (the vector form factors),

and F_A (the axial form factor). Using conservation of vector current (CVC), the two vector form factors can be related to the Dirac and Pauli electromagnetic form factors and parametrized in terms of the vector mass m_V , which has been measured in electron scattering experiments. F_A is parametrized in terms of the axial mass m_A , which must be measured in neutrino experiments.

The cross-section given in 1.48 treats the target nucleon as free. An extension of this model to include bound nucleons is given by Llewellyn-Smith and Moniz in [45]. This model treats the nucleus as a relativistic Fermi gas, as discussed above in connection with nuclear effects in $CC\pi^+$ interactions.

1.5.3 Neutrino Cross-section Measurements

Although calculations of neutrino cross-sections had been made since 1934 [2], it was not until the 1970s that measurements of these cross-sections became possible. The first generation of neutrino cross-section measurements consisted of bubble chamber experiments performed during the 1970s and 1980s at ANL, BNL, FNAL, and CERN. These experiments generally measured cross-sections in the energy range $0.5 \text{ GeV} < E_\nu < 10 \text{ GeV}$, on low-mass targets such as hydrogen or deuterium. Although they provided important data, the precision of these measurements was severely limited by their low statistics and poor knowledge of the neutrino fluxes.

The next generation of cross-section measurements was made with higher energy neutrino sources and using a variety of detector technologies. Experiments such as NuTeV, CCFR, CHARM, and CDHS looked at neutrinos in the $20 \text{ GeV} < E_\nu < 200 \text{ GeV}$ energy range. These experiments had much higher statistics than their predecessors, and the neutrino cross-sections at high energies were measured with high precision.

With the discovery of neutrino oscillations in the late 1990s, interest in low energy neutrinos increased again. In order to perform sensitive oscillation searches, it is necessary to know the neutrino-nucleon cross-sections to high precision. However, until quite recently, for neutrinos with energy on the order of 1 GeV, the only cross-section data available was

| Experiment | Detector | Target | Date |
|----------------|----------------|--------------|------|
| ANL [46] | Bubble chamber | D_2 | 1977 |
| BEBC [47] | Bubble chamber | D_2 | 1990 |
| BNL [48] | Bubble chamber | D_2 | 1981 |
| GGM [49] | Bubble chamber | Propane-fron | 1979 |
| FNAL [50] | Bubble chamber | D_2 | 1983 |
| Serpukhov [51] | Spark chamber | Al | 1985 |
| SKAT [52] | Bubble chamber | CF_3Br | 1992 |

Table 1.1: $CCQE$ cross-section measurements.

| Experiment | Detector | Target | Date |
|------------------|----------------------|----------|------------------|
| ANL [53, 54, 55] | Bubble chamber | D_2 | 1973, 1979, 1982 |
| BEBC [47, 56] | Bubble chamber | D_2 | 1986, 1990 |
| BNL [57] | Bubble chamber | D_2 | 1986 |
| FNAL [58] | Bubble chamber | D_2 | 1978 |
| K2K [59] | Plastic scintillator | C_8H_8 | 2008 |
| SKAT [60] | Bubble chamber | CF_3Br | 1989 |

Table 1.2: $CC\pi^+$ cross-section measurements.

from bubble chamber experiments of the 1970s and 1980s. Besides having large error bars, these data also come almost exclusively from targets with low nuclear mass. Modern oscillation experiments, on the other hand, tend to use heavier nuclei in order to obtain higher event rates; but this results in significant nuclear effects, concerning which the older experiments have nothing to tell us. Thus, there is a pressing need for high-statistics, high-precision cross-section measurements at low energies and on heavy nuclear targets.

1.6 The $CC\pi^+$ to $CCQE$ Ratio

At neutrino energies on the order of 1 GeV, a region of great interest for oscillation experiments, $CCQE$ and $CC\pi^+$ are the two largest event classes. In MiniBooNE, for example, these two channels account for roughly 64% of neutrino events. Due to their abundance and relatively clean experimental signature, $CCQE$ events are typically used as the signal channel in neutrino oscillation searches. Accelerator-based appearance searches such as MiniBooNE’s oscillation analysis look for an excess of ν_e $CCQE$ events over background

from a ν_μ source; likewise disappearance searches look for a deficit of ν_μ $CCQE$ events from a ν_μ source. The largest background to ν_μ $CCQE$ events at these energies typically comes from $CC\pi^+$ events in which the pion is not seen. Because of the abundance of $CC\pi^+$ events, this background tends to be very large; in MiniBooNE, for example, the $CC\pi^+$ background makes up about 20% of the ν_μ $CCQE$ sample. To extract this background while retaining sensitivity to small oscillation signals, ν_μ disappearance experiments require knowledge of the ratio of $CC\pi^+$ to $CCQE$ cross sections as a function of energy to a precision of better than 10%. No prior experiment, however, has measured this ratio to better than about 20% precision, nor with an energy resolution finer than about 0.2 GeV. Further, most previous experiments used hydrogen or deuterium targets, whereas modern oscillation experiments typically use heavier nuclei, subjecting the interactions to nuclear effects not encountered with a lower mass target.

In addition to disappearance analyses using $CCQE$ events, auxilliary searches using $CC\pi^+$ as the signal channel as well as CC inclusive searches are also possible. In these cases, knowledge of the $CC\pi^+$ cross-section is necessary not for the removal of background but for the prediction of signal rates. Although measuring rates in a near detector would minimize the dependence of the signal prediction on external cross-section data, it remains desirable to understand all oscillation signal channels as fully as possible.

Besides its direct application to neutrino oscillation searches, measurement of the $CC\pi^+$ cross-section is important for our understanding of neutrino-induced pion production. As noted above, a variety of proposals for corrections to the Rein-Sehgal model of pion production have been made; however, the ability of theorists to evaluate these models has been limited by the paucity of cross-section data at low energies.

The $CCQE$ and $CC\pi^+$ differential cross-sections can be measured directly and their ratio calculated from the individual cross-sections. However, the sizeable uncertainties on the neutrino flux in MiniBooNE limit the precision of such a procedure. In order to eliminate the flux uncertainties, we can instead measure the ratio directly, in which case the flux uncertainties largely cancel between the two samples. This type of ratio measurement

provides the cleanest way of extracting the $CC\pi^+$ background from the $CCQE$ signal in ν_μ disappearance searches. It also provides data that theorists, armed with models for $CCQE$ scattering, can use to evaluate pion production models.

In addition to the ratio reported in this thesis, several other current and future experiments have provided or will provide high-precision measurements of the $CCQE$ and $CC\pi^+$ cross-sections at low energy. Since the publication of this analysis, MiniBooNE has also completed absolute $CCQE$ [61] and $CC\pi^+$ [62] cross-section measurements. Other experiments, including both dedicated cross-section experiments such as MINER ν A and oscillation experiments such as MINOS, NO ν A, and T2K, will also be able to provide measurements of these cross-sections in the near future.

In addition to these, several experiments employing liquid argon Time Projection Chambers (LArTPCs), a relatively new detector technology, are underway or have been proposed. In an LArTPC, charged particles passing through a volume of liquid argon ionize electrons as they pass; an electric field is applied so that these electrons drift to a read-out plane on one side of the TPC. This offers the modern equivalent of a bubble chamber display, reconstructing high resolution images of the particles' tracks. LArTPCs offer a number of advantages over traditional neutrino detectors and promise to play an important role in neutrino physics - both in oscillation studies and in cross-section measurements. The ArgoNeuT experiment has collected data in the NuMI beam at Fermilab, and despite its comparatively low statistics may be able to make $CC\pi^+$ and $CCQE$ cross-section measurements. MicroBooNE, which is to run in the MiniBooNE enclosure in the Booster Neutrino Beam, will experience the same neutrino flux as MiniBooNE but will have an advantage in systematics, and should be able to improve upon the ratio measurement presented here as well as other MiniBooNE cross-section analyses.

Chapter 2

The MiniBooNE Experiment

The MiniBooNE experiment was designed to search for ν_μ to ν_e oscillations with a Δm^2 between 0.2 eV^2 and 10 eV^2 , evidence for which had been observed in anti-neutrinos by the LSND experiment. The anti-neutrino flux in the LSND detector was peaked at a neutrino energy of about 40 MeV, and the center of the detector was about 30 m from the neutrino source. The MiniBooNE detector is situated in the Booster Neutrino Beam (BNB) at Fermi National Accelerator Laboratory, with a neutrino energy spectrum peaked at around 800 MeV; the detector is located 450 m from the neutrino source, giving an L/E similar to that in the LSND experiment. MiniBooNE thus gives access to the same neutrino oscillation parameter space as LSND. Results of the oscillation search in neutrino [63] and anti-neutrino [64] modes showed no evidence for two-neutrino oscillation.

In addition to the primary oscillation search, the MiniBooNE experiment is ideal for performing a number of neutrino cross section measurements. The Booster Neutrino Beam provides a high-intensity neutrino source, offering MiniBooNE an advantage of about an order of magnitude in statistics over any previous experiment in the case of $CC\pi^+$ and $CCQE$ interactions. Moreover, the neutrino flux is peaked at about 800 MeV, an energy region of great interest to future oscillation searches but one that few previous experiments have explored. This makes MiniBooNE eminently suitable for measuring the $CC\pi^+$ to $CCQE$ cross section ratio discussed in section 1.6.

2.1 The Booster Neutrino Beam

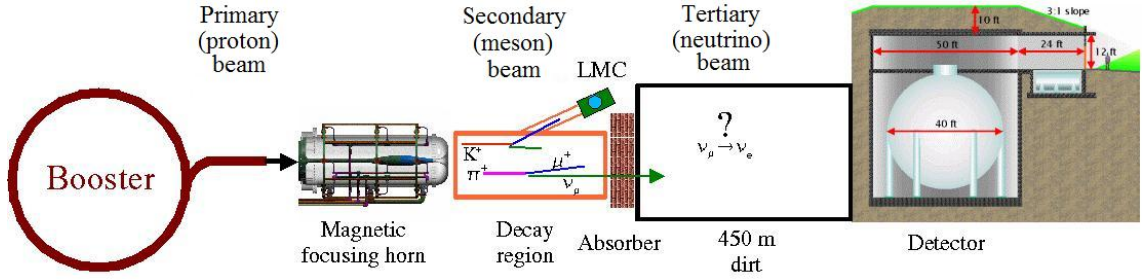


Figure 2.1: The MiniBooNE detector in the Booster Neutrino Beam.

The Booster Neutrino Beam comprises three sequential stages: the primary (proton) beam, the secondary (meson) beam, and the tertiary (neutrino) beam. A cartoon schematic of the beamline is shown in figure 2.1, on which these three sections can be seen.

The primary (proton) beam is produced by a chain of three of Fermilab’s five accelerators. The process begins with hydrogen gas being converted to H^- ions, which are accelerated to 750 keV. The ions are passed to a linear accelerator, which brings them up to 400 MeV. The electrons are then stripped away by carbon foil, and the protons are passed to the Booster synchrotron, which accelerates them to 8 GeV and delivers them to the Booster Neutrino Beamline. The protons are delivered in pulses lasting $1.6 \mu\text{s}$, with an average of four to five pulses per second. Each pulse consists of a series of 81 bunches 2 ns in length and separated by 19 ns. Each pulse typically delivers a total of about $4 \cdot 10^{12}$ protons. The MiniBooNE data acquisition system (DAQ) is synchronized with the timing signals of the Fermilab accelerator network, so that data is recorded beginning $4.5 \mu\text{s}$ before, and ending $19.2 \mu\text{s}$ after, each beam spill. As they pass down the beamline, the protons go through several beam position monitors, which are routinely checked by the person on shift in the MiniBooNE control room to ensure that the beam is on target. The root mean square width of the beam just upstream of the target is 0.75 mm vertically and 1.51 mm horizontally. The beam also passes through two toroids that measure the number of protons on target (POT), located 5 and 50 m upstream of the target. The POT

measurement is accurate to about 1% [65]. The data used in this analysis was collected from August 2002 to December 2005 and corresponds to $5.579 \pm 0.01 \cdot 10^{20}$ POT delivered in about $1.4 \cdot 10^8$ beam spills.

The protons hit a beryllium target at the end of the primary beam. The target is composed of seven cylindrical pieces or “slugs” of beryllium, each 10.16 cm long and 0.9525 cm in diameter. The slugs are suspended within a beryllium sleeve 0.9 cm thick and with an inner radius of 1.37 cm; each slug is supported by three beryllium fins that connect to the sleeve. Heat deposited in the target by the proton beam is dissipated by a stream of forced air.

The interaction of the incident protons with the beryllium target produces the secondary (meson) beam. The products of the p-Be interactions are protons, neutrons, π^\pm , K^\pm , and K^0 . π^\pm are produced with a multiplicity of about 1.8 per reaction, protons 1.5, neutrons 1.3, K^\pm 0.07, and K^0 0.02. These products pass through a pulsed toroidal electromagnet, the MiniBooNE “horn”, 185.4 cm long with a radius of 30 cm. A current of 174 ± 1 kA flows through the horn, producing a magnetic field of about 1 T; the azimuthal symmetry of the horn allows the magnetic field to be well-modelled by Ampere’s Law. When running in neutrino mode, the horn focuses the positively charged products of the p-Be interactions into the beamline while defocusing the negatively charged products; for anti-neutrino running, the direction of current flow in the horn is reversed and the negatively charged products are focused. The horn increases the neutrino flux in the MiniBooNE detector by about a factor of six over what it would be with no focusing. The horn pulses at roughly 5 Hz and is timed so that the current peaks during each beam spill.

The beam passes through a 214 cm long concrete collimator before entering the decay region. The collimator absorbs particles scattered at a large angle, which would not contribute to the neutrino flux, in order to reduce radiation farther down the beamline. The secondary hadrons then enter the decay pipe, an air-filled cylinder 45 m long and three feet in radius. The tertiary (neutrino) beam is created in this region by the decay of secondary mesons. In addition, a small number of muons created by the decay of secondary

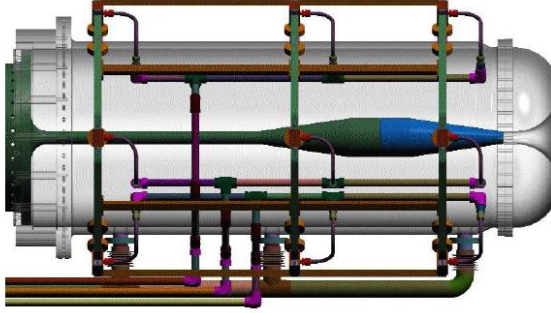


Figure 2.2: The BNB magnetic focusing horn. The outer (grey) conductor is shown semi-transparent to reveal the inner (green and blue) conductor and water cooling apparatus.

mesons subsequently decay to produce neutrinos. The branching ratios for these decays are summarized in table 2.1.

| Particle | Lifetime (ns) | Decay mode | Branching ratio (%) |
|----------|---------------|---------------------------------|---------------------|
| π^+ | 26.03 | $\mu^+ + \nu_\mu$ | 99.9877 |
| | | $e^+ + \nu_e$ | 0.0123 |
| K^+ | 12.385 | $\mu^+ + \nu_\mu$ | 63.44 |
| | | $\pi^0 + e^+ + \nu_e$ | 4.98 |
| | | $\pi^0 + \mu^+ + \nu_\mu$ | 3.32 |
| K_L^0 | 51.6 | $\pi^- + e^+ + \nu_e$ | 20.333 |
| | | $\pi^+ + e^- + \bar{\nu}_e$ | 20.197 |
| | | $\pi^- + \mu^+ + \nu_\mu$ | 13.551 |
| | | $\pi^+ + \mu^- + \bar{\nu}_\mu$ | 13.469 |
| μ^+ | 2197.03 | $e^+ + \nu_e + \bar{\nu}_\mu$ | 100 |

Table 2.1: The branching ratios for neutrino-producing decay modes.

A beam stop consisting of 10 feet of steel and 3 feet of concrete is located at the end of the decay pipe. The beam stop absorbs all non-neutrino products from the decay of the secondary meson beam, as well as any undecayed products of the initial p-Be interaction. The remaining neutrinos then pass through 450 m of earth before entering the detector enclosure. The center of the detector itself is located 541 m downstream of the center of the beryllium target and 1.9 m above the center of the neutrino beam.

In neutrino mode, the beam is composed of 93.6% ν_μ with a 5.9% (0.5%) $\bar{\nu}_\mu$ (ν_e) contamination [66]. The average neutrino energy is roughly 800 MeV. The neutrino flux is not directly measured, but the energy spectrum is obtained from a detailed simulation

of the Booster Neutrino Beam. A discussion of this simulation, including more detailed information on the composition of the neutrino beam, can be found in section 3.1.

2.2 The MiniBooNE Detector

A brief overview of the MiniBooNE detector is given in this section. For a detailed treatment, see [67].

The MiniBooNE detector is a spherical carbon steel tank 12.2 m in diameter filled with 818 tons of mineral oil. The tank is located below ground level in a cylindrical vault 13.7 m in diameter with walls roughly half a meter thick. A room above the detector houses electronics and utilities. The vault is covered by dirt with a minimal depth of 3 m to provide partial shielding against cosmic rays.

Within the outer tank is a second spherical shell 11.5 m in diameter. This shell divides the tank into two optically isolated regions. The outer volume is a “veto region” designed to identify and reject cosmic rays and neutrino events that are not fully contained within the main detector volume. The inner volume is the “signal region”. Though the inner and outer regions are optically isolated, the oil is free to circulate between them. All surfaces in the signal region are painted black to reduce light re-scattering for clean event reconstruction; all surfaces in the veto region are painted white to increase light re-scattering and increase veto sensitivity.

2.2.1 PMTs and Mineral Oil

The inner side of the spherical shell that divides the inner and outer tank regions is lined with 1280 photomultiplier tubes (PMTs). These PMTs are distributed roughly uniformly across the shell and face inward, toward the center of the detector; this results in photocathode coverage of 11.3% of the inner sphere. An additional 240 PMTs are located in the veto region, mounted on the outer tank wall. The veto PMTs are arranged in pairs; each pair is situated back to back, with the PMTs oriented perpendicular to a line from

the center of the tank.

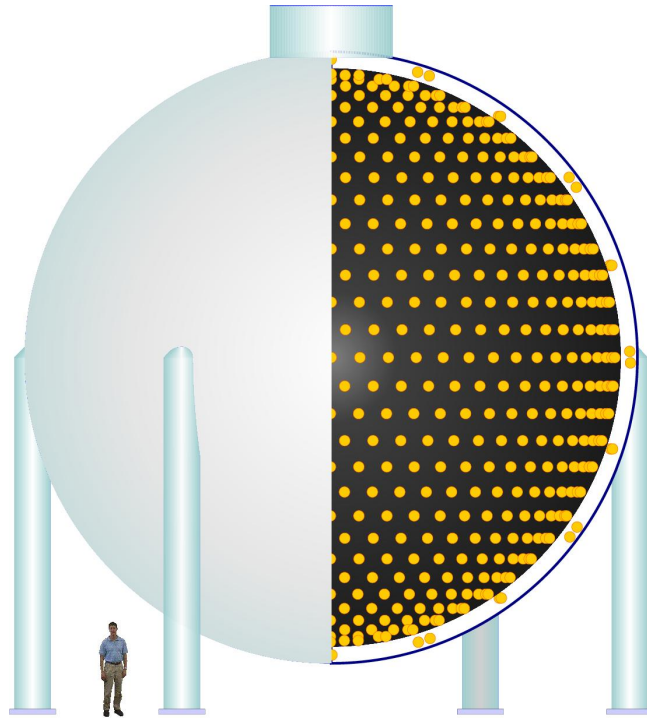


Figure 2.3: The MiniBooNE detector.

Of the 1280 PMTs in the signal region, 958 are Hamamatsu R1408, taken from the LSND experiment. The remaining 322 PMTs are Hamamatsu R5912 bought for MiniBooNE. Because the R5912 PMTs have better time and charge resolution than the R1408, all 958 of the new PMTs were used in the signal region. Figure 2.4 shows the distribution of the new and old PMTs in the signal region. The 240 PMTs used in the veto region were selected from among the LSND PMTs for having the lowest dark rates. Each PMT has an 8" diameter. The R5912 PMTs have a time resolution of about 1.1 ns and a single photo-electron (1-PE) charge resolution of 50%; the R1408 PMTs have a time resolution of about 1.7 ns and a 1-PE charge resolution of 140%. The PMTs are operated at approximately 2000 V, resulting in a gain of $1.6 \cdot 10^7$. The efficiency of the PMTs varies as a function of wavelength, peaking at about 390 nm. Each PMT was tested individually to measure its time and charge resolution, angular acceptance, dark rate, and operating voltage; precise knowledge of these is necessary for event simulation and reconstruction.

After being tested, the R1408 PMTs were cleaned to remove oil residue from LSND and were coated with a black encapsulant from the base to the bottom of the globe to prevent contamination of the oil by components of the base. Details of the PMTs' functionality can be found in [68]. Over the course of commissioning and running, 37 PMTs have failed.

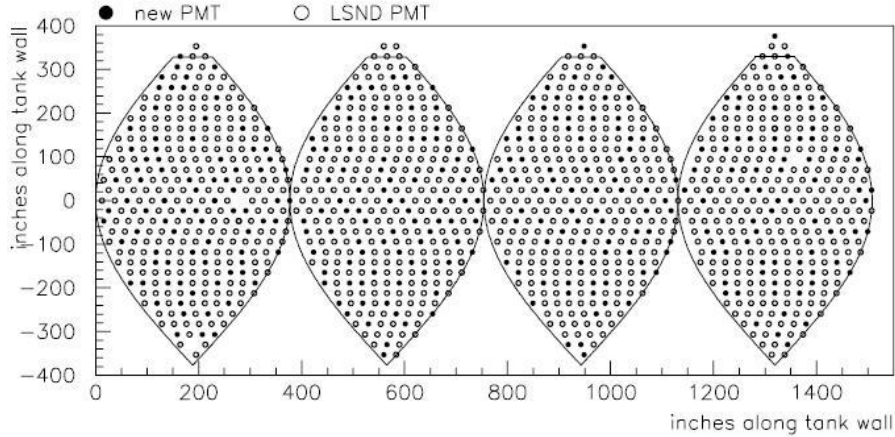


Figure 2.4: Layout of PMTs in the signal region. Clear circles indicate R1408 PMTs and black circles indicate R5912.

The MiniBooNE tank is filled with $9.5 \cdot 10^5$ liters of undoped Exxon/Mobile Marcol 7 light mineral oil. The oil provides both the nuclear target for the incoming neutrinos and a medium in which the charged products of an interaction can produce light; consequently, both its properties as a target and its optical properties needed to be considered in making the choice of mineral oil over another medium, for example, water. The density of mineral oil, 0.845 g/cm^3 , is somewhat lower than that of water, providing fewer nuclear targets and slightly lower event rates; a denser oil would have too viscous to allow recirculation. However, the optical properties of mineral oil are superior to those of water for the purposes of MiniBooNE. Its index of refraction, roughly 1.468 for visible light, is higher than that of water (1.33). This results in both a higher ratio of Čerenkov light to scintillation and a lower Čerenkov threshold. The higher ratio of Čerenkov light allows superior event reconstruction than would be possible with water, and the lower Čerenkov threshold gives MiniBooNE access to lower neutrino energies than would be possible with water. The oil has an extinction length of about 25 m or longer for 460 nm light, and no more than 25%

of photons originating in the center of the tank are lost before they reach the position of the PMTs. All materials that were to be in contact with the oil were tested for possible contaminants by being immersed in the oil for a long period of time (a week or more), at room temperature and at 66°C, after which the extinction length of the oil was measured and compared with a control sample.

2.2.2 Electronics and Data Acquisition

The information recorded during an event consists of charge and timing values in each of the PMTs. The MiniBooNE electronics takes the signals generated by the PMTs, digitizes the charge and timing information, stores the data temporarily, and reads out the data if a trigger is received. The data acquisition electronics, which are re-used from the LSND experiment, are housed in a total of fourteen VME crates: ten crates for the signal region PMTs, two for the veto region PMTs, one for the trigger, and one for calibration time inputs and beam monitoring. The PMTs are organized in groups of 24 handled by each preamp/HV board. The PMTs were sorted into these groups by their measured dependence of gain on voltage; the voltage supplied to each group is tuned to the PMTs' gain so that a uniform gain is achieved across the entire ensemble of PMTs. The MiniBooNE PMT electronics were re-used (after being tested and refurbished) from LSND.

The raw signal, V_{PMT} , generated on a PMT is convolved in the electronics with a decaying exponential with a time constant of about 700 ns to produce the integrated signal V_q . The value of V_q is read out and digitized at a frequency of 10 MHz to obtain the digital charge information. If V_{pmt} crosses a threshold of 2 mV, corresponding roughly to 0.1 photo-electrons, an asynchronous discriminator fires, triggering a voltage ramp, V_t , and signalling the synchronous discriminator to fire on the next tick of the 10 MHz clock. V_t is read out and digitized on this clock-tick and the subsequent one, and then returns quickly to baseline. These two successive measurements of V_t provide the voltage time slope, which is then used to extrapolate to baseline and determine the initial hit time at which V_{pmt} crossed the threshold. The charge and time information is processed by eight-

channel cards, with sixteen cards per crate. Digitization is performed by 8-bit flash ADCs, synchronously with the 10 MHz clock.

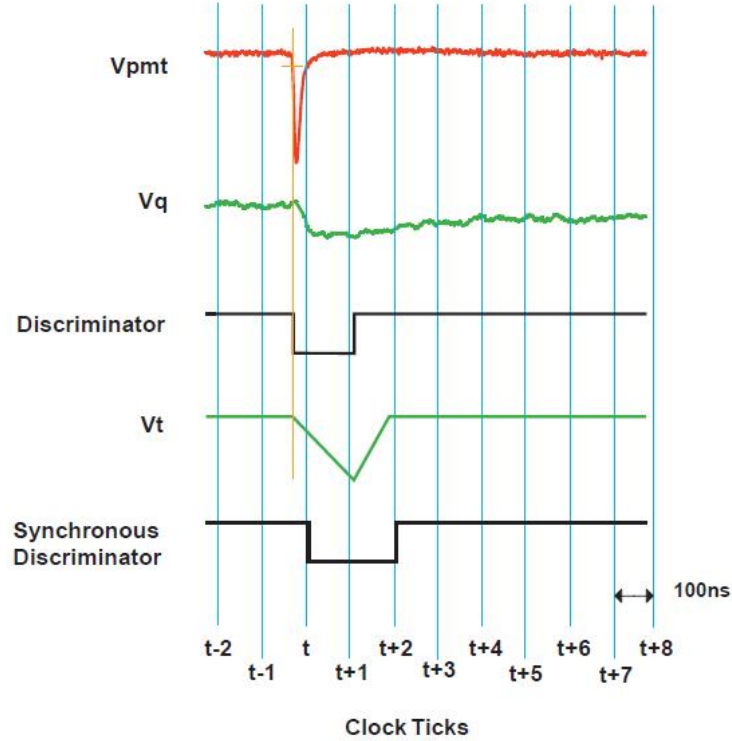


Figure 2.5: Illustration of signals in the PMT electronics.

Data for an event is read out if one of the physics triggers is set to “true”; $19.2 \mu\text{s}$ of data are stored for each event. The states of the physics triggers depend on the states of seven hit “comparators”, which in turn depend on PMT hit information, and three external triggers, which depend on information from outside MiniBooNE. The comparators and external triggers are summarized in table 2.2.

The physics triggers used are:

Beam: This is the main physics trigger for the experiment; it depends solely on the first external trigger, E1, and requires only the “beam to MiniBooNE” signal from ACNET. It is given priority over any other trigger. The primary MiniBooNE neutrino data, including all data used in this analysis, was collected from this trigger.

NuMI: This is triggered when beam is sent to the NuMI beamline, the other neutrino

| Name | Condition | Purpose |
|------|----------------------|-------------------------------------|
| E1 | External signal | Beam trigger |
| E2 | External signal | NuMI, strobe, and debuncher trigger |
| E3 | External signal | Calibration trigger |
| C1 | Tank Hits ≥ 10 | Activity monitor |
| C2 | Tank Hits ≥ 24 | Michel electron |
| C3 | Tank Hits ≥ 200 | High-energy neutrino |
| C4 | Tank Hits ≥ 100 | Neutrino candidate |
| C5 | Tank Hits ≥ 60 | Supernova ν candidate |
| C6 | Veto Hits ≥ 6 | Cosmic veto |
| C7 | Veto Hits ≥ 4 | Cosmic activity |

Table 2.2: The external triggers and internal comparators upon which the MiniBooNE physics triggers depend.

beam at Fermilab. Although off-axis from this beam, the MiniBooNE detector does see a small flux of neutrinos from NuMI. The NuMI beam is timed so as not to be on at the same time as the BNB. The NuMI trigger is given priority over any other trigger.

Strobe: This trigger fires at a rate of 2.01 Hz when the beam trigger is off, collecting data on detector activity when there is no beam.

Laser: This depends solely on the external trigger E3 and is triggered when light is transmitted to the dispersion flasks in the detector for calibration (see section 2.2.3).

Cube: This is triggered by activity in a calibration cube (see section 2.2.3) and is used for cosmic ray calibration.

Tracker: This is triggered by a coincidence in the muon tracker hodoscope (see section 2.2.3) and is used for cosmic ray calibration.

Supernova: This requires C5 and \neg C6; it is used to collect candidates for supernova neutrino events (where \neg is the logical “not” operator).

Michel: This is designed to trigger on stopped muons decaying within the detector; it requires C4 and C6 (to tag the muon) followed 3 to 15 μ s later by C3 and \neg C6 (to tag the electron).

Big ν : This requires C3 and \neg C6 to tag neutrino candidates outside the beam window.

Veto: This requires only C6.

Tank: This requires only C5.

2.2.3 Calibration

MiniBooNE uses a laser calibration system to measure and monitor the performance of the individual PMTs as well as to perform *in situ* measurements of the oil attenuation length. This system uses a pulsed diode laser which transmits pulses of light via optical fiber to four dispersion flasks in the detector. The laser pulses are about 100 ps in length and the light is peaked at a wavelength of 397 nm. The flasks, each a 10 cm diameter sphere, illuminate all the PMTs in the detector with roughly equal intensity. Laser pulses are also delivered to a bare optical fiber that illuminates a $\sim 10^\circ$ cone of PMTs at the bottom of the detector; this is used to study light scattering in the detector. The laser operates at a rate of 3.33 Hz; it is asynchronous with the beam from the accelerator, but a beam extraction timing pulse vetoes the laser so that it does not fire during a beam event. Timing and charge calibration constants for each PMT were obtained from the laser data. These constants allow the conversion of raw PMT hit times to calibrated hit times and of raw charge information into photo-electron units.

Nature provides another calibration source in the form of cosmic muons. To take advantage of cosmic muon events in the detector, a hodoscope scintillator is positioned above the detector and seven scintillator cubes within the detector's signal region. The hodoscope consists of two layers of plastic scintillator separated by one meter and tracks incoming muons with an angular resolution of $\sim 1.9^\circ$. The scintillator tubes, placed at various depths within the detector, are 5 cm on each side, except for the deepest cube, which is 7.6 cm on each side, in order to increase its signal rate. The flux of cosmic ray muons is large enough (about 1 muon per cm^2 per minute) that a significant number will stop and decay within one of the scintillator cubes. Muons decay via only one channel: $\mu^- \rightarrow e^- + \bar{\nu}_e + \nu_\mu$. The electron created in the decay is known as a *Michel electron*. In events where a cosmic muon decays in one of the scintillator cubes, the muon's trajectory and momentum and the origin of the Michel electron can be determined from the hodoscope

| T_μ (MeV) | Angular Resolution | Energy Resolution |
|---------------|--------------------|-------------------|
| 95 ± 4 | 5.4° | 12% |
| 155 ± 5 | 3.2° | 7% |
| 229 ± 7 | 2.2° | 7.5% |
| 407 ± 9 | 1.4° | 4.6% |
| 584 ± 9 | 1.1° | 4.2% |
| 771 ± 9 | 1.0° | 3.4% |

Table 2.3: Muon angle and energy resolution. The six values of T_μ for which the resolutions were measured correspond to the six scintillator cubes; each cube has access to a muon energy determined by its depth.

and scintillator cubes alone, without reference to the PMTs; this provides a way of tuning energies and particle positions in event reconstruction. Once this tuning is done, the detector's resolution in muon energy and muon angle can be measured by comparing the values obtained from the calibration system with those obtained from event reconstruction. These resolutions are shown in table 2.3 and figure 2.6.

This muon calibration can only be performed for muons that pass through the hodoscope and stop in a scintillator cube, and therefore only for muons with a roughly vertical trajectory. Our muon energy reconstruction (discussed in chapter 4), however, is not sensitive to the absolute orientation of the muon track, so data for nearly vertical muons is sufficient for calibration. Any bias resulting from calibration to muons with vertical orientation only will contribute to energy smearing, which is corrected through our energy unfolding procedure (discussed in section 5.5).

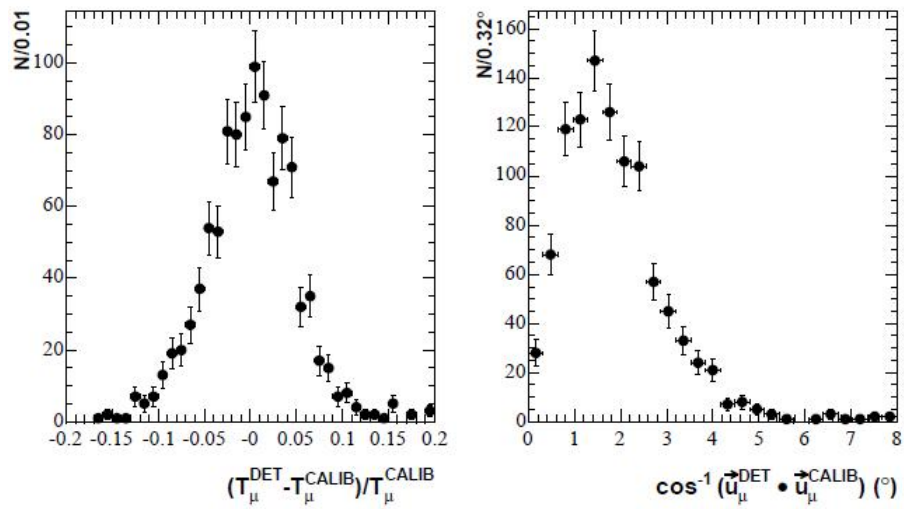


Figure 2.6: Muon energy and angle resolution for muons stopping in the 2 m deep cube ($T_{\mu} = 407\text{MeV}$).

Chapter 3

Event Simulation

As mentioned in section 1.1, a detailed simulation of neutrino events in the detector is needed to perform the cross section ratio measurement. The simulation is needed to obtain values for signal fraction and cut efficiency (see section 5.4) as a function of energy. Additionally, a comparison of true and reconstructed neutrino energies in simulated events is needed in order to unfold the neutrino energy distributions of data events into physically meaningful quantities (see section 5.5). Event reconstruction (chapter 4) also requires a simulation of the detector response to charged particles in the tank.

The event simulation in MiniBooNE is divided into three parts. First, a simulation of the proton beam's interaction with the Beryllium target and the subsequent meson decays produces a prediction for the neutrino flux at MiniBooNE. Second, NUANCE is used to simulate the interactions of neutrinos with protons and neutrons in the mineral oil and nuclear re-interactions of the resulting products. Finally, a detector simulation is used to track the final state products of these interactions and simulate the detector response.

3.1 Neutrino Flux Prediction

A Geant4 [69] Monte Carlo (MC) simulation is used to simulate the interaction of protons with the Beryllium target and the subsequent meson decays. The geometry of this MC

consists of a detailed simulation of the last 50 m of the Booster beamline, the target hall (including the horn), and the 50 m decay region. Magnetic fields, particularly that created by the MiniBooNE horn, are included in the simulation; the horn’s magnetic field is modeled as a $1/R$ field between the inner and outer conductors, with a maximum of 1.5 T at the narrowest point. Electromagnetic and hadronic interactions and decays are taken into account in the tracking of each particle in the simulation.

The MC generates protons 1 cm upstream of the target with random transverse positions and directions drawn from Gaussian distributions. The width of the position distributions is 1.51 mm in the x -direction and 0.75 mm in the y -direction and the width of the directional distributions is 0.66 mrad in the x -direction and 0.40 mrad in the y -direction. A very small number of these protons interact outside the beamline (with the aluminum of the horn, for example), due to the divergence of the beam or to scattering, but most are incident on the beryllium target. Seven types of particles ($\pi^\pm, K^\pm, K^0, p, n$) are generated by the p-Be interactions. These particles are then tracked and any decay products are also propagated through the geometry, with the branching ratios in table 2.1 governing their decays. The output of the simulation is a neutrino flux distribution; whenever a neutrino is produced with a momentum such that it will intersect with the detector, it is added to the distribution.

Customized cross section tables based on the Glauber model [70] are used for interactions of protons, neutrons, and pions with beryllium and aluminum. A customized model, based on external data, is used for particle production in p-Be interactions. The energies involved in these interactions are below the threshold for charm production. However, strange production does occur at these energies, allowing kaons to be created. The products of the p-Be interactions are thus protons, neutrons, pions, and kaons. Proton, neutron, and K^- production are handled by the MARS simulation package [71]; the contribution of K^- to the neutrino flux is expected to be small. Contributions from semi-leptonic hyperon decays, which are simulated using FLUKA [72], are also expected to be small. A Sanford-Wang parametrization [73] is used for π^\pm and K^0 production. This treats these

cross-sections as having the form:

$$\frac{\partial^2 \sigma}{\partial p \partial \Omega} = c_1 p^{c_2} \left(1 - \frac{p}{p_B - c_9} \right) \exp \left(\frac{-c_3 p^{c_4}}{p_B^{c_5}} - c_6 \theta (p - c_7 p_B \cos^{c_8} \theta) \right) \quad (3.1)$$

where p and θ are the momentum and angle of the product meson (in the laboratory frame), p_B is the momentum of the incident beam proton, and c_i are empirically obtained parameters. For pion production, the parameters are chosen to fit data provided by the HARP [74] and BNL E910 [75] experiments. For K^0 production, data from E910 and KEK [76] are used. The parameter c_9 was set to 1.00 in the pion production fits, but was allowed to vary in the kaon fit. The c_3 parameter was also set to 1.00 in the π^+ fit and was varied only in the first iteration of the fit procedure for the π^- fit. This was done because the data used in the fit covered only a limited range of proton momentum, resulting in some strong correlations among the parameters.

Modelling pion production correctly is especially important, as 97% of neutrinos in the detector are predicted to come from the decay of pions. The HARP experiment measured double differential cross-sections (as functions of pion momentum and pion angle) for π^+ and π^- production using 8.89 GeV/c protons incident on replicas of the MiniBooNE beryllium target. The kinematics of the experiment allowed cross-section measurements in the region $0.75 \text{ GeV}/c < p_\pi < 6.5 \text{ GeV}/c$ and $30 \text{ mrad} < \theta_\pi < 210 \text{ mrad}$. The full covariance matrices reported by HARP were used to account for bin-to-bin correlations. The BNL E910 experiment measured the same double differential cross-sections, but with incident protons at four different momenta (6.4, 12.3, 17.5, and 17.6 GeV/c), for $0.4 \text{ GeV}/c < p_\pi < 5.6 \text{ GeV}/c$ and $30 \text{ mrad} < \theta_\pi < 300 \text{ mrad}$. Because a covariance matrix was not reported by E910, uncertainties on each bin were treated as uncorrelated in the MiniBooNE flux prediction.

Neutral kaons are produced in the p-Be interactions with equal K_S^0 and K_L^0 components, the latter of which is important in that its decay produces a ν_e or $\bar{\nu}_e$ about 40% of the time. However, due to both the long decay time of the K_L^0 mesons and their not being

| Product | c_1 | c_2 | c_3 | c_4 | c_5 | c_6 | c_7 | c_8 | c_9 |
|---------|-------|--------|-------|-------|-------|-------|---------|--------|-------|
| π^+ | 220.7 | 1.080 | 1.000 | 1.979 | 1.32 | 5.572 | 0.0868 | 9.686 | 1.00 |
| π^- | 213.7 | 0.9379 | 5.454 | 1.210 | 1.284 | 4.781 | 0.07338 | 8.329 | 1.00 |
| K^0 | 15.13 | 1.975 | 4.084 | 0.928 | 0.731 | 4.362 | 0.048 | 13.300 | 1.278 |

Table 3.1: Sanford-Wang parameters in eq. 3.1 for production of pions and neutral in the p-Be interactions. These were obtained through fits to data from [74, 75, 76]. Further details, including the full covariance matrices, can be found in [66].

| Product | c_1 | c_2 | c_3 | c_4 | c_5 | c_6 | c_7 |
|---------|-------|-------|-------|-------|-------|-------|-------|
| K^+ | 11.70 | 0.88 | 4.77 | 1.51 | 2.21 | 2.17 | 1.51 |

Table 3.2: Feynman scaling parameters in eq. 3.2 for production of positive kaons in the p-Be interactions. These were obtained through fits to data from [77, 78, 79, 80, 81, 82, 83, 84]. Further details, including the full covariance matrices, can be found in [66].

focused by the horn, their contribution to the neutrino flux is small compared to the K^+ .

The K^+ production model is based on a variety of experiments [77, 78, 79, 80, 81, 82, 83, 84] using proton beams with momenta between 9.5 and 24 GeV/ c . Feynman scaling is used to extrapolate these data to the 8.89 GeV/ c Booster beam. The production cross-section in this parametrization is given by:

$$\frac{\partial^2 \sigma}{\partial p \partial \Omega} = \frac{p^2}{E} c_1 \left(a - \frac{p_{\parallel}}{p_{\parallel}^{max}} \right) \exp \left(-c_2 p_T - c_3 \left| \frac{p_{\parallel}}{p_{\parallel}^{max}} \right|^{c_4} - c_5 p_T^2 - c_7 \left| p_T \frac{p_{\parallel}}{p_{\parallel}^{max}} \right|^{c_6} \right) \quad (3.2)$$

where p and E are the momentum and energy of the produced K^+ , p_T is the transverse component of its momentum, p_{\parallel} is the parallel component of its momentum, p_{\parallel}^{max} is the maximal possible parallel momentum for a given interaction (all in the center of mass frame), and c_i are again empirically determined constants.

Using the brute force method of generating protons one by one and recording their neutrino products would be too computationally intensive to produce the MC statistics needed for the experiment. Therefore, several techniques are used to improve the statistics in a computationally efficient way. First, the parent particles of the neutrinos are “redecayed”; whenever a neutrino is produced, the decay of its parent is simulated 1000 at the same position but with kinematics randomly drawn from decay distributions each time. Simi-

larly, every time a muon is produced in the secondary beam, its propagation and possible decay are simulated twenty times; to correct for the resulting overproduction of neutrinos, those neutrinos produced by muon decay are weighted by a factor of $\frac{1}{20}$. To reduce statistical uncertainties in the high energy tail of the neutrino energy distribution, the cross sections for meson production in the p-Be interactions are multiplied by an exponential of the longitudinal meson momentum; the resulting neutrinos are weighted by the inverse of this exponential. These enhancements result in better statistics for neutrinos produced by muons and for those in the high energy tail of the distribution, while preserving the shape of the neutrino flux by virtue of the lower event weights of those neutrinos.

The predicted MiniBooNE flux versus neutrino energy in neutrino mode is shown in figure 3.1. Figure 3.2 shows the contribution to the ν_μ flux from each of the four most important meson-decay channels. As the figure shows, nearly all neutrinos below about 2 GeV are produced by decaying pions; above 3 GeV the flux is dominated by the decay of K^+ , while between 2 and 3 GeV these two sources are both significant.

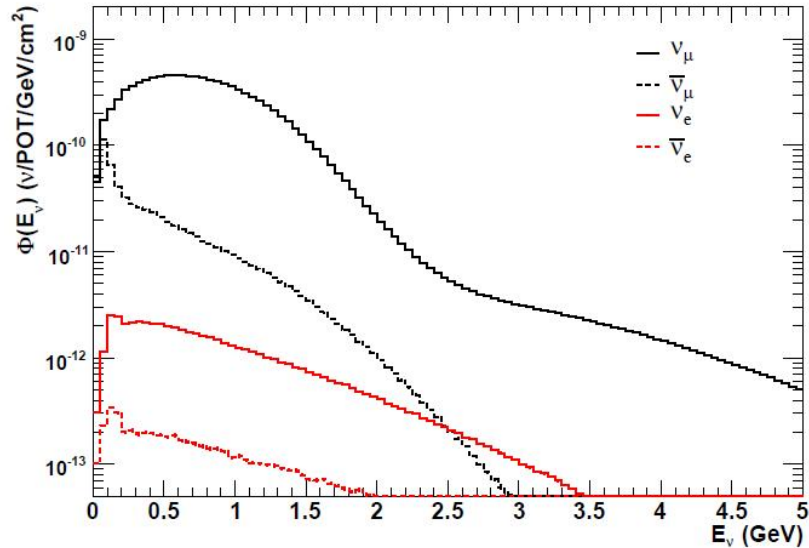


Figure 3.1: The predicted flux by neutrino species in neutrino mode.

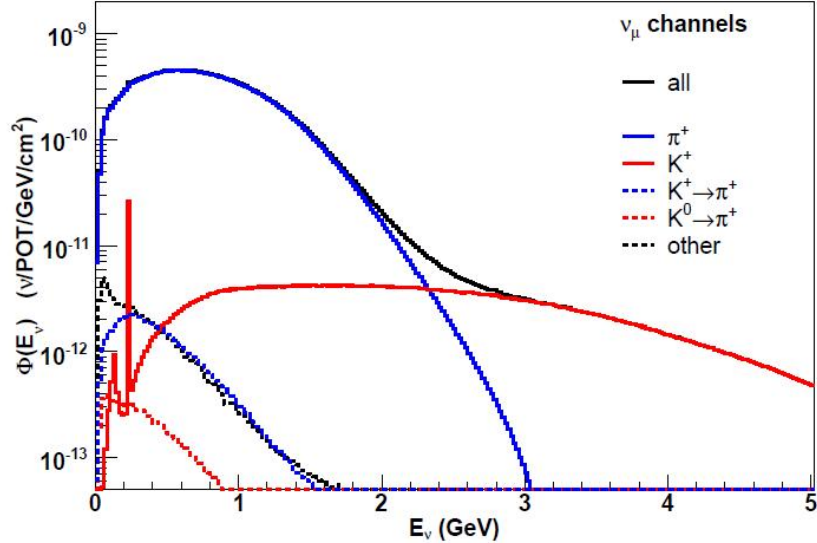


Figure 3.2: The predicted flux of muon neutrinos by parent meson in neutrino mode.

3.2 NUANCE

Neutrino interactions within the detector are simulated with the Fortran-based package NUANCE v3 [85]. The momentum distributions for each neutrino species generated by the beam MC serves as the input to NUANCE. From these distributions, NUANCE generates spectra for each possible channel of neutrino interaction. There are 99 event channels in NUANCE, which is capable of simulating interactions over the wide range of 100 MeV to 1 TeV.

$CCQE$ events are simulated using the Llewellyn-Smith model [44], discussed in section 1.5.2, with the axial mass tuned to $M_A^{eff} = 1.23 \pm 0.20$ GeV for interactions on carbon to fit $\nu_\mu CCQE$ cross-section data [87]. For interactions on hydrogen (i.e. on a free nucleon), an axial mass of $M_A^{eff} = 1.13$ GeV is used. This is essentially a compromise between the MiniBooNE measured value of 1.23 GeV and the consensus value of 1.03 GeV from $CCQE$ measurements on deuterium. Simulation of resonant interactions is based on the Rein-Sehgal model [24] (discussed in section 1.5.1) and simulation of deep inelastic scattering (DIS) is based on the GRV model [88, 89], using parton distribution functions.

In MiniBooNE's mineral oil (CH_2), a small number of neutrino interactions occur on

| Name | Interaction | Contribution |
|-----------------------------|---|--------------|
| <i>CCQE</i> | $\nu_\mu n \rightarrow \mu^- p$ | 40% |
| <i>CCπ^+</i> | $\nu_\mu p(n) \rightarrow \mu^- \pi^+ n(p)$ | 24% |
| <i>NCEl</i> | $\nu_\mu p(n) \rightarrow \nu_\mu p(n)$ | 16% |
| <i>NCπ^0</i> | $\nu_\mu p(n) \rightarrow \nu_\mu \pi^0 p(n)$ | 8% |
| <i>CCπ^0</i> | $\nu_\mu n \rightarrow \mu^- \pi^0 p$ | 4% |
| Other | | 8% |

Table 3.3: The most abundant event channels in MiniBooNE and their contributions to the total number of neutrino events in the detector.

the bare protons of the hydrogen atoms. Most interactions, however, are with a nucleon in a carbon nucleus; in this case, nuclear effects must be taken into account. The nucleus is treated as a relativistic Fermi Gas using the formalism of Smith and Moniz [45] with Fermi momentum $p_F = 220 \pm 30$ MeV/c and binding energy $E_B = 34 \pm 9$ MeV/c². This model results in adjustments to the neutrino cross sections due to Fermi motion. Nuclear shadowing is also taken into account through the Pauli blocking parameter $\kappa = 1.019 \pm 0.011$. The dependence of the predicted cross sections on this nuclear model is considered as a possible source of systematic error in section 5.7.5.

Neutrino interactions are treated as being instantaneous. After simulating the neutrino interaction itself, NUANCE also simulates re-interactions of the products within the target nucleus. The products of the initial interaction are propagated in 0.3 fm steps and at each step are subject to possible hadronic interactions within the nuclear medium. When a particle moves beyond the nuclear radius (2.5 fm for carbon), it is recorded in the final state particle stack. The output of NUANCE consists of a list of these final state particles and their momenta along with truth information concerning the event channel, the energy of the initial neutrino, etc.

3.3 Detector Simulation

A Geant3-based Monte Carlo program [86] is used to simulate particle propagation and interactions in the tank and the detector response. The detector MC takes as input the final

state particle information generated by NUANCE. It then tracks these particles, taking full account of Čerenkov radiation, scintillation, particle decays, and hadronic interactions. Each visible photon radiated (by any process) is tracked individually.

Several modifications have been made to Geant3 for the detector simulation. Models for Dalitz decay of neutral pions ($\pi^0 \rightarrow e^+e^-\gamma$) and muon decay ($\mu \rightarrow e\nu\bar{\nu}$) have been added. Geant3's default simulation of muon capture has also been modified. In the default configuration, Geant3 treats captured muons as simply disappearing; in the MiniBooNE MC the products of muon capture (low energy photons and neutrons) are correctly modelled. The default hadronic interaction model, GFLUKA, has been replaced with GCALOR [90]. This is because the GFLUKA model has been found to significantly overpredict pion charge exchange and underpredict pion absorption when compared with data [91].

The MiniBooNE optical model handles the creation, propagation, and detection of photons in the 250 to 650 nm range using 39 parameters to describe attenuation length, scattering, reflections, PMT efficiencies, scintillation, and fluorescence. The MC allows photon production via Čerenkov radiation, scintillation, or fluorescence and allows the photons to interact in the tank via fluorescence, Rayleigh or Raman scattering, or absorption.

The index of refraction n of the oil used in MiniBooNE was found empirically [92] to be a function of temperature and wavelength:

$$n(\lambda, T) = \left(n_D + C_0 \left(\frac{1}{\lambda^2} - \frac{1}{\lambda_D^2} \right) \right) (1 - C_1(T - T_0)) \quad (3.3)$$

where $\lambda_D = 589.3$ nm (the wavelength of the test laser used), $T_0 = 293.15$ K, $n_D = 1.4684$ (the index of refraction at λ_D and T_0), and C_0 and C_1 are empirically determined constants, 4240 ± 157 nm² and $(3.66 \pm 0.04) \cdot 10^{-4}$ K⁻¹, respectively.

Čerenkov radiation, the primary source of photons producing PMT hits in MiniBooNE, occurs when a charged particle moves faster than the speed of light in the surrounding medium. The oil's index of refraction at 589.3 nm and 293.15 K is 1.4684 ± 0.0002 , resulting in a phase velocity c_n of $\frac{1}{n} = 0.681c \pm 0.0001c$ for light. For a particle with speed v , Čerenkov

radiation is emitted at a characteristic angle:

$$\theta_{Cer} = \arccos\left(\frac{c_n}{v}\right) \quad (3.4)$$

Using the relativistic relation between velocity and kinetic energy T , this can be written as:

$$\theta_{Cer} = \arccos\left(\frac{1}{n} \left[\frac{(T+m)^2}{(T+m)^2 - m^2} \right]^{\frac{1}{2}}\right) \quad (3.5)$$

The Čerenkov threshold, the minimal kinetic energy a particle must have to produce Čerenkov radiation, is for a particle of mass m :

$$T_{Cer} = m \left(\sqrt{\frac{n^2}{n^2 - 1}} - 1 \right) \quad (3.6)$$

The passage of charged particles through the mineral oil also excites or ionizes electrons in the surrounding atoms. The de-excitation of these atoms produces scintillation light. Because the atoms do not de-excite instantaneously, the scintillation light is delayed by a time on the order of tens of nanoseconds. Unlike Čerenkov radiation, scintillation light is isotropic. The scintillation yield is proportional to the energy lost by the particle; however, quenching reduces flux of scintillation light that reaches the phototubes. Birk's law gives the energy flux of scintillation light in relation to the energy loss of the particle responsible:

$$\frac{dE_{sci}}{dx} = \frac{\frac{dE}{dx}}{1 + k_{B1} \frac{dE}{dx} + k_{B2} \left(\frac{dE}{dx}\right)^2} \quad (3.7)$$

The constants $k_{B1} = 0.014 \text{ g cm}^2 \text{ MeV}^{-1}$ and $k_{B2} = 0$ were found empirically.

A further possible source of light is fluorescent molecules in the medium. These molecules may be excited by high energy photons and produce visible wavelength photons in their de-excitations. Spectrofluorometer measurements found four different fluorescers in the mineral oil, with lifetimes ranging from 1 to 33 ns [93], of which one, with a time constant of 33 ns, dominates the fluorescent emission [94]. The time constants and emission

profiles of these fluorescers were measured and are included in the MC simulation.

The processes to which photons propagating through the mineral oil are susceptible in the MC are scattering, absorption, and fluorescence. Photons may scatter either elastically (Rayleigh scattering) or inelastically (Raman scattering). In the case of Rayleigh scattering, the wavelength of the photon is unchanged; in Raman scattering, the photon loses some energy by exciting the molecule on which it scatters. The MC model for Rayleigh and Raman scattering is based on measurements of scattering in Marcol 7 mineral oil [95, 96]. Rayleigh scattering accounts for about 95% of scattering in the oil.

Photons travelling through the oil can also contribute to fluorescence. In this case, rather than being excited by a higher energy photon (as discussed above), a fluorescent molecule may be excited by a visible photon; in this case, fluorescence is effectively a scattering phenomenon rather than a source of visible light. The difference between fluorescence and Raman scattering is that in fluorescence, the initial photon is absorbed completely while in Raman scattering it only loses some of its energy. Fluorescence is thus a resonant process, whereas Raman scattering can occur with light of any frequency. Like Raman scattering, however, fluorescence can shift the wavelength of the scattered light. The response of the fluorophores in the oil was measured as a function of wavelength, and the wavelength shifting is included in the optical

Absorption refers to any process by which a photon is lost without producing secondary photons that are visible to the PMTs. The absorption rate is not measured directly, but measurements were made of the total extinction rate; the absorption rate is defined as the total extinction rate minus the contributions from scattering and fluorescence. Figure 3.3 shows the total extinction rate at 10 cm as well as the contributions of various processes.

Data collected by the strobe trigger is added to the MC to simulate detector activity during periods when the beam is off. This allows the MC events to include hits from radioactivity and any other sources of light not modelled in Geant.

The output of the Geant3 detector simulation is the energy and arrival time of each visible photon that reaches a PMT. This information is passed to a FORTRAN program

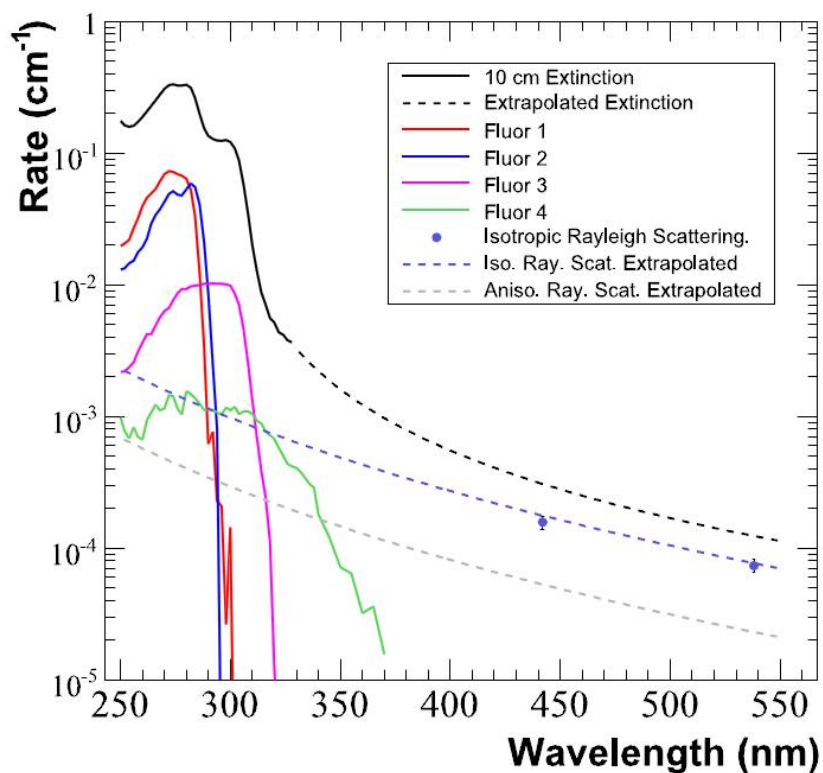


Figure 3.3: Extinction rates in Marcol 7 mineral oil. The black curve indicates the total extinction rate; the coloured curves indicate the contributions of each component. Not shown are the contributions from Raman scattering (which is very small) and from absorption (which is not measured independently, but is assumed to account for the remainder of extinction). The solid curves and data points come from measurements of the oil [95]; the dashed curves are extrapolations.

that convolutes each arriving photon with the charge response function for the appropriate PMT; these response functions were obtained empirically for each individual PMT. The simulated response function is then subjected to an algorithm that duplicates in software the processing performed by the analog-to-digital converter in hardware (discussed in section 2.2.2). The information output by the DAQ simulation is then in exactly the same form as the raw data recorded in the detector.

Chapter 4

Event Reconstruction

4.1 Events and Sub-events

The task of event reconstruction in MiniBooNE is to convert raw PMT data into information on particle tracks and momenta. Each PMT's discriminator can fire, triggering the recording of hit information, at most once every 200 ns. The products of a typical neutrino interaction propagate through the tank for a time on the order of tens of ns before stopping or decaying. Photons produced immediately by these products ("prompt light") can take up to 40 ns to traverse the tank and reach a PMT. The emission of delayed light (e.g. from scintillation) in the detector decays exponentially with a time constant of about 30 ns. Because the time during which light from a given particle is produced is typically shorter than the 200 ns window of the discriminator, each PMT can only register one hit due to that particle.

The raw data available for use in event reconstruction consists of a charge and time value for each of the 1,280 PMTs. From this data, there are seven quantities to be reconstructed for a given final state particle: the 4-vertex of the particle's track (\vec{r}_0, t_0), the direction (θ_0, ϕ_0), and the particle's initial energy (E_0). If a track is approximated as a straight line segment, it can be parametrized with these seven quantities. These track parameters can be thought of as a seven-dimensional vector \vec{x} .

An event in the MiniBooNE detector is defined to comprise all PMT data during the 19.2 μs DAQ window; the data actually coming from light produced by the products of a neutrino interaction typically covers a much shorter time, on the order of a few μs . In practice, the data from an event can be divided into still shorter units called “sub-events”. A sub-event is defined as any group of more than 10 PMT hits with no more than 10 ns between consecutive hits. An event might contain many sub-events or it might contain just one sub-event. Each sub-event typically corresponds to a particle track in the detector. For example, a muon created in a neutrino interaction will propagate through the oil, producing light and triggering PMT hits until it loses enough energy to drop below the Čerenkov threshold. Eventually it will decay, producing an electron; the electron will then briefly radiate and produce PMT hits before dropping below Čerenkov threshold. The cluster of hits associated with the muon will typically constitute one sub-event and the cluster associated with the electron will constitute another. This is illustrated in 4.1, which shows the sub-event structure of a typical $CCQE$ event. The first task in event reconstruction, then, is, for each sub-event, to transform the set \vec{q} and \vec{t} of charge and time data on the PMTs into a track parametrization \vec{x} . Once a track is associated with each sub-event, reconstruction of event kinematics can proceed.

When two Čerenkov-radiating particles are produced simultaneously, both of their tracks will be contained in a single sub-event. This is typically the case, for example, for the muon and the pion in a $CC\pi^+$ event. The Stancu fitters used for this analysis are not capable of resolving two tracks in the same sub-event. In the case of two simultaneous tracks, the more energetic track is reconstructed. This means that in a $CC\pi^+$ event, it is impossible to reconstruct both the muon and the pion. The more energetic track is therefore reconstructed and assumed to be the muon. MC predicts that this will result in a mis-identification of the pion as the muon in roughly 32% of $CC\pi^+$ events. This muon mis-ID ultimately has the effect of a bias in the neutrino energy reconstruction (see section 4.4). This bias is among the effects that the energy unfolding procedure, which will be discussed in section 5.5, is intended to correct.

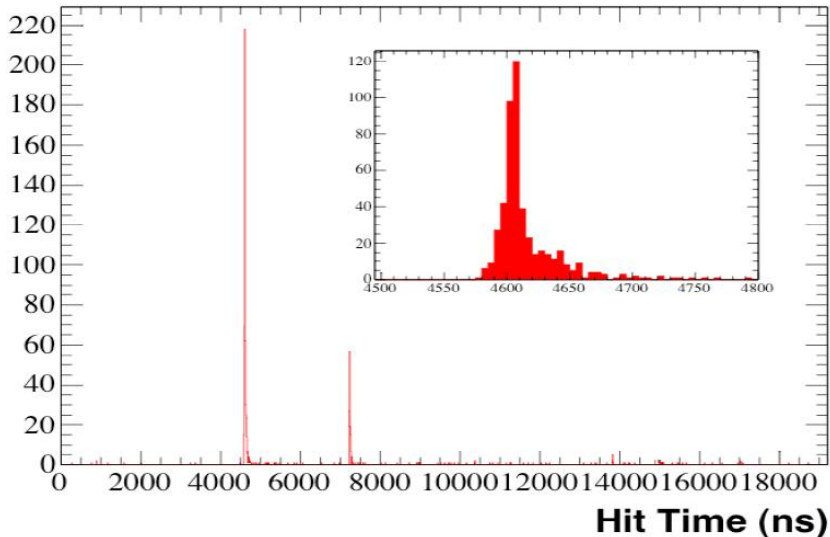


Figure 4.1: The sub-event structure of a typical *CCQE* event. The first cluster of hits corresponds to the muon and the second cluster to the electron produced when the muon decays. The inset shows a closer view of the first sub-event.

A least log likelihood method is used to find the track parameters \vec{x} for a sub-event from the charge and time information \vec{q}, \vec{t} . Conceptually, there are two components to this method: first, an algorithm is needed to predict the probability that \vec{q} and \vec{t} are observed for a given track \vec{x} ; second, the values for \vec{x} that maximize the probability of the observed \vec{q} and \vec{t} must be found. For the latter step, the minimization package MINUIT [97] is used. MINUIT takes as input a function to be minimized, the parameters to be varied, lower and upper limits on each parameter, the step size for each parameter, and the initial guess or “seed” for each parameter. It would be too computationally intensive to simply feed MINUIT all the raw hit information and perform a simultaneous fit for all seven parameters of \vec{x} . Therefore, a series of improving guesses and minimizations is performed, as described in the following sub-sections.

4.2 The S-Fitter

The fitter used for this analysis is the Stancu Fitter or S-Fitter, developed primarily by Ion Stancu. This fitter uses three iterations of the likelihood maximization procedure to

obtain, respectively, the “fast”, “full” and “flux” fits.

4.2.1 Fast Fit

Approximating the source of the light for a sub-event as the point \vec{r}_0 and time t_0 at the beginning of a particle’s track and assuming that only Čerenkov light is produced, one can write the probability that a PMT i measures light at time t_i as a Gaussian with the PMT’s measured time resolution of 1.8 ns as the spread:

$$P_C(t_i|\vec{r}_0, t_0) = \frac{1}{\sqrt{2\pi}\sigma} \exp\left(-\frac{(t_i - t_0 - |\vec{r}_i - \vec{r}_0|/c_n)^2}{2\sigma^2}\right) \quad (4.1)$$

where \vec{r}_i is the position of PMT i and c_n is the speed of light in the oil. The probability for the full set of N PMTs to measure light at a set of times \vec{t} is the product of the individual probabilities for each PMT:

$$P_C(\vec{t}|\vec{r}_0, t_0) = \prod_{i=1}^N \frac{1}{\sqrt{2\pi}\sigma} \exp\left(-\frac{(t_i - t_0 - |\vec{r}_i - \vec{r}_0|/c_n)^2}{2\sigma^2}\right) \quad (4.2)$$

This expression for $P_C(\vec{t}|\vec{r}_0, t_0)$ is called the *time likelihood function*. The Stancu Fast Fit is achieved by maximizing the time likelihood function with respect to the track parameters \vec{r}_0 and t_0 . The fitter is seeded with the charge-averaged position:

$$\vec{r}_0 = \frac{\sum_{i=1}^N q_i \vec{r}_i}{\sum_{i=1}^N q_i} \quad (4.3)$$

where q_i is the number of photons measured by PMT i .

This maximization procedure gives the Fast Fit for \vec{r}_0 and t_0 . The fit time t_0 is used to classify each PMT hit as either prompt (if the hit time is less than 4 ns after t_0) or late (if the hit time is more than 4 ns after t_0). Prompt PMT hits are assumed to be due mainly to Čerenkov light and late PMT hits mainly to scintillation; values for the Čerenkov and scintillation photon fluxes, Φ_C and Φ_s , are thus obtained. Fast Fit values for the θ and ϕ (specifying the particle’s direction) are then obtained simply by taking the charge-averaged

direction of prompt PMT hits with respect to the vertex fit \vec{r}_0 . A Fast Fit value for the energy E of the particle producing the track is obtained from the total charge.

4.2.2 Full Fit

The track parameters obtained by the Fast Fitter are used as the seed values for the Stancu Full Fitter. Whereas the Fast Fitter uses only the time likelihood function, the Full Fitter uses both a modified time likelihood function and a charge likelihood function.

The predicted number of photons (or, equivalently, the predicted charge) measured by a PMT i due to a track with parameters \vec{x} can be written as the sum of contributions from Čerenkov and scintillation light:

$$Q_i = Q_{C,i} + Q_{s,i} \quad (4.4)$$

$$Q_{C,i} = \frac{\epsilon_i}{(\vec{r}_i - \vec{r}_0)^2} \Phi_C(E) F(\cos \theta_i, E) f_C(\cos \eta_i) \exp \left[-\frac{(\vec{r}_i - \vec{r}_0)^2}{\lambda_C} \right] \quad (4.5)$$

$$Q_{s,i} = \frac{\epsilon_i}{(\vec{r}_i - \vec{r}_0)^2} \Phi_s(E) f_s(\cos \eta_i) \exp \left[-\frac{(\vec{r}_i - \vec{r}_0)^2}{\lambda_s} \right] \quad (4.6)$$

where ϵ_i is the PMT quantum efficiency, Φ_C (Φ_s) is the Čerenkov (scintillation) flux of photons, fixed to the values obtained by the Fast Fitter, λ_C (λ_s) is the attenuation length for Čerenkov (scintillation) photons, η_i is the angle of incidence of the light, f_C (f_s) is the PMT response for Čerenkov (scintillation) light, θ_i is the angle between the particle track and the vector pointing from the track's vertex to PMT i , E is the particle's energy, and F is the angular distribution of Čerenkov light.

The probability that PMT i measures a number of photons q_i can be written as a Poisson distribution about the expected value Q_i :

$$P(q_i | \vec{r}_0, t_0, E) = \frac{1}{q_i!} Q_i^{q_i} e^{-Q_i} \quad (4.7)$$

As with the timing likelihood function, we can generalize to the *charge likelihood function*, that is, the probability for the set of N PMTs with expected charges \vec{Q} to actually measure charges \vec{q} by taking the product of the individual probabilities:

$$P(\vec{q}|\vec{r}_0, t_0, E) = \prod_{i=1}^N \frac{1}{q_i!} Q_i^{q_i} e^{-Q_i} \quad (4.8)$$

The time likelihood function $P_C(t_i|\vec{r}_0, t_0)$ given in eq. 4.1 assumed that only Čerenkov light (prompt light) was produced. A corresponding time likelihood function P_s that assumes only scintillation light (late light) can be constructed simply by convolving the expression for P_C with an exponential decay as a function of time. The full time likelihood for an individual PMT can be written using these two terms and the predicted Čerenkov and scintillation charge for the PMT:

$$P(t_i|\vec{r}_0, t_0) = \frac{Q_{C,i}}{Q_i} P_C(t_i|\vec{r}_0, t_0) + \frac{Q_{s,i}}{Q_i} P_s(t_i|\vec{r}_0, t_0) \quad (4.9)$$

The Full Fitter obtains the track parameters \vec{r}_0 and t_0 by maximizing the *total likelihood function*, which is just the product of the charge likelihood (eq. 4.7) and the improved time likelihood (eq. 4.9):

$$P(\vec{q}, \vec{t}|\vec{r}_0, t_0, E) = \prod_{i=1}^N P(t_i|\vec{r}_0, t_0) P(q_i|\vec{r}_0, t_0, E) \quad (4.10)$$

The Full Fit direction and energy are then obtained in the same way as in the Fast Fit, but using the new 4-vertex.

4.2.3 Flux Fit

The final stage of the S-Fitter is the Flux Fit. In this step, the values for \vec{r}_0 , t_0 , θ , and ϕ are held constant while the Čerenkov and scintillation light strengths Φ_C and Φ_s are varied. A new value for the energy E of the particle is then obtained using the fit values for Φ_C and Φ_s .

4.2.4 Electron-like and Muon-like Sub-events

As noted above, the discussion of the S-Fitter so far has assumed that the source of light for a sub-event is point-like. This is a good approximation in the case that the light is produced by an electron, which Čerenkov radiates only briefly. It is not, however, a good approximation for many other particles; a muon, for example, typically has a long track and Čerenkov radiates for a comparatively long time. The reconstruction scheme described above, in which a point-like source is assumed, is therefore the reconstruction scheme for the so-called “electron hypothesis”, that is, the hypothesis that the particle responsible for the sub-event is an electron or positron.

A modified reconstruction scheme exists for the corresponding “muon hypothesis”. This scheme is the same as that described above, except that the light is assumed to come from two point-like sources located symmetrically about the mid-point of the particle’s track, with each source responsible for half of the Čerenkov and half of the scintillation light detected by the PMTs. This introduces an additional parameter, the length of the track (or, in this model, the distance between the two sources) for which the fitter extracts a value. The Fast, Full, and Flux fits are then performed just as for the electron hypothesis, but with this additional parameter also varied in the likelihood maximizations.

For each sub-event, a fit is performed using both the electron hypothesis and the muon hypothesis. A comparison of the likelihood functions with the best fit for each hypothesis is used to determine whether the sub-event is electron-like or muon-like; the fit values from the appropriate hypothesis are then used for subsequent stages of reconstruction and analysis.

4.3 The P-Fitter

The P-Fitter was developed primarily by Ryan Patterson. While most of this analysis uses the S-Fitter, the P-Fitter is used for an alternative reconstruction study described in section 5.7.2. The primary differences between the P-Fitter and the S-Fitter are described

here; a full description of the P-Fitter can be found in [94]

The P-Fitter assumes that the source of light observed for a sub-event is a line segment corresponding to the track the particle responsible. This is in contrast to the S-Fitter, which approximates a track with one or two point-like sources. Čerenkov radiation and scintillation along the track is allowed to be non-uniform, but for each process the probability density for emission $\rho(s, E)$ is assumed to be a function only of the distance s from the event vertex and the initial energy E of the particle. This density is normalized to $\int_{-\infty}^{\infty} \rho(s, E) ds = 1$. Using these probability densities, we can write new expressions for the predicted charge $Q_{C,i}$ and $Q_{s,i}$ measured by PMT i due to Čerenkov and scintillation light as integrals over the particle's path:

$$Q_{C,i} = \Phi_C(E)\epsilon_i \int_{-\infty}^{\infty} \rho_C(s, E) F(\cos \theta_i, s, E) f_C(\cos \eta_i) \frac{T(\vec{r})}{(\vec{r}_i - \vec{r})^2} ds \quad (4.11)$$

$$Q_{s,i} = \Phi_s(E)\epsilon_i \int_{-\infty}^{\infty} \rho_s(s, E) f_s(\cos \eta_i) \frac{T(\vec{r})}{(\vec{r}_i - \vec{r})^2} ds \quad (4.12)$$

where \vec{r} is the vector pointing from the center of the tank to point s along the track, $T(\vec{r})$ is the transmission of light through the oil and glass (which was assumed to be an exponential decay in equations 4.5 and 4.6), and other terms are as defined in section 4.2. Note that \vec{r} , η , and θ are now implicitly functions of s , which parametrizes the track. F , the Čerenkov emission profile, is also allowed to depend explicitly on s ; that is, the emission profile changes as the particle propagates and loses energy. Note also that while we integrate from negative to positive infinity, $\rho(s, E)$ will be non-zero only between the track vertex ($s = 0$) and the point at which the particle either ceases to radiate or exits the detector.

Computing these integrals for each PMT would make the likelihood maximization unacceptably slow. Therefore, an approximation is used. We begin by defining an effective acceptance, $J(s)$, which absorbs all the terms in the integrand except the emission probability density and the Čerenkov emission profile:

$$J_C(s) = \epsilon_i f_C(\cos \eta_i) \frac{T(\vec{r})}{(\vec{r}_i - \vec{r})^2} \quad (4.13)$$

$$J_s(s) = \epsilon_i f_s(\cos \eta_i) \frac{T(\vec{r})}{(\vec{r}_i - \vec{r})^2} \quad (4.14)$$

We then approximate $J(s)$ with a parabola:

$$J_C(s) = j_{0,C} + j_{1,C}s + j_{2,C}s^2 \quad (4.15)$$

$$J_s(s) = j_{0,s} + j_{1,s}s + j_{2,s}s^2 \quad (4.16)$$

The predicted charges for Čerenkov and scintillation light, then, are:

$$Q_{C,i} = \Phi_C(E) \left(j_{0,C} \int_{-\infty}^{\infty} \rho_s(s, E) F(\cos \theta_i, s, E) ds + j_{1,C} \int_{-\infty}^{\infty} \rho_s(s, E) F(\cos \theta_i, s, E) s ds + j_{2,C} \int_{-\infty}^{\infty} \rho_s(s, E) F(\cos \theta_i, s, E) s^2 ds \right) \quad (4.17)$$

$$Q_{s,i} = \Phi_s(E) \left(j_{0,s} \int_{-\infty}^{\infty} \rho_s(s, E) ds + j_{1,s} \int_{-\infty}^{\infty} \rho_s(s, E) s ds + j_{2,s} \int_{-\infty}^{\infty} \rho_s(s, E) s^2 ds \right) \quad (4.18)$$

The integrands in the scintillation equation now depend only on E . The integrands in the Čerenkov equation also depend on $\theta_i(s)$, the angle between the particle's direction and a line connecting the particle with PMT i , which in turn depends on the distance $|\vec{r}_0 - \vec{r}_i|$ between the track's vertex and PMT i and on the initial angle $\theta_i(0)$. The integrals, then, depend on three parameters, and can be computed ahead of time for various values of these parameters. Rather than evaluating an integral for each PMT at each step of the maximization, a table of these pre-computed values is consulted.

The P-Fitter then proceeds in much the same way as the S-Fitter, but using the more detailed charge predictions in equations 4.17 and 4.18. The P-Fitter reconstructs muons slightly better than the S-Fitter, but runs about ten times more slowly. For a comparison of the S-Fitter and P-Fitter in the ratio analysis, see section 5.7.2

4.4 Reconstruction of Event Kinematics

The neutrino energy E_ν of an event is reconstructed using the muon energy and direction obtained from the Stancu fitters. For events in the $CC\pi^+$ sample, it is the StancuFlux fit for muon energy that is used in this reconstruction; for the larger $CCQE$ sample, the faster StancuFull fit is used. This results in a bias that makes the reconstructed neutrino energies for the two samples incommensurable. This difficulty is overcome by the energy unfolding scheme (see section 5.5), which is applied separately to each sample. A check of the analysis was also performed using the StancuFull fit for muon energy in the $CC\pi^+$ as well as the $CCQE$ sample; this variation showed a negligible difference in the resulting cross-section ratio as compared to the main result (see section 5.7.2).

Treating the interaction as a two-body collision and assuming that the target nucleon is at rest within the nucleus and the incident neutrino is moving in the z-direction, we can write the neutrino energy for an event as:

$$E_\nu = \frac{1}{2} \frac{2m_p E_\mu + m_1^2 - m_p^2 - m_\mu^2}{m_p - E_\mu + \cos \theta_\mu \sqrt{E_\mu^2 - m_\mu^2}} \quad (4.19)$$

where θ_μ is the angle of the muon with respect to the z-axis, E_μ is the energy of the muon, m_μ is the mass of the muon, m_p is the mass of the proton, and m_1 is the mass of the neutron for $CCQE$ events and the mass of the nucleon resonance for $CC\pi^+$ events. For the purpose of neutrino energy reconstruction, the resonance is assumed to be the $\Delta(1232)$ for all $CC\pi^+$ events.

Note that by treating all events as two-body collisions, we are ignoring the effect of the pion on event kinematics in $CC\pi^+$ events. This approximation is necessary because the pion cannot be reconstructed using the standard fitters. Including the pion, the kinematics for a $CC\pi^+$ event would give:

$$E_\nu = \frac{1}{2} \frac{2m_p(E_\mu + E_\pi) - 2p_\mu \cdot p_\pi + m_1^2 - m_p^2 - m_\mu^2}{m_p - E_\mu - E_\pi + \cos \theta_\mu \sqrt{E_\mu^2 - m_\mu^2} + \cos \theta_\pi \sqrt{E_\pi^2 - m_\pi^2}} \quad (4.20)$$

The systematic effect of the use of eq. 4.19 instead of 4.20 on the $CC\pi^+$ reconstructed energy distribution is one of the smearing effects that our energy unfolding procedure (section 5.5) is intended to correct.

Chapter 5

$CC\pi^+$ to $CCQE$ Cross Section Ratio

5.1 Analysis Method

The cross-section for a neutrino interaction α is defined as:

$$\sigma_\alpha = \frac{N_\alpha}{\Phi_\nu T N_{targets}} \quad (5.1)$$

where N_α is the true number of events of type α , $N_{targets}$ is the number of nuclear targets in the detector, T is the length of time during which neutrinos are incident on the target, and Φ_ν is the flux of incident neutrinos.

Because the incident neutrino flux and the number of nuclear targets are fixed properties of the beam and the detector (i.e. independent of the process we are considering), $N_{targets}$ and Φ_ν must be the same for any two processes α and β (where α and β are, for instance, $CC\pi^+$ and $CCQE$). Therefore we can write the ratio of the α and β cross-sections as:

$$\frac{\sigma_\alpha(E_\nu)}{\sigma_\beta(E_\nu)} = \frac{N_\alpha(E_\nu)}{N_\beta(E_\nu)}. \quad (5.2)$$

Note that in writing the cross sections and numbers of events as functions of E_ν only,

we are implicitly integrating over Q^2 and $\cos(\theta_\mu)$.

For a given process α and a given set of cuts associated with α , we can relate the number of events passing those cuts, $N_{\alpha-cuts}$, to the true number of events of type α present in the data, N_α , with:

$$N_{\alpha-cuts} = f_\alpha^{-1} * \epsilon_\alpha * N_\alpha \quad (5.3)$$

where f_α is the signal fraction and ϵ the cut efficiency for process α and the given cuts. The signal fraction is defined as the fraction of events $N_{\alpha-cuts}$ that are also true α events; the cut efficiency is defined as the fraction of true α events N_α that also pass the cuts. In other words, if we denote true α events that pass the α cuts as $N_{\alpha-cuts,\alpha}$, then:

$$f_\alpha = \frac{N_{\alpha-cuts,\alpha}}{N_{\alpha-cuts}} \quad (5.4)$$

$$\epsilon_\alpha = \frac{N_{\alpha-cuts,\alpha}}{N_\alpha} \quad (5.5)$$

Given a set of events that pass cuts, we can find the true number of events N_α , if f_α and ϵ_α are known:

$$N_\alpha = \epsilon_\alpha^{-1} * f_\alpha * N_{\alpha-cuts} \quad (5.6)$$

We can apply this relation independently to each energy bin. However, because the reconstructed energy we measure for the $N_{\alpha-cuts}$ events differs from the true energy, in order to make the relation useful we must include an energy unfolding correction. Therefore we write the relation between the true number of α events in the i th true energy bin, $N_{\alpha,i}$, and the number of events passing cuts in the j th reconstructed energy bin, $N_{\alpha-cuts,j}$ (we will use index i to refer to true energy bins and j to refer to reconstructed bins throughout) as:

$$N_{\alpha,i} = \epsilon_{\alpha,i}^{-1} * \sum_j U_{ij} * f_{\alpha,j} * N_{\alpha-cuts,j} \quad (5.7)$$

where $f_{\alpha,j}$ and $\epsilon_{\alpha,i}$ are now the signal fraction and cut efficiency for the appropriate reconstructed and true energy bins, respectively. U_{ij} , the energy unfolding correction, is defined by this equation; it is a matrix that acting on a reconstructed energy distribution returns the corresponding true energy distribution. For now, we'll just assume that such a matrix exists; in section 5.5, the method of actually constructing U_{ij} will be discussed.

Note that while the signal fractions are defined as functions of reconstructed energy, the cut efficiencies must be defined in terms of true energy, because for events that are not reconstructed, no reconstructed energy is defined. Therefore, we apply the signal fraction correction before and the cut efficiency correction after unfolding.

Thus, we can write the ratio of the α to β cross-sections for energy bin i as:

$$R_i = \frac{\sigma_{\alpha,i}}{\sigma_{\beta,i}} = \frac{\epsilon_{\alpha,i}^{-1} * \sum_j U_{ij} * f_{\alpha,j} * N_{\alpha-cuts,j}}{\epsilon_{\beta,i}^{-1} * \sum_j U_{ij} * f_{\beta,j} * N_{\beta-cuts,j}} \quad (5.8)$$

Plugging in the definitions of signal fraction and cut efficiency, the ratio can be rewritten purely in terms of numbers of events in data and Monte Carlo:

$$R_i = \frac{\sigma_{\alpha,i}}{\sigma_{\beta,i}} = \frac{\frac{N_{\alpha,i}^{MC}}{N_{\alpha-cuts,\alpha,i}^{MC}} * \sum_j U_{ij} * \frac{N_{\alpha-cuts,\alpha,j}^{MC}}{N_{\alpha-cuts,j}^{MC}} * N_{\alpha-cuts,j}^{Data}}{\frac{N_{\beta,i}^{MC}}{N_{\beta-cuts,\beta,i}^{MC}} * \sum_j U_{ij} * \frac{N_{\beta-cuts,\beta,j}^{MC}}{N_{\beta-cuts,j}^{MC}} * N_{\beta-cuts,j}^{Data}}}{\quad} \quad (5.9)$$

5.2 Observed and FSI-Corrected Ratios

So far we have spoken in a general way of measuring the ratio between two cross sections α and β . In this analysis, we are interested in $CC\pi^+$ processes: $\nu_\mu p \rightarrow \mu^- p\pi^+$ (NUANCE channel 3), $\nu_\mu n \rightarrow \mu^- n\pi^+$ (NUANCE channel 5), and $\nu_\mu A \rightarrow \mu^- A\pi^+$ (NUANCE channel 97); and the $CCQE$ process: $\nu_\mu n \rightarrow \mu^- n$. We must, however, carefully decide exactly what we are measuring before we define what counts as a signal event for each of these processes.

For our primary measurement, we define “effective” $CC\pi^+$ and $CCQE$ (or $CC\pi^+$ -like and $CCQE$ -like) signal events as follows:

Effective $CC\pi^+$:

1. Final state particles (FSP) must include one μ^- and no other muons.
2. FSP must include one π^+ and no other pions.
3. FSP must not include any hadrons other than protons, neutrons, or pions.

Effective $CCQE$:

1. FSP must include one μ^- and no other muons.
2. FSP must not include any hadrons other than protons or neutrons.

“Final state particles” here refers to particles that emerge from the target nucleus. Note that it does not include additional particles subsequently produced in detector.

The $CC\pi^+$ -like to $CCQE$ -like cross section ratio is then found according to equation 5.9. The ratio found this way is called the observable cross section ratio. This amounts to a measurement of events as they appear after any nuclear re-interactions take place. This result is not corrected for nuclear effects and is thus independent of any model for such re-interactions.

The composition of effective $CC\pi^+$ and $CCQE$ samples, before cuts, is shown in figure 5.1. The effective $CC\pi^+$ sample consists primarily of $CC\pi^+$ events, with small but significant contributions from DIS and multi-pion events at higher energies. Effective $CCQE$ events are, likewise, primarily $CCQE$ with additional contributions from $CC\pi^+$ resonant and, to a lesser extent, $CC\pi^0$. Figure 5.2 compares the effective and true Monte Carlo samples in generated neutrino energy, before cuts. Note that there are fewer effective than true $CC\pi^+$ events at all energies, whereas there are more effective than true $CCQE$ events above 0.6 GeV (and roughly equal numbers below 0.6 GeV). Taken together with the effective sample composition plots, these indicate that the dominant effect driving the difference between true to effective samples is that a large number of true $CC\pi^+$ events

are effective $CCQE$ events. These are presumably events in which the pion is absorbed in the nucleus.

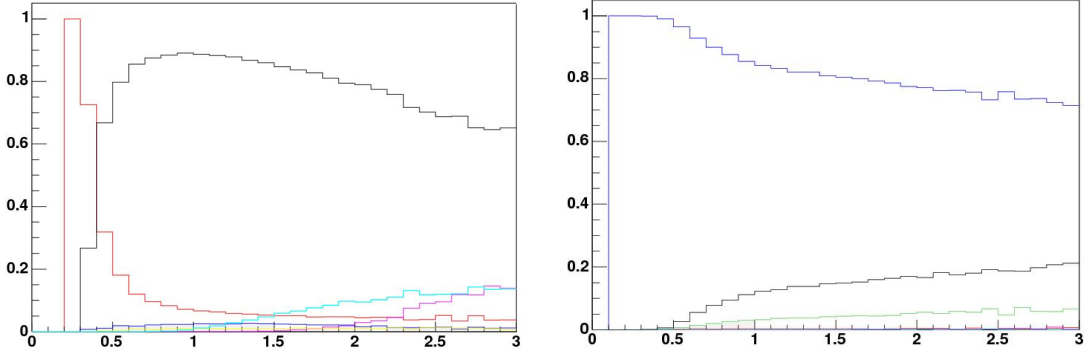


Figure 5.1: Composition of effective $CC\pi^+$ (left) and $CCQE$ (right) events before cuts vs. generated neutrino energy. Black: $CC\pi^+$ resonant, red: $CC\pi^+$ coherent, dark blue: $CCQE$, purple: DIS, light blue: multi-pion, green: $CC\pi^0$.

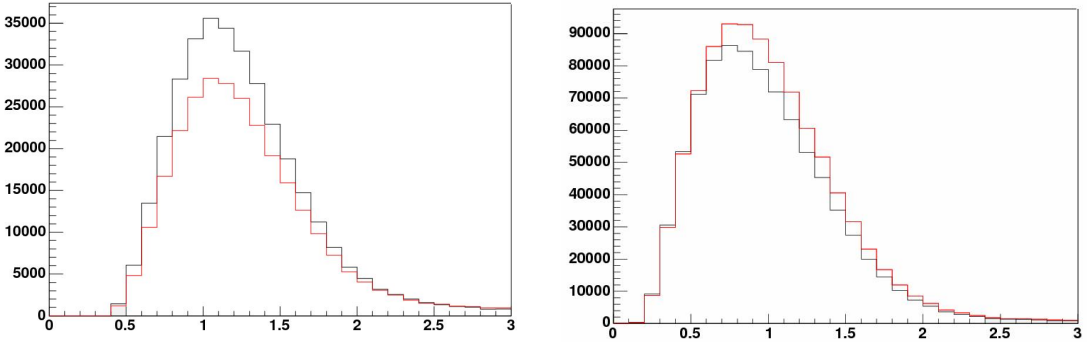


Figure 5.2: Effective (red) and true (black) samples of $CC\pi^+$ (left) and $CCQE$ (right) before cuts, vs. generated neutrino energy.

Prior experiments [55, 57, 59], however, have all reported measurements in which the effects of final state interactions (FSI) in the target nucleus have been removed using MC. Solely for the purpose of comparison, we extracted a similar FSI-corrected ratio. In this case, we define $CC\pi^+$ and $CCQE$ signal events based on the NUANCE channel by which the events were produced. NUANCE channels 3, 5, and 97 are defined as $CC\pi^+$ signal and NUANCE channel 1 is defined as $CCQE$ signal. Thus, the FSI-corrected measurement is a measurement of the cross section ratio at the initial event vertex, before any hadronic re-interactions. The signal fractions and cut efficiencies for the FSI-corrected ratio include

corrections for intra-nuclear hadron re-scattering based on the MC’s model for nuclear effects. It must be noted that this is not in any way an independent measurement from the observed ratio discussed above; the difference between the two results comes entirely from the nuclear model assumed in the MC. The FSI-corrected measurement is made only in order to allow a comparison with previous measurements.

The MC’s model for hadronic re-interactions depends on parameters with associated uncertainties. The corrections for final state interactions, therefore, introduces new systematic uncertainty into the FSI-corrected result. These systematic errors are discussed in section 5.6.

5.3 Event Selection

CCQE events can be identified in the MiniBooNE data by looking for the outgoing muon and the electron to which it decays at the end of its track (the “Michel electron”). *CCQE* events should therefore include exactly two sub-events, one each for the muon and Michel electron. The requirement that we see the Michel electron means that our *CCQE* sample will include fully contained events only (that is, events in which the muon decays before leaving the tank).

The *CCQE* cuts were chosen to maximize the efficiency of the sample while also minimizing background. Note that it was the efficiency and purity of the total sample that were considered in optimizing the selection; the purity and efficiency in any given energy bin might not be optimal with these cuts. The following cuts are used to select this sample:

1. Exactly two sub-events
2. First sub-event in beam window ($4400 < \text{SplitEvent_aveTTim} < 6400$)
3. Veto region hits < 6 for both sub-events
4. Distance between Michel electron and end of muon track < 100 cm.
5. Signal region (“tank”) hits > 200 for first sub-event and < 200 for second sub-event

6. $R < 500$ cm. for first sub-event, where R is the distance of the muon vertex from the center of the tank.

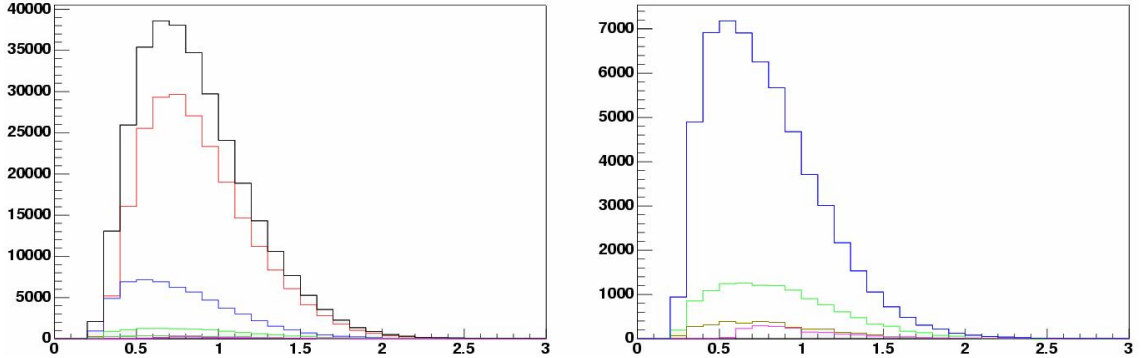


Figure 5.3: *CCQE* Box After Cuts vs. E_{gen} (GeV) (Monte Carlo). *Left: all events; right: only background.* Black: total, red: *CCQE*, blue: $CC\pi^+$ resonant, gold: $CC\pi^+$ coherent, green: $CC\pi^0$, purple: Multi-pion

Figure 5.3 shows the composition of the *CCQE* box after cuts. Table 5.1 shows the fractional contributions of the most important processes to the *CCQE* box, dividing each process into *CCQE*-like and non-*CCQE*-like events. As we would expect, $CC\pi^+$ resonant events constitute by far the most important background for *CCQE*. The MC used for this analysis contains 516,643 true *CCQE* events for $5.579\text{E}20$ protons on target. 181,379 events pass the *CCQE* cuts and 134,226 of the events passing cuts are true *CCQE*. The *CCQE* data sample after cuts contains 195,482 events.

$CC\pi^+$ events are identified by tagging the outgoing muon, the Michel electron at the end of its track, and the Michel electron produced by the pion. As with the *CCQE* sample, the requirement that we see the Michel at the end of the muon track means that we select only fully contained events. Note that the events we refer to as $CC\pi^+$ here actually include two quite distinct processes: resonant pion production, in which a neutrino interacts with a nucleon to produce a Δ^+ or a Δ^{++} which then decays to produce a pion, and coherent pion production, in which the pion is produced via the reaction of a neutrino with the nucleus.

As with *CCQE*, the $CC\pi^+$ cuts were chosen to maximize the total purity and efficiency

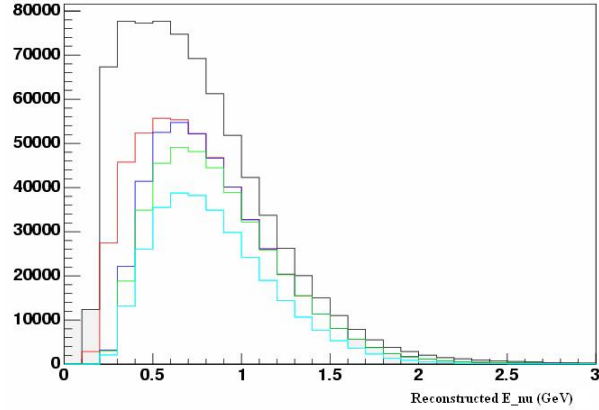


Figure 5.4: Effects of Cuts on $CCQE$ sample in E_{rec} (GeV) (Monte Carlo). *Black: 2 sub-events and beam window cuts, red: v_{cut} , dark blue: t_{cut} , green: R cut, light blue: all cuts*

of the sample. The $CC\pi^+$ sample uses the following cuts:

1. Exactly three sub-events
2. First sub-event in beam window ($4400 < \text{SplitEvent_aveTTim} < 6400$)
3. Veto region hits < 6 for all sub-events
4. Signal region hits > 175 for first sub-event
5. $20 < \text{Signal region hits} < 200$ for subsequent sub-events
6. $r_{nu} < 500$ cm., $r_{mi1} < 500$ cm., $r_{mi2} < 500$ cm, where r_{nu} is the distance of the interaction vertex from the center of the tank and r_{mi1} and r_{mi2} are the distances of the two Michel electrons from the center of the tank.
7. Distance from closest Michel electron to end of muon track < 150 cm.

Figure 5.5 shows the composition of the $CC\pi^+$ box after cuts. Table 5.2 gives the fractional contributions of the most important processes to the $CC\pi^+$ box. Note that while the coherent distribution is here shown separately from the resonant (and is included for comparison in the plot showing the backgrounds) it is properly a contribution to the signal, not to the background, in this analysis. The background is dominated by $CCQE$

| Process | Channels | Percent of Box |
|--|--------------|----------------|
| <i>CCQE</i> (CCQE-like) | 1 | 72.3 |
| <i>CCπ⁺</i> Resonant (CCQE-like) | 3, 5 | 8.0 |
| <i>CCπ⁺</i> Coherent (CCQE-like) | 97 | 0.2 |
| <i>CCπ⁰</i> (CCQE-like) | 4 | 2.1 |
| Multi-pion (CCQE-like) | 17-26, 79-84 | 0.02 |
| DIS (CCQE-like) | 91, 92 | < 0.01 |
| Other (CCQE-like) | | 2.1 |
| <i>CCQE</i> (not CCQE-like) | 1 | 1.5 |
| <i>CCπ⁺</i> Resonant (not CCQE-like) | 3, 5 | 10.6 |
| <i>CCπ⁺</i> Coherent (not CCQE-like) | 97 | 0.9 |
| <i>CCπ⁰</i> (not CCQE-like) | 4 | 1.8 |
| Multi-pion (not CCQE-like) | 17-26, 79-84 | 0.6 |
| DIS (not CCQE-like) | 91, 92 | 0.04 |
| Other (not CCQE-like) | | 3.8 |

Table 5.1: Composition of the *CCQE* sample. In the measurement of the observed cross section ratio, rows 1-7 (CCQE-like) are defined as *CCQE* signal events. In the measurement of the FSI-corrected ratio, rows 1 and 8 are defined as *CCQE* signal.

and (at lower reconstructed energies) by multi-pion resonant processes. Figure 5.6 shows the effect of each cut on the distribution of true Monte Carlo *CCπ⁺* events. The MC sample contains a total of 308,352 *CCπ⁺* events for 5.579E20 protons on target. 42,390 MC events pass the *CCπ⁺* cuts, of which 36,844 are true *CCπ⁺* events. The *CCπ⁺* data sample after cuts contains 46,649 events.

5.4 Signal Fraction and Cut Efficiency

To obtain the signal fraction and cut efficiency for the *CCπ⁺* and *CCQE* samples, we pass a sample of Monte Carlo events through the reconstruction, perform the event selection cuts, and compare the results with the truth information. From their definitions (given in section 5.1), we see that:

$$f_{\alpha,j} = \frac{N_{\alpha-cuts,\alpha,j}}{N_{\alpha-cuts,j}} \quad (5.10)$$

$$\epsilon_{\alpha,i} = \frac{N_{\alpha-cuts,\alpha,i}}{N_{\alpha,i}} \quad (5.11)$$

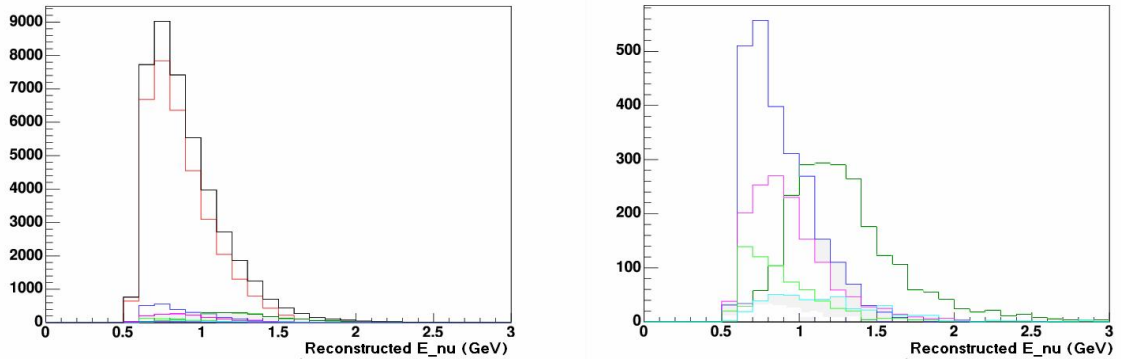


Figure 5.5: $CC\pi^+$ Box After Cuts vs. E_{gen} (GeV) (Monte Carlo). *Left: all events; right: only non-resonant contributions. Black: total, red: $CC\pi^+$ resonant, blue: $CC\pi^+$ coherent, dark green: $CCQE$, purple: Multi-pion resonant, light green: $CC\pi^0$, light blue: DIS*

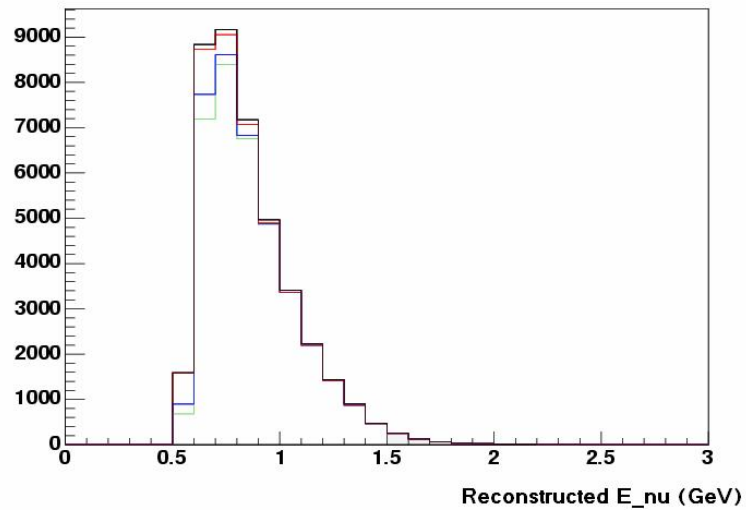


Figure 5.6: Effects of Cuts on $CC\pi^+$ sample in E_{rec} (GeV) (Monte Carlo). *Black: 3 sub-events and beam window cuts, red: v_{cut} , blue: t_{cut} , green: all cuts.*

| Process | Channels | Percent of Box |
|---|--------------|----------------|
| $CCQE$ ($CC\pi^+$ -like) | 1 | 2.2 |
| $CC\pi^+$ Resonant ($CC\pi^+$ -like) | 3, 5 | 80.4 |
| $CC\pi^+$ Coherent ($CC\pi^+$ -like) | 97 | 5.9 |
| $CC\pi^0$ ($CC\pi^+$ -like) | 4 | 0.9 |
| Multi-pion ($CC\pi^+$ -like) | 17-26, 79-84 | 2.4 |
| DIS ($CC\pi^+$ -like) | 91, 92 | 0.2 |
| Other ($CC\pi^+$ -like) | | 1.1 |
| $CCQE$ (not $CC\pi^+$ -like) | 1 | 3.0 |
| $CC\pi^+$ Resonant (not $CC\pi^+$ -like) | 3, 5 | 1.2 |
| $CC\pi^+$ Coherent (not $CC\pi^+$ -like) | 97 | 0.02 |
| $CC\pi^0$ (not $CC\pi^+$ -like) | 4 | 0.6 |
| Multi-pion (not $CC\pi^+$ -like) | 17-26, 79-84 | 1.4 |
| DIS (not $CC\pi^+$ -like) | 91, 92 | 0.3 |
| Other (not $CC\pi^+$ -like) | | 1.9 |

Table 5.2: Composition of the $CC\pi^+$ sample. In the measurement of the observed cross section ratio, rows 1-7 ($CC\pi^+$ -like) are defined as $CC\pi^+$ signal events. In the measurement of the FSI-corrected ratio, rows 2, 3, 9, and 10 are defined as $CC\pi^+$ signal.

where a subscript $\alpha - cuts$ denotes events that pass the cuts associated with process α , a subscript α denotes true α events, and the combined subscript denotes true α events that pass the α cuts.

We can obtain all the distributions necessary to calculate f_α and ϵ_α for both $CC\pi^+$ and $CCQE$ by comparing truth and reconstructed information from the Monte Carlo. Figures 5.7 and 5.8 show these distributions; figures 5.9 and 5.10 show the resulting signal fractions and cut efficiencies. The effect of each cut on signal fraction and efficiency is shown in figures 5.11 and 5.12 and tables 5.3 and 5.4.

To see how features of the signal fraction plots arise, figure 5.9 may be compared with figures 5.3 and 5.5, which show the box compositions. The drop in $CC\pi^+$ signal fraction as one moves to higher E_ν is largely due to the $CCQE$ background, which peaks around 1.25 GeV and falls off more slowly than the signal events. The low signal fraction at high E_ν is not a big concern, as this region is of limited use in any case due to low statistics in the data. The $CCQE$ signal fraction, on the other hand, is nearly flat at about 0.8 except for a precipitous drop at very low E_ν ; figure 5.3 indicates that this occurs because

the $CCQE$ events fall off much more quickly than $CC\pi^+$ (the largest background at all energies) at low E_ν , so that the signal is swamped. Above about 0.6 GeV, the $CC\pi^+$ background becomes roughly proportional to the $CCQE$ signal, so signal fraction remains more or less constant. The sharp drop at low energies is not cause for concern because $CC\pi^+$ events are not reconstructed below 0.5 GeV, so this region of the $CCQE$ box does not end up being used in the ratio analysis.

The cut efficiency plots may be compared with figures 5.4 and 5.6, which show the effects of each cut on the samples. As one might expect, the tank hits cut for the first sub-event ($thits > 175$ and $thits > 200$ for $CC\pi^+$ and $CCQE$ respectively) tends to remove low-energy events. The fact that we require full containment of the events (through $vhits$ and sub-event cuts), on the other hand, tends to remove high-energy events. Thus the shapes of the cut efficiency plots for $CCQE$ and $CC\pi^+$ are very similar: both peak a little below 1 GeV, drop off quickly below this due to the $thits$ requirement, and drop off more slowly in the other direction due to the containment requirement.

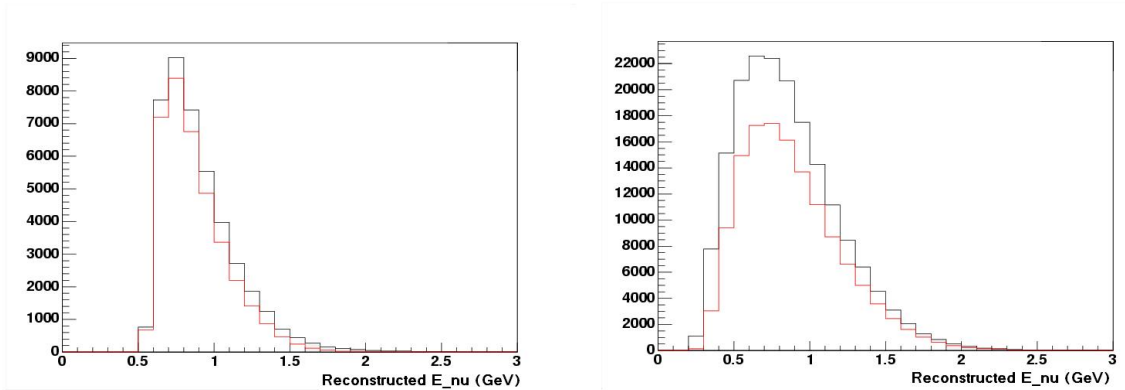


Figure 5.7: $CC\pi^+$ and $CCQE$ Boxes After Cuts vs. E_{rec} (GeV) (Monte Carlo). *Left: $CC\pi^+$; right: $CCQE$. Black: all events, red: Signal ($CC\pi^+$ or $CCQE$ respectively) only.*

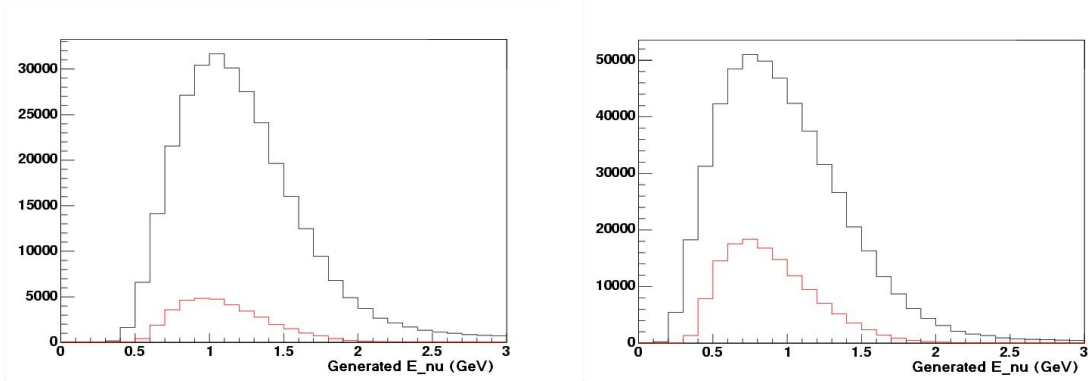


Figure 5.8: True $CC\pi^+$ and $CCQE$ events vs. E_{gen} (GeV) (Monte Carlo). *Left: $CC\pi^+$; right: $CCQE$. Black: before cuts, red: after cuts.*

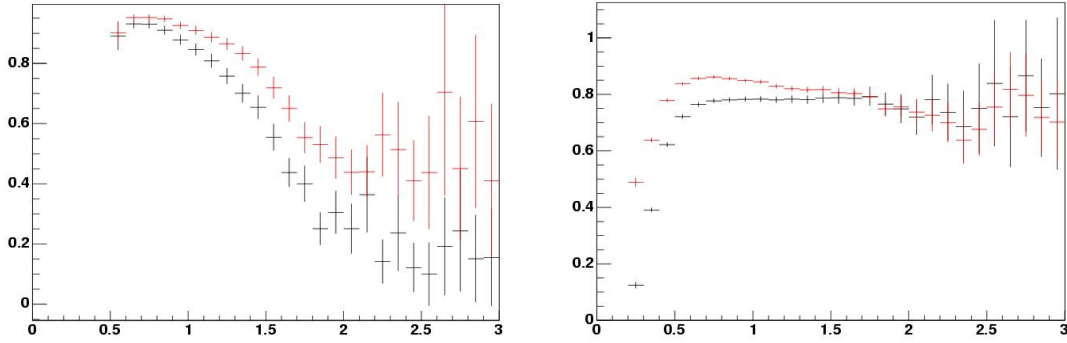


Figure 5.9: Effective (red) and FSI-corrected (black) signal fractions in $CC\pi^+$ (left) and $CCQE$ (right).

5.5 Neutrino Energy Unfolding

To correct or “unfold” reconstructed energy to true energy, we must find an operator U that acting on the reconstructed distribution N_{rec} returns the true distribution N_{true} . Typically, this will be constructed as a matrix U_{ij} such that $\sum_j U_{ij} * N_{rec,j} = N_{true,i}$. The standard way to construct U_{ij} consists of three steps:

1. Create a “migration matrix” A by binning Monte Carlo events in true and reconstructed energy; $A_{i,j}$ is the number of MC events in true energy bin i and reconstructed energy bin j .

2. Obtain a “smearing” matrix $S_{ji} = \frac{A_{ij}}{\sum_l A_{il}}$. This has the property that $\sum_i S_{ji} * N_{true,i} =$

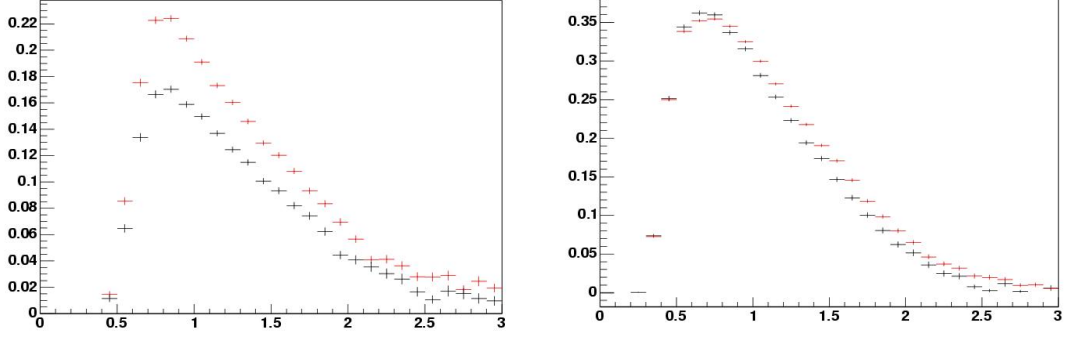


Figure 5.10: Effective (red) and FSI-corrected (black) cut efficiencies in $CC\pi^+$ (left) and $CCQE$ (right).

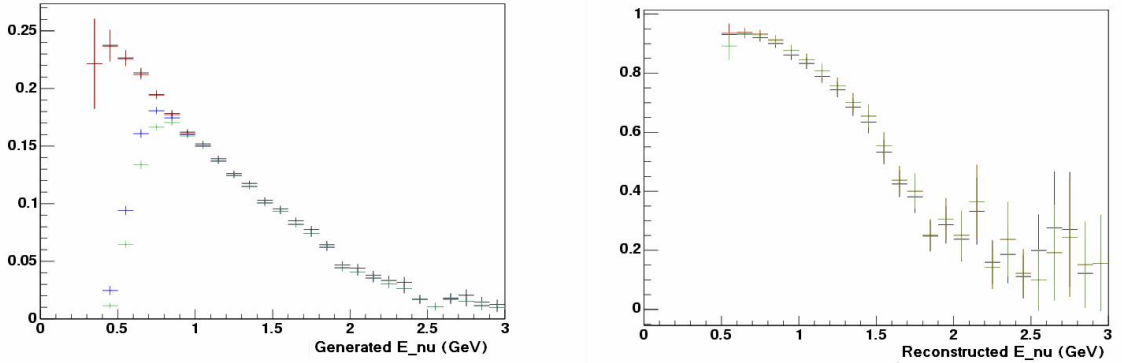


Figure 5.11: $CC\pi^+$ Cut Efficiency and Signal Fraction by Cut *Left: Cut Efficiency vs. E_{gen} (GeV); right: Signal Fraction vs. E_{rec} (GeV)*. Black: 3 sub-events and beam window cuts, red: $vcut$, blue: $tcut$, green: all cuts

$N_{rec,j}$.

3. Invert the smearing matrix to obtain an unfolding matrix $U = S^{-1}$. This has the desired property that $\sum_j U_{ij} * N_{rec,j} = N_{true,i}$

However, this method has certain notorious problems due to the numerical instability of matrix inversion. Specifically, the matrix inversion method tends to magnify small perturbations in the reconstructed distribution into very large variations in the unfolded distribution. Due to these fluctuations, results assigning negative numbers of events to certain bins frequently arise. To avoid these problems, we use an alternative, Bayesian method that does not require matrix inversion. Our method is equivalent to that proposed in [98], where further discussion can be found.

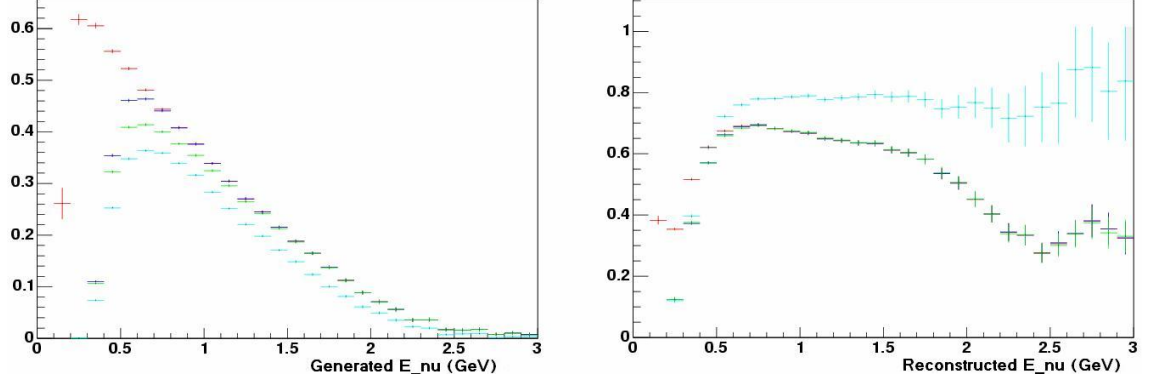


Figure 5.12: *CCQE* Cut Efficiency and Signal Fraction by Cut *Left: Cut Efficiency vs. E_{gen} (GeV); right: Signal Fraction vs. E_{rec} (GeV). Black: 2 sub-events and beam window cuts, red: v cut, dark blue: t cut, green: R cut, light blue: all cuts*

| Cut | Cut Efficiency | Signal Fraction |
|----------------------------|----------------|-----------------|
| 3 sub-events, beam window | 13.3% | 86.13% |
| vhits < 6 for all s.e. | 13.1% | 87.68% |
| thits > 175 for first s.e. | 12.3% | 87.12% |
| All cuts | 11.95% | 86.68% |

Table 5.3: $CC\pi^+$ Cut Efficiency and Signal Fraction by Cut

If there are $N_{rec,j}$ events in reconstructed energy bin j , the number N_{ij} of those events that we expect to come from true energy bin i can be written as:

$$N_{i,j} = P(i|j)N_{rec,j} \quad (5.12)$$

where $P(i|j)$ is the conditional probability for an event to be in true bin i , given that it is in reconstructed bin j . The total number of events expected to be in true energy bin i , $\hat{N}_{true,i}$, is the sum over j :

| Cut | Cut Efficiency | Signal Fraction |
|---------------------------|----------------|-----------------|
| 2 sub-events, beam window | 46.3% | 53.6% |
| vhits < 6 for all s.e. | 37.0% | 62.9% |
| thits cuts | 32.7% | 63.7% |
| R cut | 30.4% | 63.8% |
| All cuts | 26.3% | 73.9% |

Table 5.4: *CCQE* Cut Efficiency and Signal Fraction by Cut

$$\hat{N}_{true,i} = \sum_j N_{i,j} = \sum_j N_{rec,j} P(i|j) \quad (5.13)$$

The circumflex on the $\hat{N}_{true,i}$ is there to remind us that this is the *expected* number of events in bin i , not necessarily the *true* number.

The unfolding problem will now be solved if we can find a general expression for $P(i|j)$. For such an expression, we turn to Bayes's theorem for conditional probabilities:

$$P(i|j) = \frac{P(j|i)P(i)}{P(j)} \quad (5.14)$$

$P(i|j)$ is thus expressed in terms of the converse conditional probability and the total prior probabilities of i and j . $P(j)$ can be rewritten as a sum over i :

$$P(j) = \frac{P(j|i)P(i)}{\sum_i P(j|i)P(i)} \quad (5.15)$$

This expression can then be plugged into eq. 5.13:

$$\hat{N}_{true,i} = \sum_j \frac{P(j|i)P(i)}{\sum_l P(j|l)P(l)} N_{rec,j} \quad (5.16)$$

We now have an expression for the unfolding matrix in terms of the prior probabilities $P(i)$ and the conditional probabilities $P(j|i)$. Both of these can be obtained from the Monte Carlo, which represents our *a priori* best guess for the true energy distribution. Note that $P(j|i)P(i)$ is, up to a factor of the total number of Monte Carlo events, the migration matrix $A_{i,j}$. In terms of the migration matrix, then:

$$\hat{N}_{true,i} = \sum_j \frac{A_{i,j}}{\sum_l A_{l,j}} N_{rec,j} \quad (5.17)$$

To obtain an unfolding matrix, then, we first bin the MC events in reconstructed and true energy to form the migration matrix A ; then we calculate the unfolding matrix $U_{i,j} = \frac{A_{i,j}}{\sum_l A_{l,j}}$. This is in practice very similar to the matrix inversion method described

above, except that rather than normalizing each bin of *true* neutrino energy in the migration matrix to unity (which gives the smearing matrix S , which then needs to be inverted), we normalize each bin of *reconstructed* energy, directly obtaining the unfolding matrix U . The element U_{ij} can be thought of as representing the fraction of events in reconstructed bin j that are also in true bin i .

When N_{true} and N_{rec} are the MC distributions we have used to generate U_{ij} , it is trivially true that $N_{true,i} = \sum_j U_{ij} * N_{rec,j}$. However, in practice there will be a difference between the Monte Carlo and data distributions, so that while:

$$N_{unfolded,i}^{MC} \equiv \sum_j U_{ij} * N_{rec,j}^{MC} = N_{true,i}^{MC} \quad (5.18)$$

holds, the same is not exactly true of the data distributions:

$$N_{unsmearred,i}^{data} \equiv \sum_j U_{ij} * N_{rec,j}^{data} \neq N_{true,i}^{data} \quad (5.19)$$

Although we don't know *a priori* how large this difference will be, we can gauge its significance by comparing generated Monte Carlo with unfolded data (see figure 5.17).

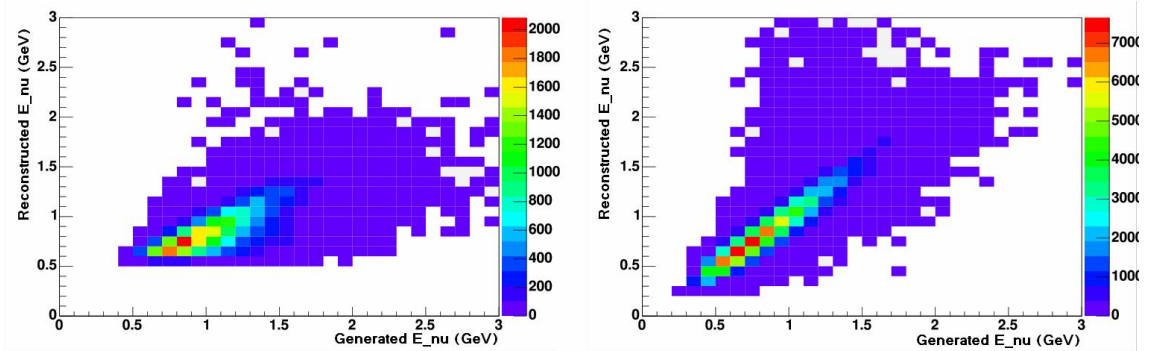


Figure 5.13: Reconstructed vs. True Neutrino Energy (GeV) (Monte Carlo) *Left: $CC\pi^+$; right: $CCQE$.*

To confirm that this unfolding method works, a simple closure test was performed. An unfolding matrix was constructed from a subset of the Monte Carlo and was then used to unfold a statistically independent Monte Carlo subset. The results, shown in figures 5.15

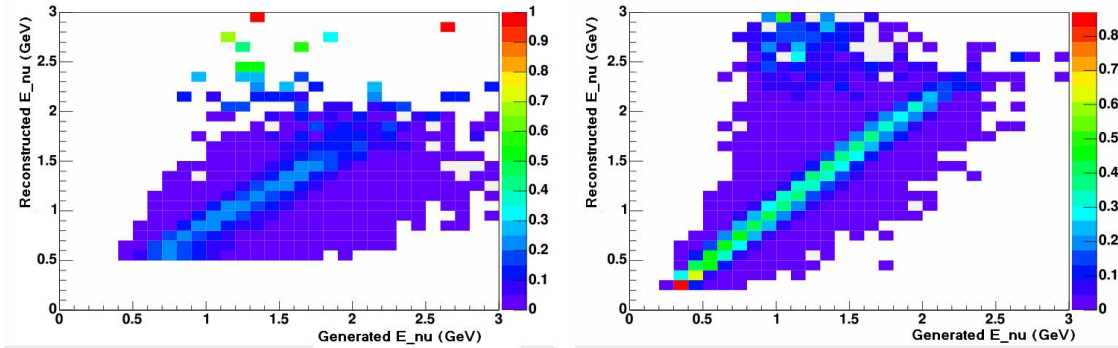


Figure 5.14: Unsmearing Matrices (GeV). *Left: $CC\pi^+$; right: $CCQE$.*

and 5.16, confirm the soundness of the method.

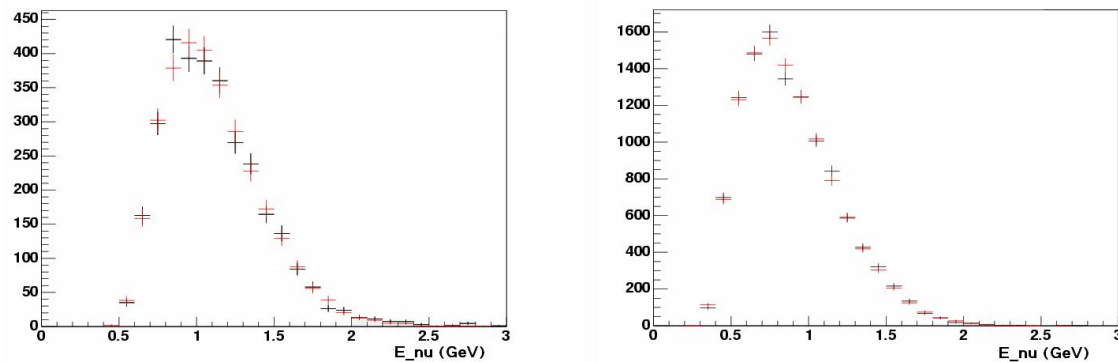


Figure 5.15: True vs. Unsmearred Distributions vs. ν Energy (GeV) (Monte Carlo) *Left: $CC\pi^+$, right: $CCQE$; black: true, red: unsmearred*

Because the unfolding matrix is dependent on the initial distributions in our MC, this method introduces a bias toward these initial distributions. This is to be expected, given that this method is essentially Bayes's theorem with those initial distributions as the prior probabilities. However, this additional dependence on MC introduces an additional source of systematic uncertainty into the measurement, which must be accounted for. This may be contrasted with the matrix inversion method, which is unbiased, because the initial MC distribution is normalized out of the smearing matrix. Because it is completely unbiased, the matrix inversion method has no compunction against giving wildly fluctuating, unphysical results. These results tend to be highly sensitive to the input reconstructed distribution, with the result that statistical uncertainties in the reconstructed distribu-

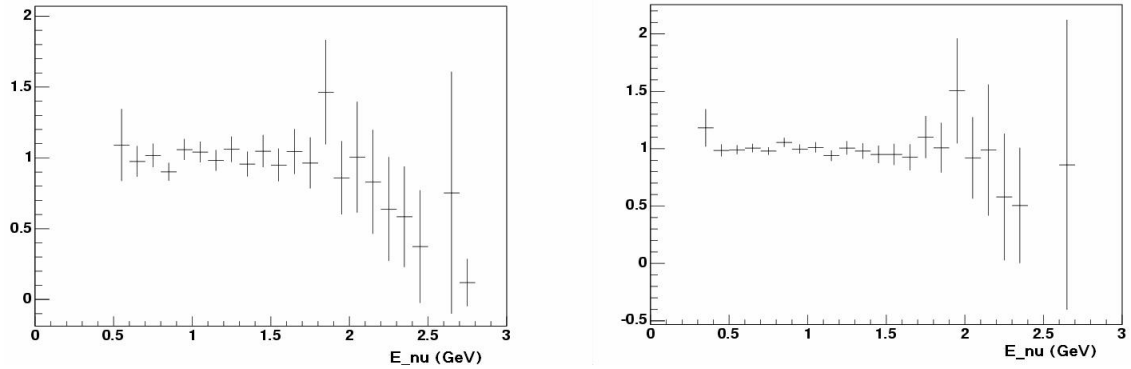


Figure 5.16: Unsmear/True Ratio vs. ν Energy (GeV) (Monte Carlo) *Left: $CC\pi^+$, right: $CCQE$*

tion are typically inflated by many orders of magnitude in the unfolded distribution. By choosing the Bayesian method over the matrix inversion method, we essentially trade huge statistical uncertainties for reasonable systematic uncertainties.

To gauge the significance of the bias introduced by the Monte Carlo, we can compare the unsmear data distributions with the $CC\pi^+$ and $CCQE$ distributions generated by the Monte Carlo. If there is a significant bias away from the “correct” data distribution, then we would expect to see significant disagreement between the unfolded data and the Monte Carlo. Figure 5.17 shows this comparison for both $CC\pi^+$ and $CCQE$; figure 5.18 gives the ratio of unfolded data to generated Monte Carlo. These plots confirm that there is no large data-MC discrepancy in either of these distributions.

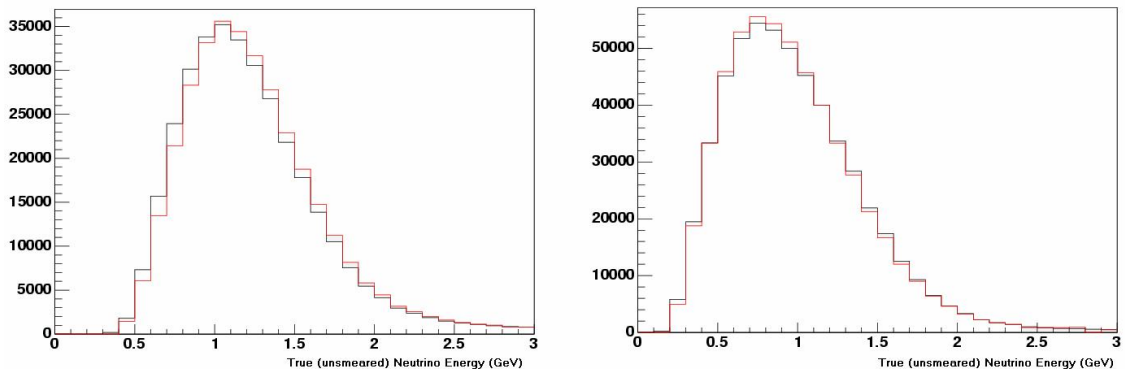


Figure 5.17: Corrected data (red) and Monte Carlo generated (black) distributions for $CC\pi^+$ (left) and $CCQE$ (right).

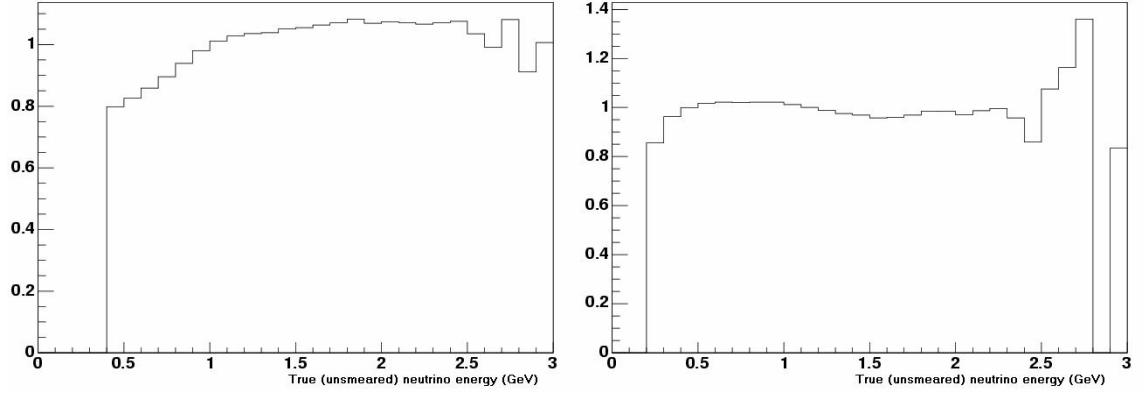


Figure 5.18: Ratio of corrected data to Monte Carlo generated distributions. Left: $CC\pi^+$, right: $CCQE$

If we were including uncertainties on the distributions of signal events in our calculation of systematic error, we would not need to worry any further about the bias; the parameter space covered by the MC variations would include the point that corresponds with reality, and the true unsmearred distribution would thus be within our error bars. However, because we do not include variations on certain parameters that affect only signal events (see section 5.6), we need to account for the bias in some other way. We do this by including an iteration of the unfolding process as a contribution to the systematic uncertainty; this also provides another check that nothing is going wrong in the unfolding process. To iterate, we reweight the Monte Carlo to match the corrected data, using the ratios shown in figure 5.18. From the reweighted Monte Carlo, we form new unfolding matrices for $CC\pi^+$ and $CCQE$ (as well as obtaining new purities and efficiencies) and apply these to the raw data to obtain new results for the corrected distributions.

The plot on the left in figure 5.19 compares the ratio after the initial analysis with the ratio after a single iteration. The plot on the right shows both of these as well as the ratio after a further iteration. Figure 5.20 shows the ratio of each of these iterated results to the initial result. The first iteration is included as a unisim variation (see section 5.6) in our uncertainties.

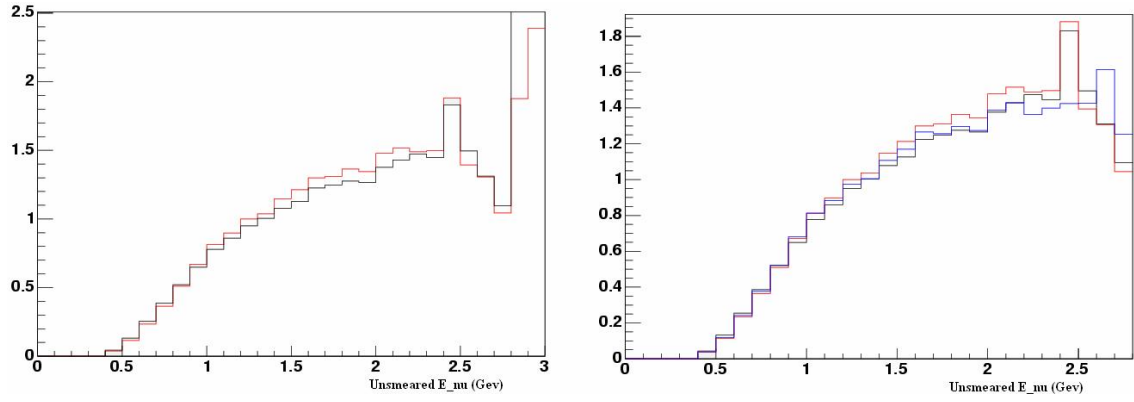


Figure 5.19: Ratio after zeroth (black), first (red), and second (blue) iterations.

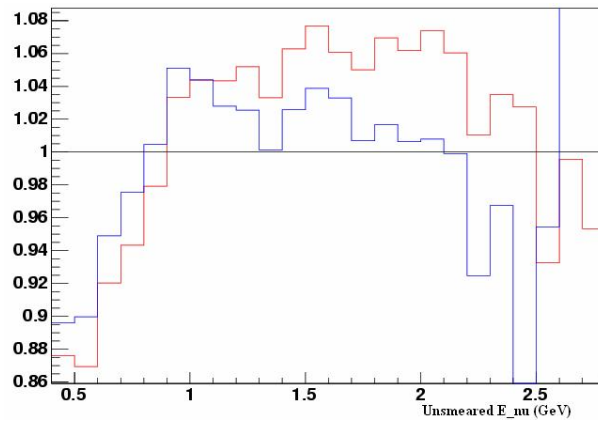


Figure 5.20: Ratio of ratios. Red: first iteration to zeroth iteration; blue: second iteration to zeroth iteration.

5.6 Systematic Uncertainties

As seen in the preceding sections, the results of the analysis depend on our detector simulation as well as flux and cross section predictions from Monte Carlo. These simulations depend on parameters that are not known exactly and thus have uncertainties associated with them; these uncertainties translate into systematic uncertainties on the results of the analysis. To evaluate the uncertainty on the measured $CC\pi^+$ to $CCQE$ ratio, we must therefore vary the parameters on which our simulations depend within their uncertainties.

If the central value of an underlying parameter i of the simulations is denoted α_i^{cv} and the uncertainty on its value is δ_i , then to test the dependence of our result on the uncertainty in that parameter, we can run a new simulation in which the value of parameter i is changed to $\alpha_i^u = \alpha_i^{cv} + \delta_i$ and all other parameters are unchanged. This simulation will, in general, produce altered predictions for all the quantities used in our analysis except for the values from the raw data itself. We can then repeat the analysis using the predictions from the new simulation in place of the central value predictions to obtain a new result. In MiniBooNE parlance, this technique, in which a single simulation parameter is varied, is called a “unisim” variation.

Many of the parameters on which the simulations depend, however, are correlated. Altering each parameter one by one in a series of unisims would fail to take these correlations into account. Therefore in these cases we use a “multisim” variation. In a multisim, the correlated parameters are varied within the region of parameter space allowed by their uncertainties. This ensures that correlations among the varied parameters are properly included in the final error matrices and also reduces the computational load compared with running a separate unisim for each parameter.

The unisims and multisims used in the cross section analysis are:

1. Meson production multisims: These four multisims vary meson production in the beryllium target. The four multisims are:

- π^+ production

- π^- production
- K^+ production
- K^0 production

2. Beam unisims: Variations in a group of uncorrelated parameters relating to the horn and to interactions in the beryllium target. The parameters are:

- nuclear inelastic cross section
- nuclear quasi-elastic cross section
- pion inelastic cross section
- pion quasi-elastic cross section
- pion total cross section
- skin depth (penetration of horn current inside the conductor, creating a magnetic field in the inner conductor)
- horn current

3. Cross section multisim: Variations in the neutrino interaction cross sections.

4. π^0 yield multisim: Variations in the production of π^0 s in neutrino interactions in the detector.

5. Tank re-interaction multisim: Variations in the model for hadronic re-interactions in the Geant3 detector simulation.

6. Nuclear re-interaction multisim: Variations in the model for hadronic re-interactions in the target nucleus used by NUANCE (included only for FSI-corrected measurement).

7. Optical model multisim: Variations in the 39 parameters of the model used to simulate light propagation in the mineral oil and PMT response.

8. Unfolding iteration unisim: Variation to account for uncertainty due to the bias introduced by our neutrino energy unfolding method (see section 5.5).

9. Event selection unisim: Variation in $CC\pi^+$ selection cuts (see section 5.7.1).
10. Event reconstruction unisim: Variation using an alternative event reconstruction scheme (see section 5.7.2).
11. Q^2 reweighting unisim: Variation with $CC\pi^+$ events reweighted to enforce agreement with MC in Q^2 (see section 5.7.3).
12. π^+ momentum distribution unisim: Variation in the momentum distribution of π^+ s produced in $CC\pi^+$ events (see section 5.7.4).

These uncertainties were divided into three groups which were calculated separately: uncertainties associated with the flux, neutrino cross sections, and hadronic re-interactions in the tank (numbers 1-5 above); those associated with the optical model and re-interactions in the target nucleus (6 and 7); and those from miscellaneous additional sources (8-12). More detailed information on the uncertainties assigned to each parameter can be found in [66] (for flux-related uncertainties), [67] (for optical model uncertainties), and [85] (for neutrino cross-section and hadronic re-interaction uncertainties).

In the error propagation analysis we calculate each variable which appears in the ratio measurement equation for each multisim or unisim excursion. In particular, it is to be noted that we calculate the unfolding matrix separately for each excursion and use it to unfold the neutrino energy for the data corrected for background from the same excursion.

The error matrix elements for the set of multisims for a given error source are obtained using the following formula:

$$M_{ij}(x) = \frac{1}{s-1} \sum_{k=1}^s \left(x_i^k - x_i^{cv} \right) \left(x_j^k - x_j^{cv} \right) \quad (5.20)$$

where x_j^k denotes the value of variable x in the k th multisim in i th bin, and x_i^{cv} is the value of the variable x in the i th bin for the central value (CV) Monte Carlo. The total error

matrix is a sum of contributions from all error sources:

$$\begin{aligned}
M_{ij} &= M_{ij} (\pi^+ \text{ production}) + M_{ij} (\pi^- \text{ production}) + M_{ij} (K^+ \text{ production}) \\
&+ M_{ij} (K^0 \text{ production}) + M_{ij} (\text{beam unisim}) + M_{ij} (\text{cross section}) \\
&+ M_{ij} (\pi^0 \text{ yield}) + M_{ij} (\text{optical model}) \\
&+ M_{ij} (\text{data statistics}) + M_{ij} (\text{MC statistics})
\end{aligned} \tag{5.21}$$

The total error for a i-th bin is

$$\Delta x_i^{total} = \sqrt{M_{ii}} \tag{5.22}$$

In most MiniBooNE analyses the distribution for which the error matrix is calculated has a form such that it can be fit with a smooth and decreasing function. In such a case we can sum over all error matrix elements to obtain the normalization error. However, the $CC\pi^+$ to $CCQE$ ratio has different behavior - it is an increasing function up to 2.5 GeV neutrino energy but this does not represent an increase in the number of events. At neutrino energies greater than 2.5 GeV there are several spikes typical for the case of division by a number close to zero.

Taking into account the behavior of the ratio distribution, we used bins only up to 2.4 GeV in both the optical model and flux/cross section uncertainties. The statistical errors are taken into account by using Monte Carlo samples with the same number of events as in the data.

5.6.1 Cross section and flux uncertainties

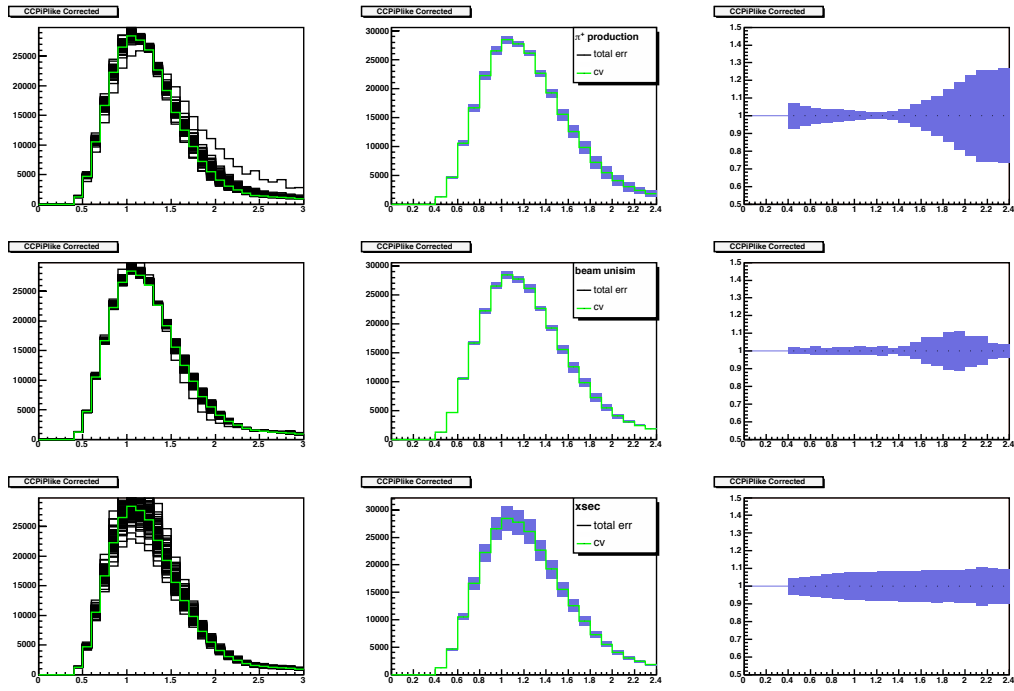
Cross section and flux uncertainties are, in accordance with standard MiniBooNE practice, calculated together by a single software package; the individual contributions of each of the unisims and multisims can, however, be extracted by the package. In both samples for the $CC\pi^+$ to $CCQE$ ratio analysis, we distinguish a signal and background. To avoid double counting we propagate errors for each sample separately up to the calculation of the

ratio itself. For the cross section uncertainties, most of the errors are only applied to the background of each respective sample. Thus, in each respective sample, we omit from the calculation uncertainties associated with the cross section of that sample's signal events, which is in essence what is being measured. The nuclear model parameters, p_F and E_B are applied to both samples because they can change the total number of events. Also, CCQE normalization errors were applied to the $CCQE$ sample to take into account the 10% cross section normalization uncertainty. In the cross section error matrix, two parameters are not connected with the neutrino interaction, but with the pion propagation in the tank, pion absorption and pion charge exchange. Again, these are included here, instead of with the detector simulation where they would more logically belong, for technical reasons relating to the MiniBooNE analysis software. In table 5.5 the set of uncertainties applied is shown. In calculating the error matrix for the $CC\pi^+$ to $CCQE$ ratio we reprocessed each sample separately with different sets of parameters in the cross section multisims. For each sample, 1000 files, corresponding to $5.48E20$ POT, were reprocessed with 100 draws.

| Error | $CC\pi^+$ | $CCQE$ |
|------------------|-----------|--------|
| $p_F(ccpip)$ | yes | yes |
| $p_F(ccqe)$ | yes | yes |
| $p_F(other)$ | yes | yes |
| $E_B(ccpip)$ | yes | yes |
| $E_B(ccqe)$ | yes | yes |
| $E_B(other)$ | yes | yes |
| M_A^{QE} | yes | no |
| $M_A^{1\pi}$ | no | yes |
| κ | yes | no |
| CCQE Norm | yes | no |
| M_A^{coh} | no | yes |
| pi Abs (in tank) | yes | yes |
| pi cex (in tank) | yes | yes |

Table 5.5: The set of errors used in the cross section errors analysis.

Contributions to the flux uncertainties come in two main forms. First, there are uncertainties in the production cross-sections in the p-Be interactions that generate the secondary (meson) beam. These are constrained by data from other experiments, as discussed



$\epsilon^{-1}\bar{U}(f * N^{data})$ - corrected data (CC π^+ -like)

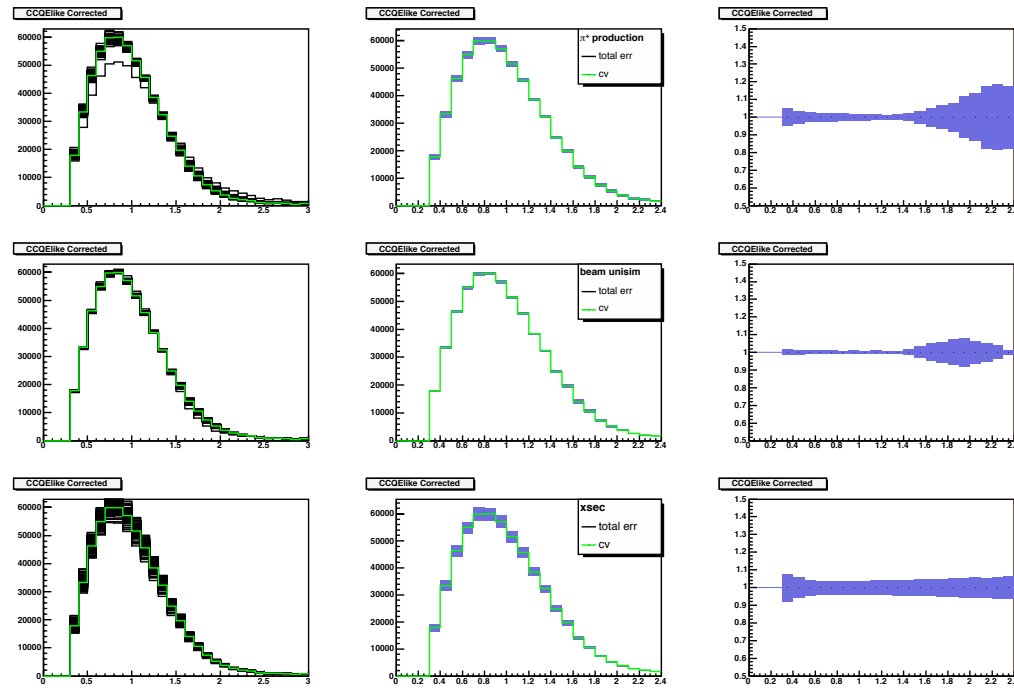


Figure 5.21: $\epsilon^{-1}\bar{U}(f * N^{data})$ - corrected data (CCQE-like)

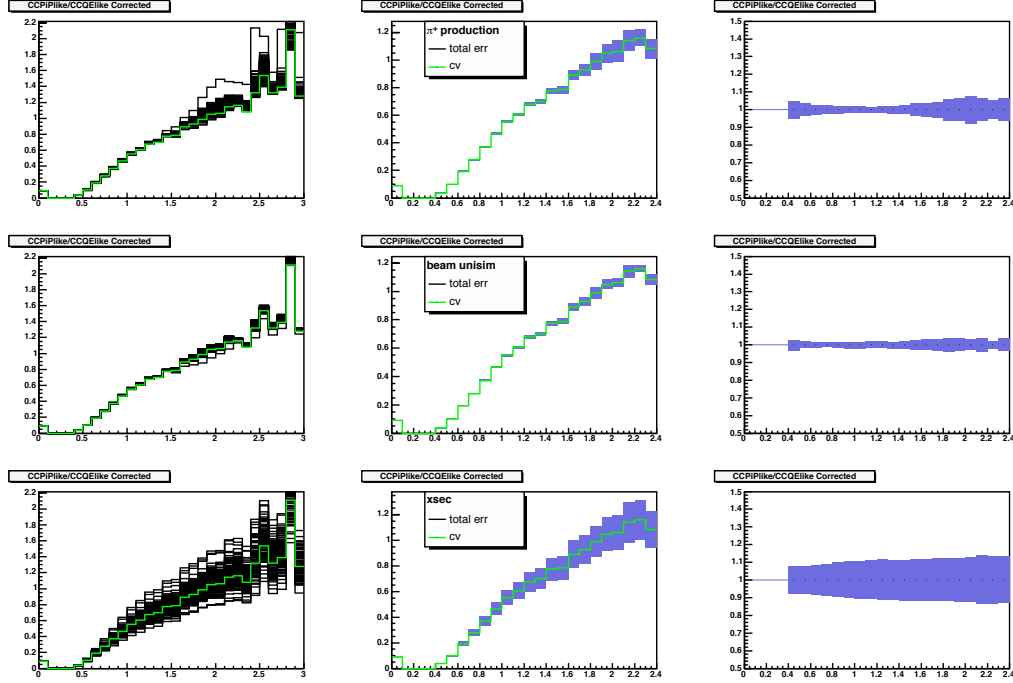
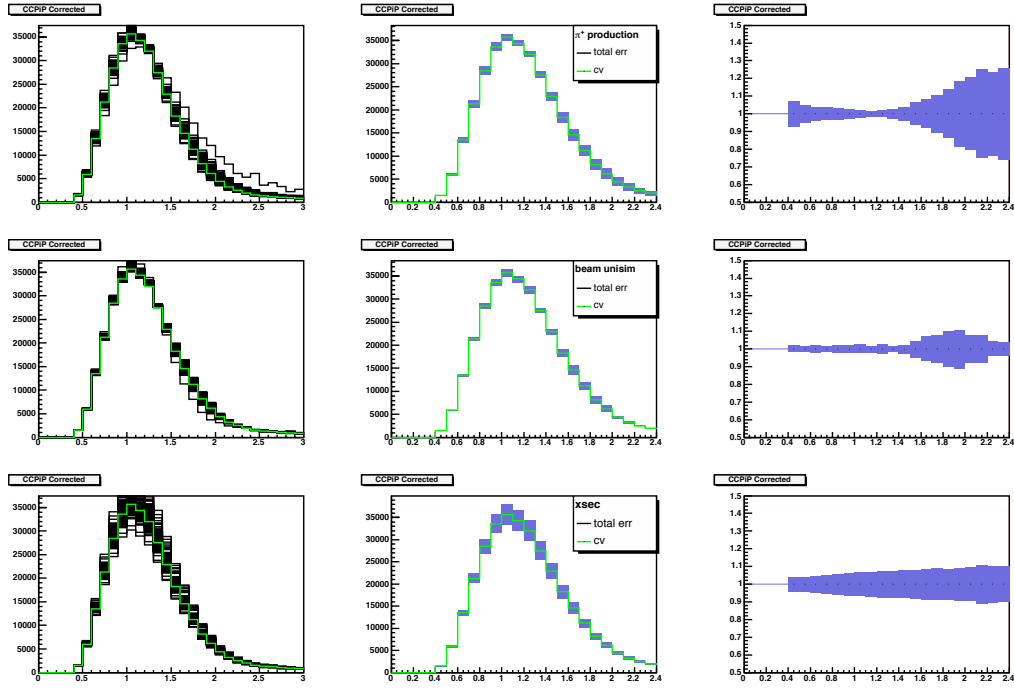


Figure 5.22: Observed cross section ratio for three sources of errors.

in section 3.1. Second, there are several uncorrelated variations that collectively constitute the “beam unisims”. These include hadronic interactions in the beryllium and aluminum, the roughly 0.5% uncertainty in the horn current, and uncertainty on the skin depth of the horn’s inner conductor. Uncertainties in the geometry of the beamline simulation are not included, as it was found that variations within the construction tolerances have a negligible effect on the neutrino flux prediction. The contributions to the total flux uncertainty for each neutrino species are shown in table 5.6. Note that these are just the total sizes of the uncertainties; in the actual calculation of systematic uncertainties for the analysis, the appropriate uncertainty for each energy bin is used.

In the flux and cross-section error analysis for $CC\pi^+$ to $CCQE$ ratio we observed that only three sources of uncertainty are significant: π^+ production, the beam unisims, and the cross-sections. Note that the latter includes both the principal background processes for each sample ($CC\pi^+$ in the $CCQE$ sample and $CCQE$ and multi-pion in the $CC\pi^+$ sample) and the cross-sections for hadronic re-interactions in the mineral oil. In figure



$CC\pi^+$: $\epsilon^{-1}\bar{U}(f * N^{data})$ - corrected data, FSI-corrected

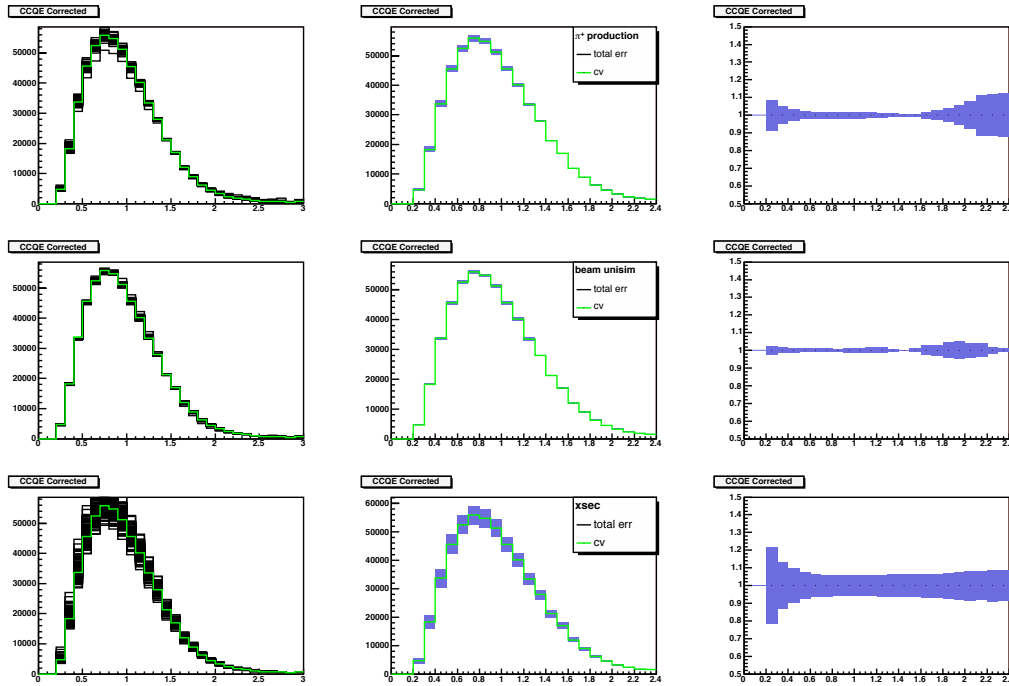


Figure 5.23: $CCQE$: $\epsilon^{-1}\bar{U}(f * N^{data})$ - corrected data, FSI-corrected

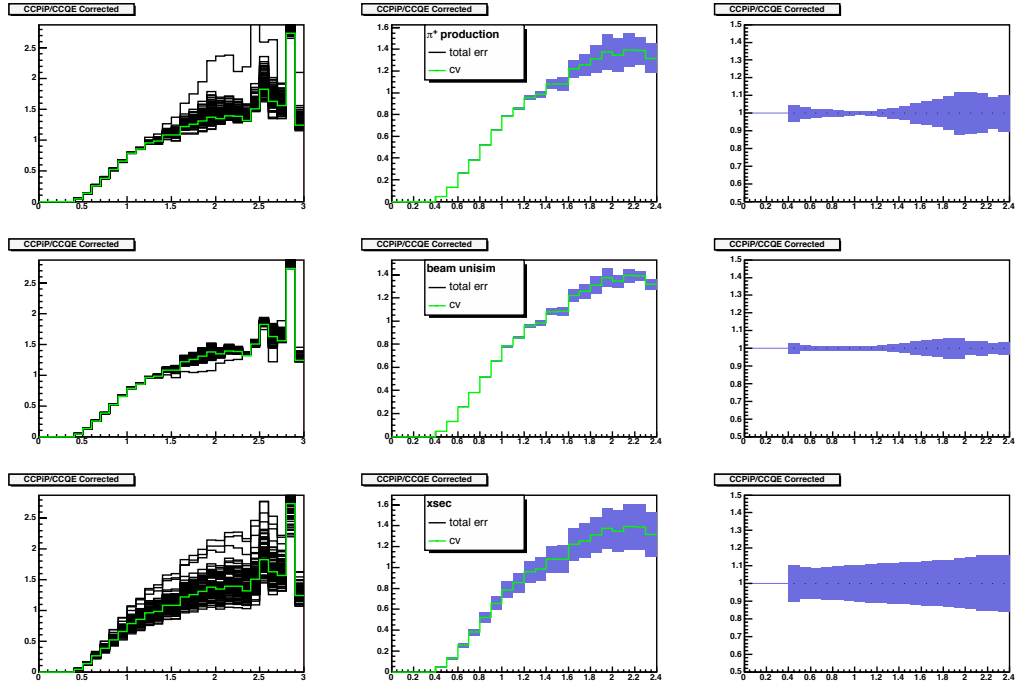


Figure 5.24: $CC\pi^+$ to $CCQE$ ratio for three sources of errors.

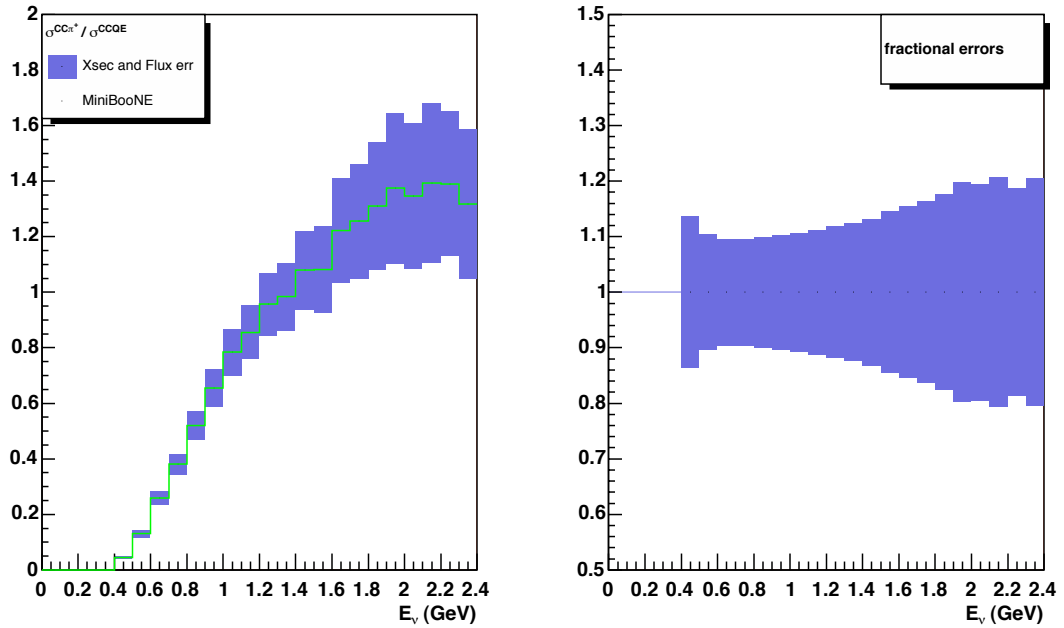


Figure 5.25: The $CC\pi^+$ to $CCQE$ ratio with cross section and flux uncertainties. Cross section errors are included only in the background for each sample; uncertainties on the nuclear parameters and on pion propagation are included in both signal and background.

| Source of Uncertainty | ν_μ | $\bar{\nu}_\mu$ | ν_e | $\bar{\nu}_e$ |
|------------------------|-----------|-----------------|---------|---------------|
| Proton delivery | 2.0% | 2.0% | 2.0% | 2.0% |
| Proton optics | 1.0% | 1.0% | 1.0% | 1.0% |
| π^+ production | 14.7% | 1.0% | 9.3% | 0.9% |
| π^- production | 0.0% | 16.5% | 0.0% | 3.5% |
| K^+ production | 0.9% | 0.2% | 11.5% | 0.3% |
| K^0 production | 0.0% | 0.2% | 2.1% | 17.6% |
| Horn field | 2.2% | 3.3% | 0.6% | 0.8% |
| Nucleon cross-sections | 2.8% | 5.7% | 3.3% | 5.6% |
| Pion cross-sections | 1.2% | 1.2% | 0.8% | 0.7% |

Table 5.6: Variations in the total flux prediction for each neutrino species in neutrino mode for each of the sources of systematic uncertainty.

5.21 the corrected $CC\pi^+$ -like and $CCQE$ -like event distributions for the observed cross section measurement are shown separately for each of these three sources of error. The left column shows all multisim excursions; the central column shows the CV results with errors calculated according to eqs. 5.21 and 5.22; and the right column shows the fractional error. The uncertainties on the observed $CC\pi^+$ to $CCQE$ ratio are similarly presented in figure 5.22. The biggest errors come from the cross section uncertainties and the flux errors mostly cancel out as expected.

Figures 5.23 and 5.24 show the corrected data distributions and cross section ratio with the same three sources of error for the FSI-corrected measurement. Figure 5.25 shows the observed $CC\pi^+$ to $CCQE$ cross section ratio with all flux and cross section uncertainties.

5.6.2 Optical model uncertainties

The MiniBooNE optical model is discussed in chapter 3.

The optical model multisims are variations of the Monte Carlo in which the 39 parameters of the optical model have been varied within their uncertainties. These parameters are correlated, necessitating a multisim rather than a unisim treatment. The covariance matrix relating the variations among these parameters was built through an iterative process. An initial guess at a covariance matrix was made, based on measurements of the 39 parameters. From this initial matrix, 3000 draws were made, giving 3000 parameter

sets consistent to within uncertainties with the measured values of the parameters. For each parameter set, a data to MC comparison was made of electrons from muon decay in cosmic ray events, and a χ^2 was obtained using statistical error only. Each of the 3000 parameter sets was then assigned a weight based on this χ^2 . A new covariance matrix was then formed by taking the weighted average 3000 draws. The procedure was repeated until agreement between the data and MC ceased to improve. Eighty parameter sets were drawn from the final covariance matrix and the full Monte Carlo was run with each set. As with the cross-section and flux multisims, the ratio analysis was repeated in its entirety for each Monte Carlo variation.

Uncertainties in pion absorption and charge exchange within the target nucleus, which are only included in the error analysis for the FSI-corrected measurement, are handled together with the optical model variations. These variations are achieved by reweighting Monte Carlo events in which absorption or charge exchange occurred. The variations used are 35% for pion absorption and 50% for pion charge exchange.

Figures 5.26 and 5.27 show the corrected data for the observed ratio measurement with optical model errors. Figure 5.28 shows the observed cross section ratio with optical model errors only. Figures 5.29 through 5.31 show the corresponding plots for the FSI-corrected ratio.

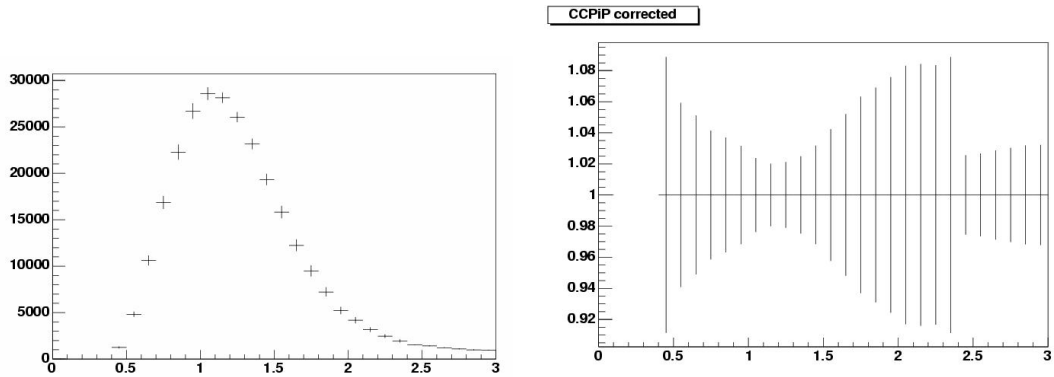


Figure 5.26: $CC\pi^+$: $\epsilon^{-1}\bar{U}(f * N^{data})$ - corrected data; effective

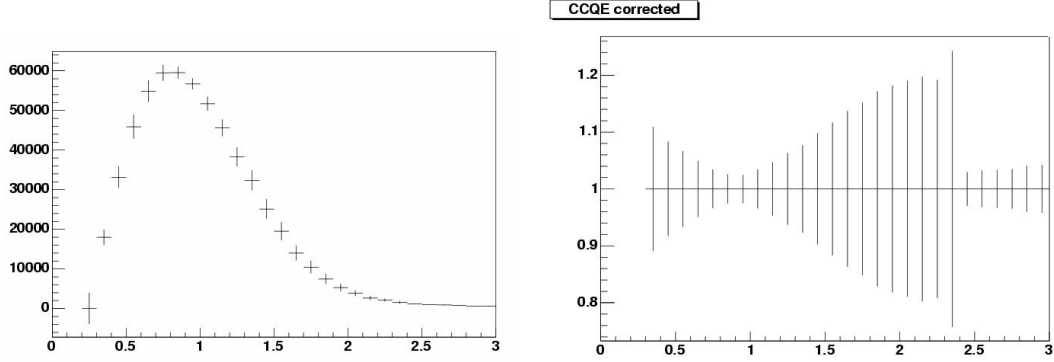


Figure 5.27: $CCQE: \epsilon^{-1}\bar{U} (f * N^{data})$ - corrected data; effective

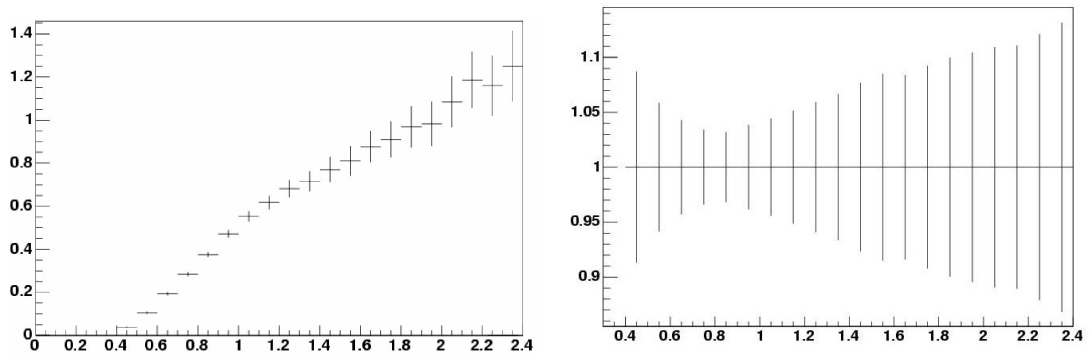


Figure 5.28: Observed ratio with OM errors

5.6.3 Additional unisims

Five further unisim variations were performed to assess sources of uncertainty more specific to the ratio analysis. These were variations in the energy unfolding, the event selection, the muon energy reconstruction, the Q^2 distribution for $CC1\pi^+$, and the pion momentum distribution for $CC1\pi^+$. The energy unfolding variation was discussed in section 5.5; the other four unisims will be discussed in section 5.7. None of these unisims gave an error of more than about 3% in the high-statistics region around 1 GeV.

5.6.4 Total Uncertainties

The errors from cross-section and flux, the optical model, the additional unisims, and statistics are added in quadrature in each energy bin to obtain the total uncertainties. In the region with highest statistics, around 1 GeV in neutrino energy, there is roughly an

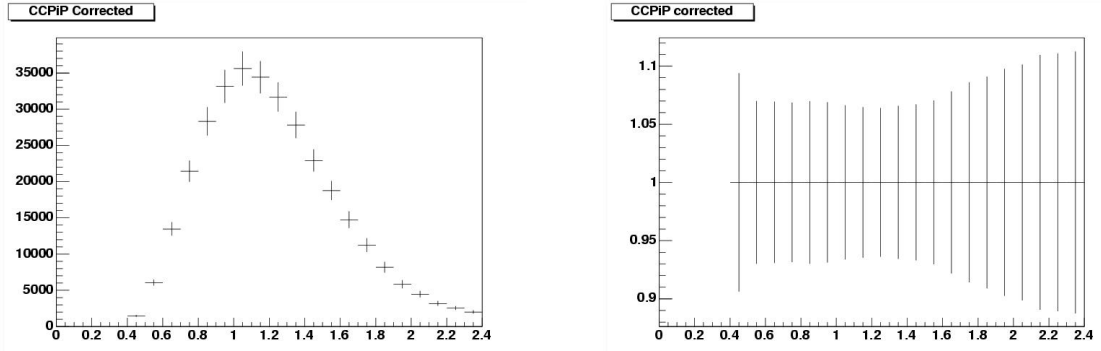


Figure 5.29: $CC\pi^+$: $\epsilon^{-1}\bar{U}(f * N^{data})$ - corrected data, FSI-corrected

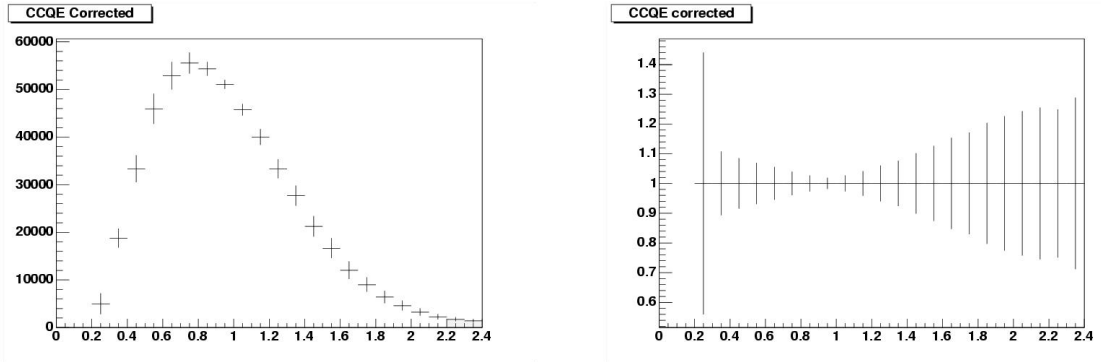


Figure 5.30: $CCQE$: $\epsilon^{-1}\bar{U}(f * N^{data})$ - corrected data, FSI-corrected

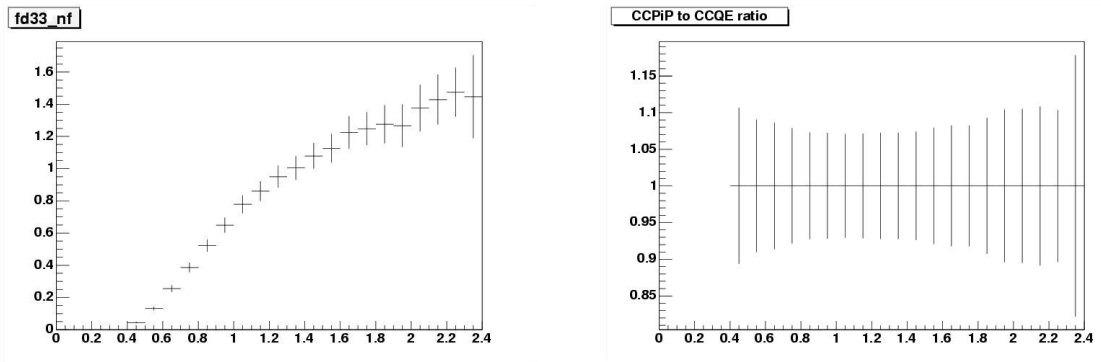


Figure 5.31: Left: FSI-corrected $CC\pi^+$ to $CCQE$ ratio with optical model uncertainties only. Right: Fractional errors on ratio from optical model multisims.

8% fractional error due to hadron re-scattering in the oil, 6% from neutrino cross-sections, 4% from the detector simulation, 2% from the neutrino flux prediction, and 2% from the statistics of the two samples. In the FSI-corrected measurement, uncertainties on hadronic re-interactions within the struck nucleus contribute an additional error of about 6%. Added in quadrature, these give a total uncertainty of about 11% for the observed ratio and 13% for the FSI-corrected ratio at 1 GeV.

5.7 Cross-checks

Several checks were performed to confirm the soundness of the ratio analysis, to test the sensitivity of the result to the methodology used, and to identify and account for possible sources of systematic uncertainty not included in the standard MiniBooNE error analysis.

5.7.1 Alternative Cuts

The cuts used for the main analysis (see section 5.3) were chosen to optimize signal fraction and cut efficiency for each sample. The choice of cuts for each sample was made independently. The selection cuts chosen include different requirements on the distance of the Michel electrons from the end of the muon track and on the number of signal region hits for the $CCQE$ and $CC\pi^+$ samples. In principle, there is nothing wrong with this; regardless of what cuts are used, as long as they are applied correctly to both data and Monte Carlo, we will obtain the proper cut efficiencies, signal fractions, and unfolding matrices for each sample. However, as a check that this is true, as well as a test of the sensitivity of our result to the particular cuts chosen, the analysis was re-performed using an alternative set of $CC\pi^+$ selection cuts. The alternative cuts are the same as those for the main analysis, except that the Michel distance cut and the tank hits cut have been changed to be the same as those for the $CCQE$ sample. The alternative $CC\pi^+$ cuts are thus:

1. Exactly three sub-events

2. First sub-event in beam window ($4400 < \text{SplitEvent_aveTTim} < 6400$)
3. Veto region hits < 6 for all sub-events
4. Signal region hits > 200 for first sub-event
5. Signal region hits < 200 for subsequent sub-events
6. $r_{\text{nu}} < 500$ cm., $r_{\text{mi1}} < 500$ cm., $r_{\text{mi2}} < 500$ cm, where r_{nu} is the distance of the interaction vertex from the center of the tank and r_{mi1} and r_{mi2} are the distances of the two Michel electrons from the center of the tank.
7. Distance from closest Michel electron to end of muon track < 100 cm.

The cut efficiency and signal fraction using the alternative cuts (figure 5.32) are slightly worse than with the standard cuts. This is to be expected, as the standard cuts were tuned to maximize the overall cut efficiency and signal fraction. Figure 5.33 compares the $CC\pi^+$ to $CCQE$ ratio using the two sets of cuts. There is no significant difference between the results, indicating that the differences in cuts between $CCQE$ and $CC\pi^+$ do not pose a problem. This also indicates that the result is not highly sensitive to our choice of cuts. The modified cuts analysis is included as a unisim variation (see section 5.6) in our errors.

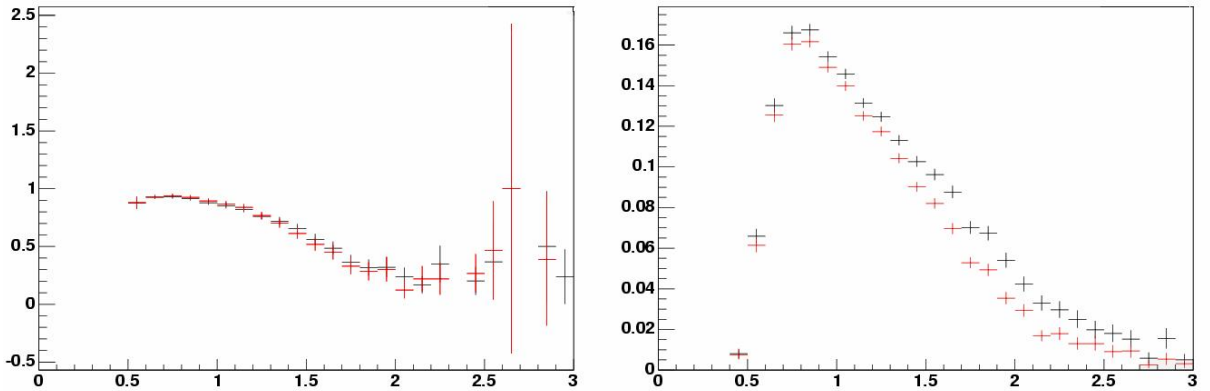


Figure 5.32: Signal fraction (left) and cut efficiency (right) for $CC\pi^+$ using standard (black) and alternative (red) cuts.

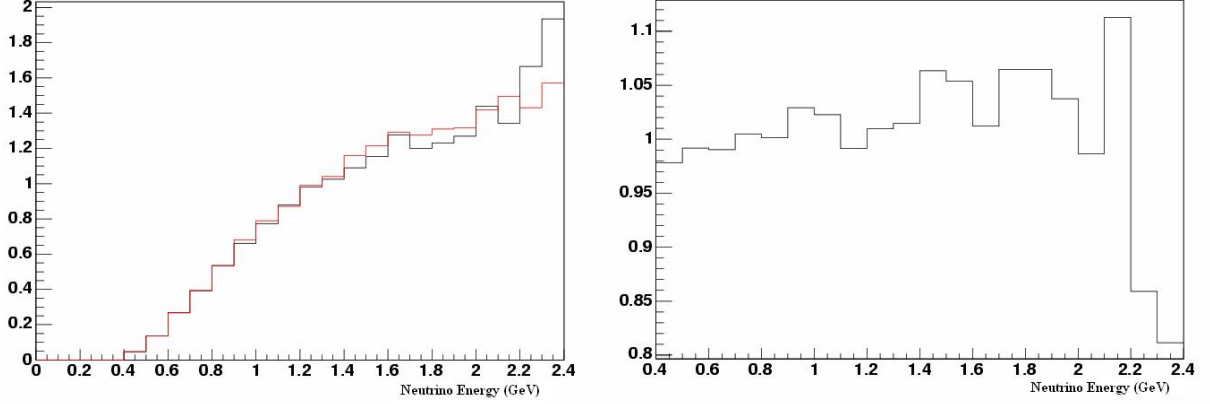


Figure 5.33: Left: $CC\pi^+$ to $CCQE$ ratio with standard (black) and modified (red) cuts. Right: Ratio of ratios; modified cuts/CV

5.7.2 Alternative Energy Reconstructions

The $CC\pi^+$ reconstruction used for the main analysis uses the StancuFlux fit for muon energy (see section 4.2 for a discussion of these fitters). However, the $CCQE$ reconstruction uses the muon energy from the StancuFull fit. The reconstructed neutrino energies for $CC\pi^+$ and $CCQE$, which are dependent on muon energy, are thus not directly comparable. In principle, this is not a problem, because in both event samples an unfolding correction is applied to transform reconstructed neutrino energy to true neutrino energy. However, as a check to make sure that this difference in reconstruction between the two samples does not have an effect on the ratio, we have repeated the ratio analysis with a subset of the Monte Carlo, using the muon energy from the StancuFull fit for $CC\pi^+$ as well as $CCQE$. We used the FSI-corrected ratio for this comparison. Because the FSI corrections apply the same way to both the principal ratio and the ratio using alternative reconstruction, it is sufficient to look only at the FSI-corrected ratio; agreement of the two versions of reconstruction in the FSI-corrected ratio implies agreement in the observed ratio.

Figure 5.34 shows, for both StancuFull and StancuFlux reconstruction, the Monte Carlo and data distributions in reconstructed neutrino energy of events passing $CC\pi^+$ cuts. There is a significant difference between the shapes of the distributions; that using StancuFull is broader and peaked higher than that using StancuFlux.

The signal fraction and cut efficiency for $CC\pi^+$ events in the two reconstructions are compared in figure 5.35. While the efficiency remains more or less the same, the signal fraction appears to improve dramatically with the StancuFull reconstruction. However, the improvement in signal fraction above about 1 GeV comes primarily from the fact that events in the lowest few bins in the StancuFlux reconstruction (which have high purity) are shifted into higher bins in the StancuFull reconstruction. This is illustrated in figure 5.36, which plots the reconstructed neutrino energy using StancuFull against that using StancuFlux for events in the $CC\pi^+$ sample. The total signal fraction with StancuFull reconstruction is about 90%, as compared to about 87% for StancuFlux.

Figure 5.37 shows the $CC\pi^+$ unsmearing matrices for StancuFlux and StancuFull. The unsmearing matrix for StancuFull is mostly diagonal. The unsmearred distributions and the ratio for the two reconstructions are compared in figure 5.38. The unsmearing procedure corrects both reconstructed distributions to nearly the same $E_{\nu,true}$ distribution and the result for the ratio is consistent. The ratio result obtained using StancuFull reconstruction is included as a variation in calculating our systematic uncertainties.

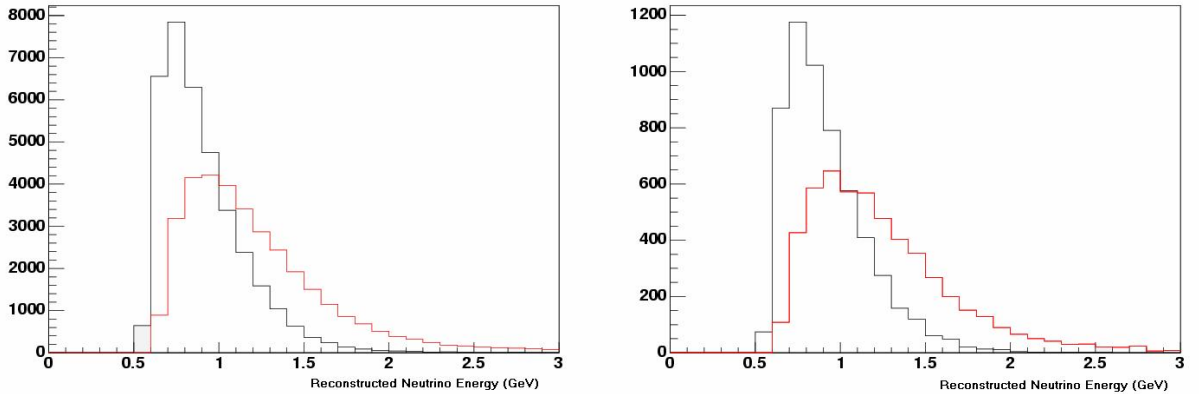


Figure 5.34: $CC\pi^+$ sample after cuts vs. reconstructed neutrino energy for Monte Carlo (left) and data (right). Black: StancuFlux reconstruction; red: StancuFull reconstruction.

A second check of the sensitivity of the result to our energy construction was performed by repeating the ratio analysis using the P-Fitter rather than the S-Fitter (see sections 4.2 and 4.3) and comparing it with the principal analysis. Before showing the results of this

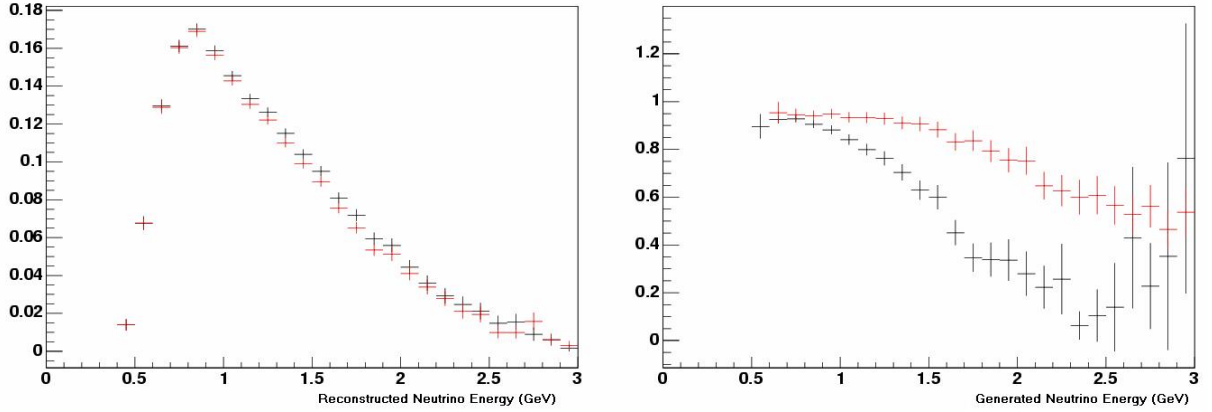


Figure 5.35: Cut efficiency (left) and signal fraction (right) for $CC\pi^+$ sample. Black: StancuFlux reconstruction; red: StancuFull reconstruction.

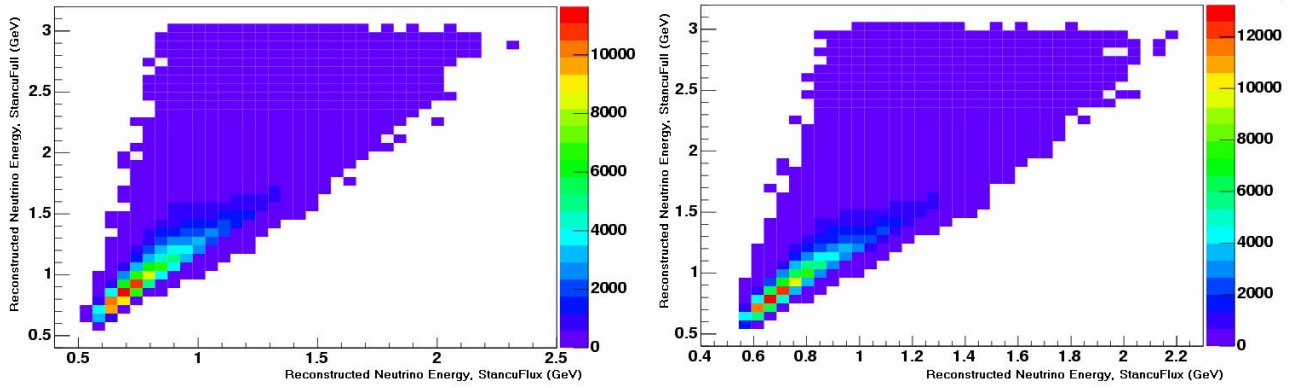


Figure 5.36: $E_{\nu,full}$ vs. $E_{\nu,flux}$ for all Monte Carlo events passing $CC\pi^+$ cuts (left) and for $CC\pi^+$ events only (right).

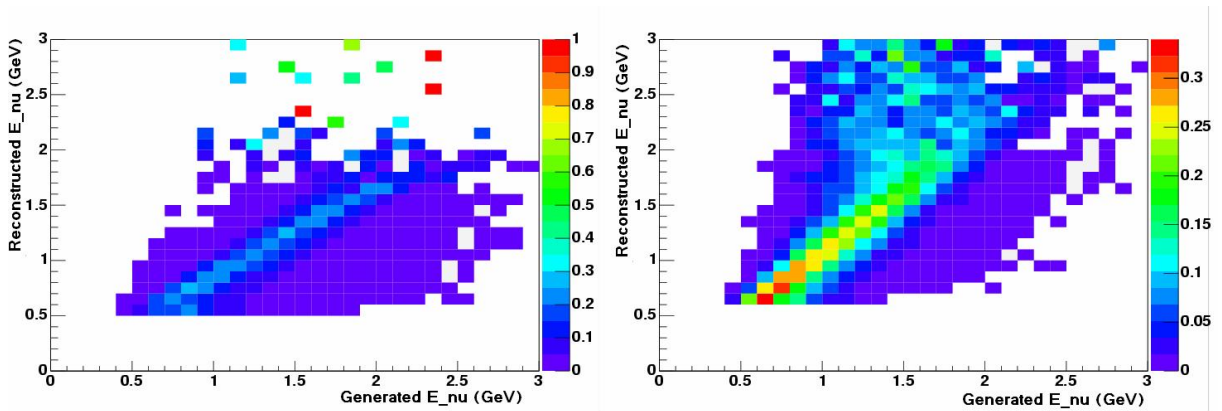


Figure 5.37: Unsmearing matrices for $CC\pi^+$ with StancuFlux reconstruction (left) and StancuFull reconstruction (right)

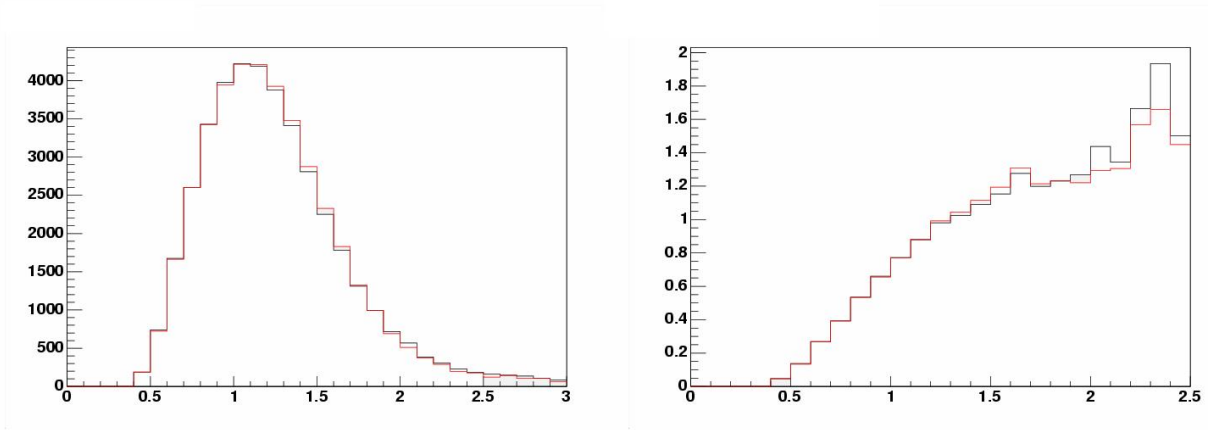


Figure 5.38: Unsmeared $CC\pi^+$ data (left) and $CC\pi^+$ to $CCQE$ ratio (right) vs. $E_{\nu,true}$. Black: StancuFlux reconstruction; red: StancuFull reconstruction.

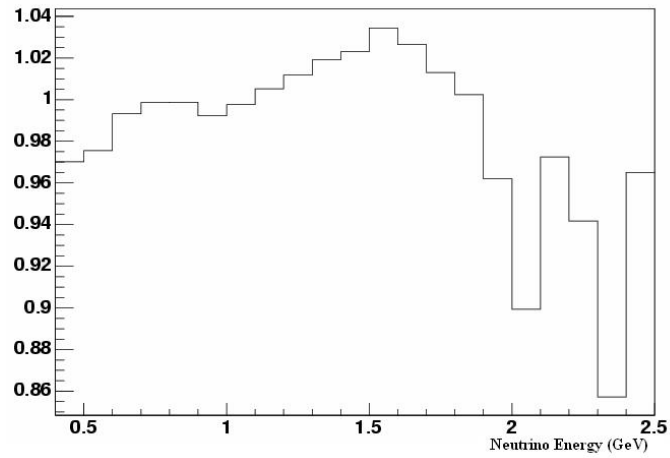


Figure 5.39: Ratio of corrected $CC\pi^+$ data using StancuFull reconstruction to the same using StancuFlux reconstruction.

check, we will compare the behavior of several variables used in event reconstruction with the two fitters.

Figures 5.40 and 5.41 compare the P-Fitter and S-Fitter (StancuFull) reconstructions for the event vertex. For each variable the plot on the left shows the data distributions, as reconstructed with the P-Fitter (the points with error bars) and the S-Fitter (the blue curve). The plot on the right shows the resolution (MC - data) in these variables. The radial (R) distribution requires some explanation. In the case of the P-Fitter analysis the event vertex is simply the origin of the muon track, while in the principal analysis it is given by the 4-vertex fit of the Stancu reconstruction. The S-Fitter has a tendency to pull events near the edge of the detector inward, resulting in the distinctive shape seen in the radial distribution. This in turn affects the vertex coordinates, as is best seen in the resolution plot for the z coordinate. The effect this has on the acceptance is accounted for in the signal fraction and cut efficiency corrections described in section 5.4.

Figure 5.42 gives the same comparisons for the muon direction. The u_z variable shown here is of some interest, as it enters into the calculation of Q^2 . There is a slight deficit of P-Fitter events at the forward angles ($uz > 0.9$) as compared with the S-Fitter. This should have a negligible effect on the E_ν distribution, which is more sensitive to the visible muon energy than to u_z , but it will have a small effect on the Q^2 distribution.

In all of the above plots and allowing for the observed shape differences, it is clear that the P-Fitter gives a better resolution. However, as will be seen below, the difference is not enough to cause a significant change in the cross-section ratio.

The muon visible energy, with the same comparison of the P-Fitter and StancuFull reconstructions, is shown in figure 5.43. The agreement is reasonably good; this is to be expected, as in both cases the energy is ultimately derived from the total charge. However, as seen in the resolution plot, both overestimate the muon energy due to the extra charge created primarily by the pion. Thus the principal analysis uses the StancuFlux energy, which is based on the charge in the muon ring only, rather than the StancuFull. The bottom panels compare this (StancuFlux) energy to a loosely calibrated P-Fitter energy.

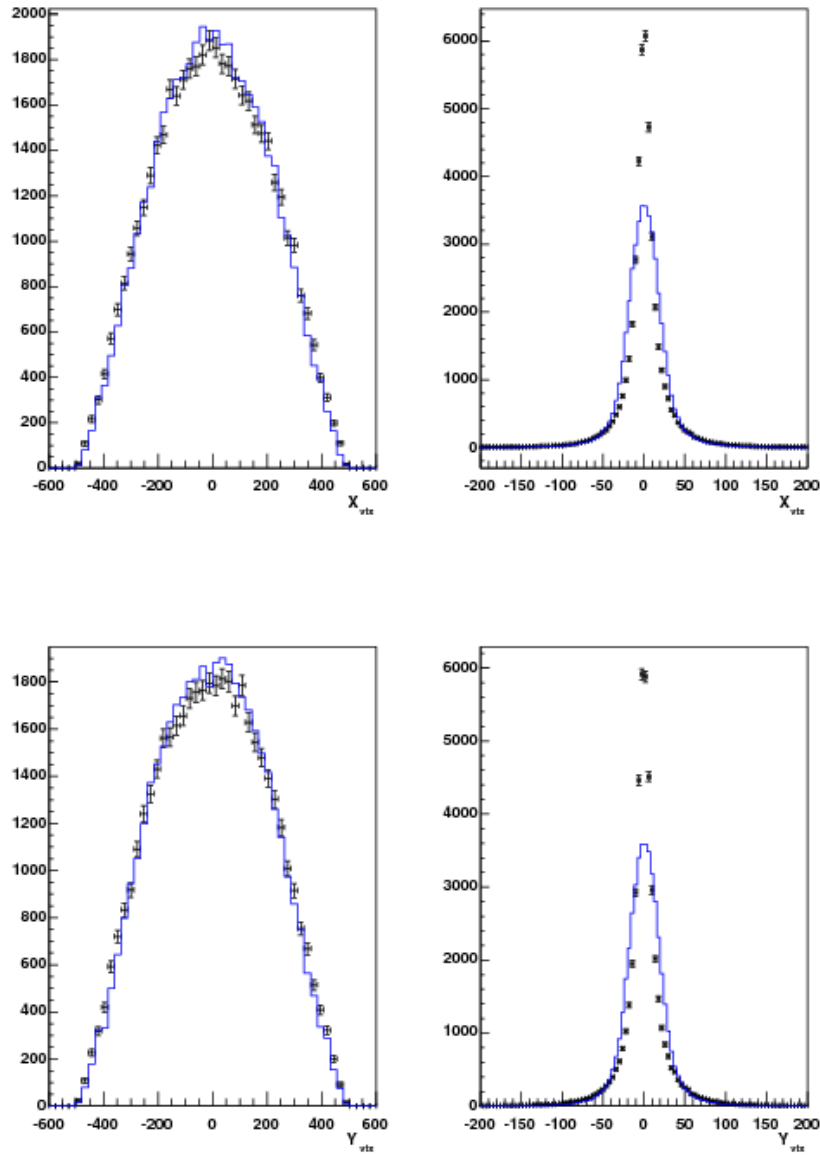


Figure 5.40: Comparison of StancuFull and One-track event vertex x (top) and y (bottom) coordinates. On the left are the data distributions with One-track as points with error bars and StancuFull as blue curve normalized to the same number of events. On the right are the resolution plots for each.

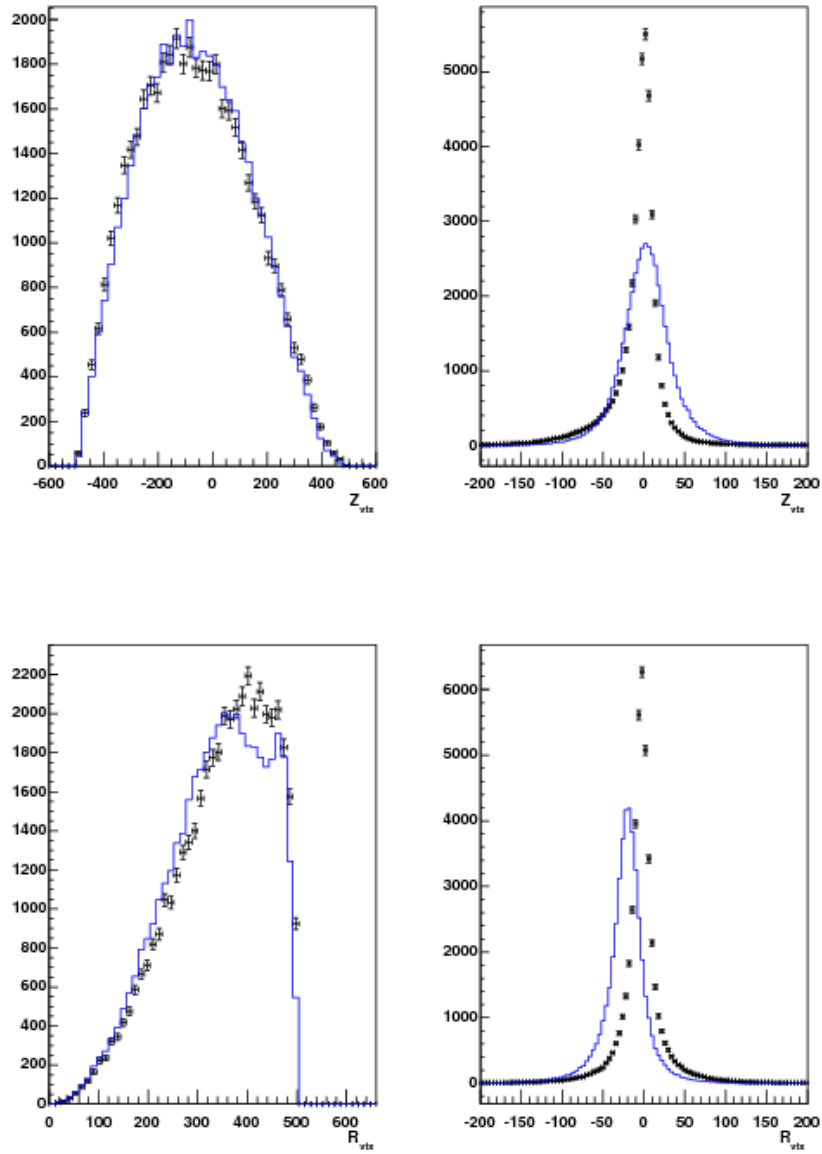


Figure 5.41: Comparison of StancuFull and One-track event vertex z (top) and R (bottom) coordinates. On the left are the data distributions with One-track as points with error bars and StancuFull as blue curve normalized to the same number of events. On the right are the resolution plots for each.

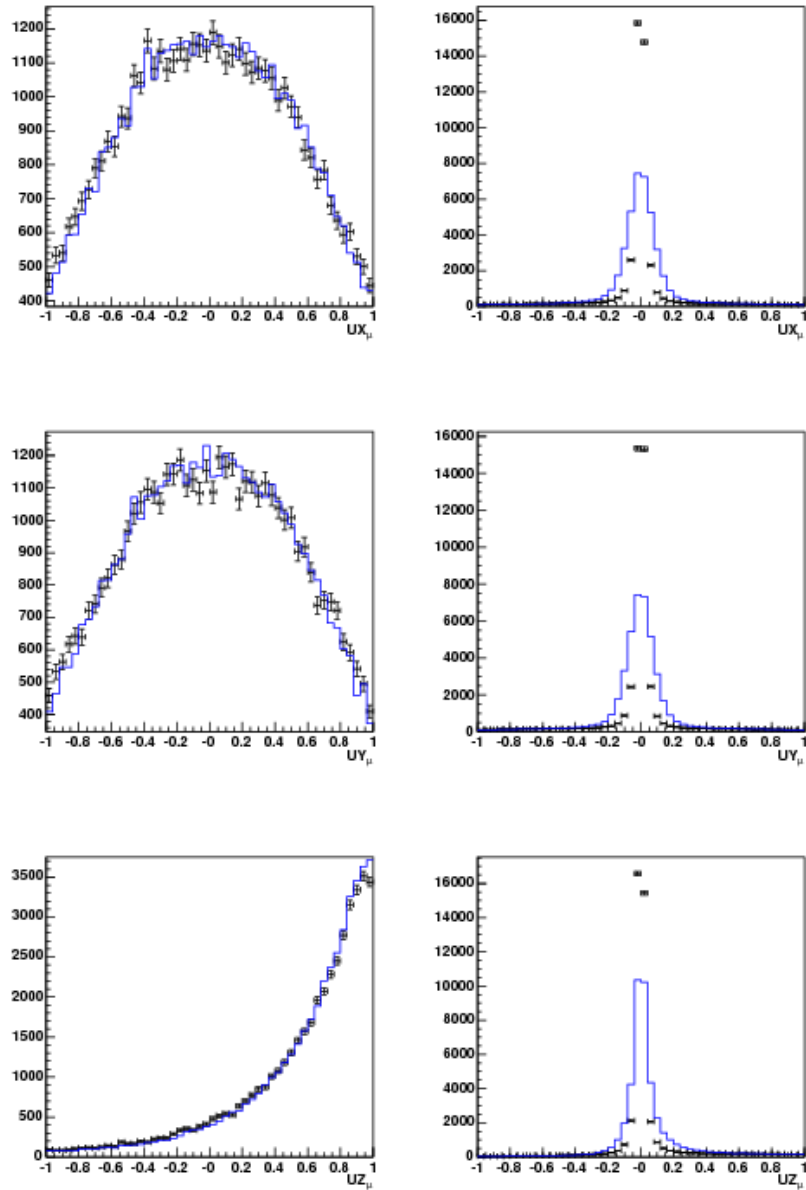


Figure 5.42: Comparison of StancuFull and One-track muon direction u_x (top) and u_y (middle) and u_z (bottom). On the left are the data distributions with One-track as points with error bars and StancuFull as blue curve normalized to the same number of events. On the right are the resolution plots for each.

This calibrated energy is simply $aE + b$ where E is the raw P-Fitter energy and where a and b are determined by the threshold and the peak muon visible energy. The motivation for using this variable was to have an energy which, like the StancuFlux energy, was closer to the true visible energy of the muon in case the E_nu unfolding algorithm was unstable for a large difference in the reconstructed and true energies. As it turns out the Bayesian unfolding procedure is quite robust and gives consistent results, as will be seen, whether one uses the raw P-Fitter energy or this corrected one.

Figures 5.44 and 5.45 give these same comparisons for the reconstructed neutrino energy E_ν and momentum transfer Q^2 . Again the top panels use the Full (raw) muon visible energy in calculating these while the bottom panels are for the Flux (corrected) muon energy. The difference in the reconstructed E_ν , which comes almost entirely from the difference in muon visible energy, is removed by the unfolding procedure with consistent results for whatever visible energy is used. The difference in reconstructed Q^2 comes from both the muon energy and the small discrepancy in u_z . Note that we do not extract a ratio as a function of Q^2 because of the disagreement between data and MC in that variable (see section 5.7.3).

In obtaining the $CC\pi^+$ to $CCQE$ ratio for this comparison, we repeated all procedures used for the main analysis but with the P-Fitter used for the $CC\pi^+$ sample. As described previously the muon energy for the P-Fitter has been calibrated; a ratio was calculated using both the calibrated and uncalibrated versions. The $CCQE$ sample used in this comparison was reconstructed using the S-Fitter, and is identical to that used in the main analysis. As with the StancuFull check described above, we made the comparison between the P-Fitter and S-Fitter using the FSI-corrected ratio.

In figure 5.46 the reconstructed neutrino energy distributions for both $CC\pi^+$ and $CCQE$ data samples are shown. The most significant difference between reconstructed neutrino energy distributions for the $CC\pi^+$ sample in figure 5.46 is that between the S-Fitter and the original (uncalibrated) P-Fitter.

Figure 5.47 shows the Monte Carlo prediction for the reconstructed neutrino energy distribution of $CC\pi^+$ events before and after the cuts for this sample were applied. In

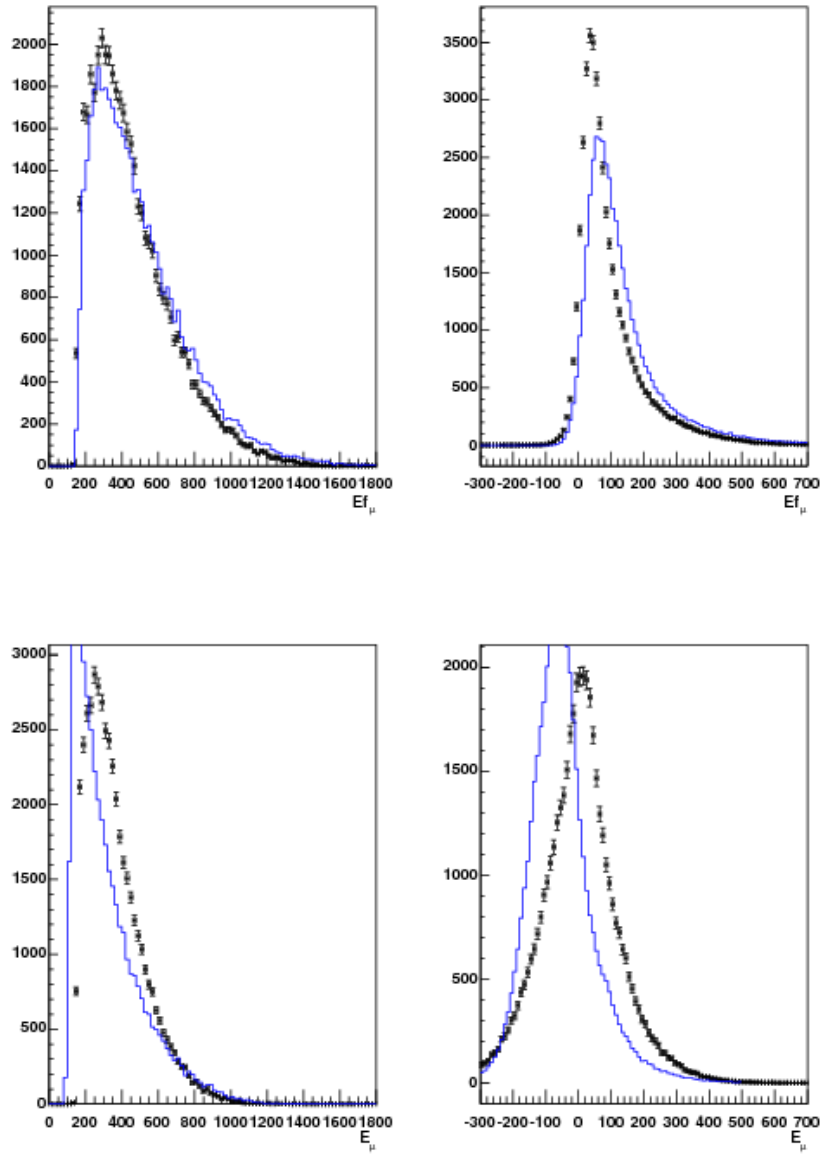


Figure 5.43: Comparison of muon visible energy for StancuFull and One-track (top) and StancuFlux vs One-track corrected (bottom). On the left are the data distributions with One-track as points with error bars and StancuFull as blue curve normalized to the same number of events. On the right are the resolution plots for each.

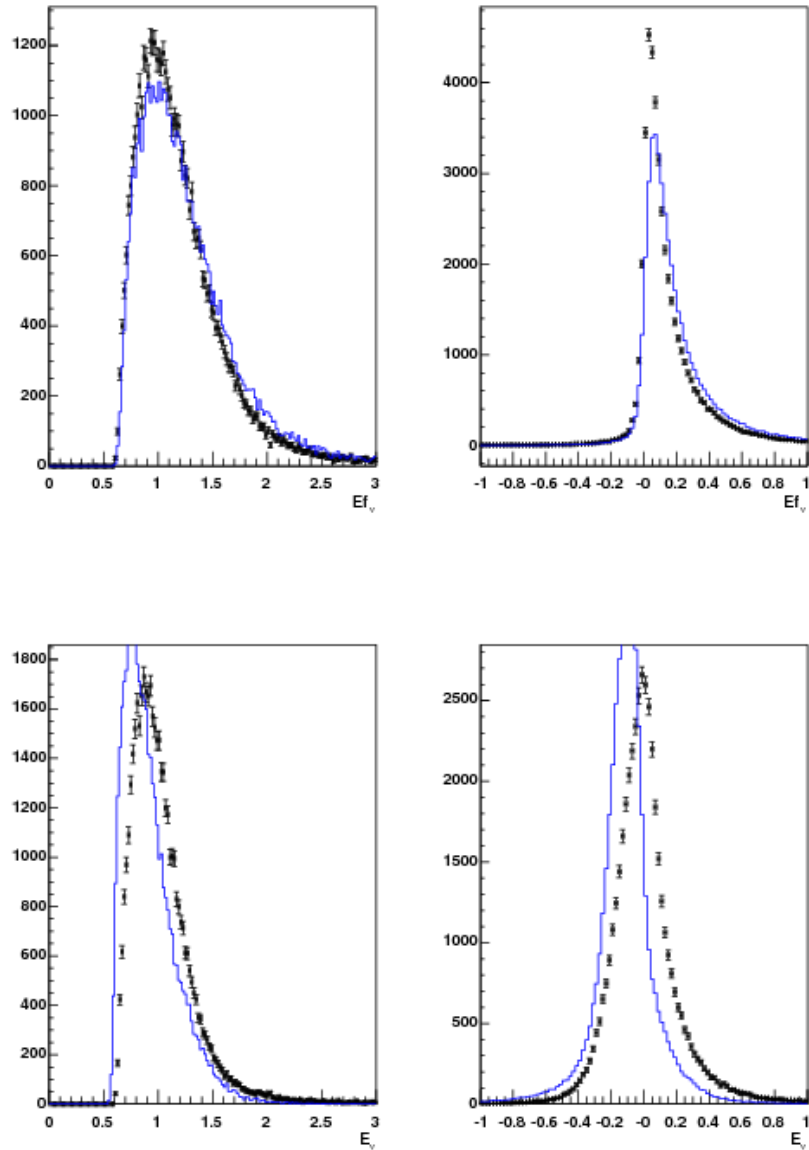


Figure 5.44: Comparison of reconstructed E_ν for StancuFull and One-track (top) and StancuFlux and One-track corrected (bottom). On the left are the data distributions with One-track as points with error bars and StancuFull as blue curve normalized to the same number of events. On the right are the resolution plots for each.

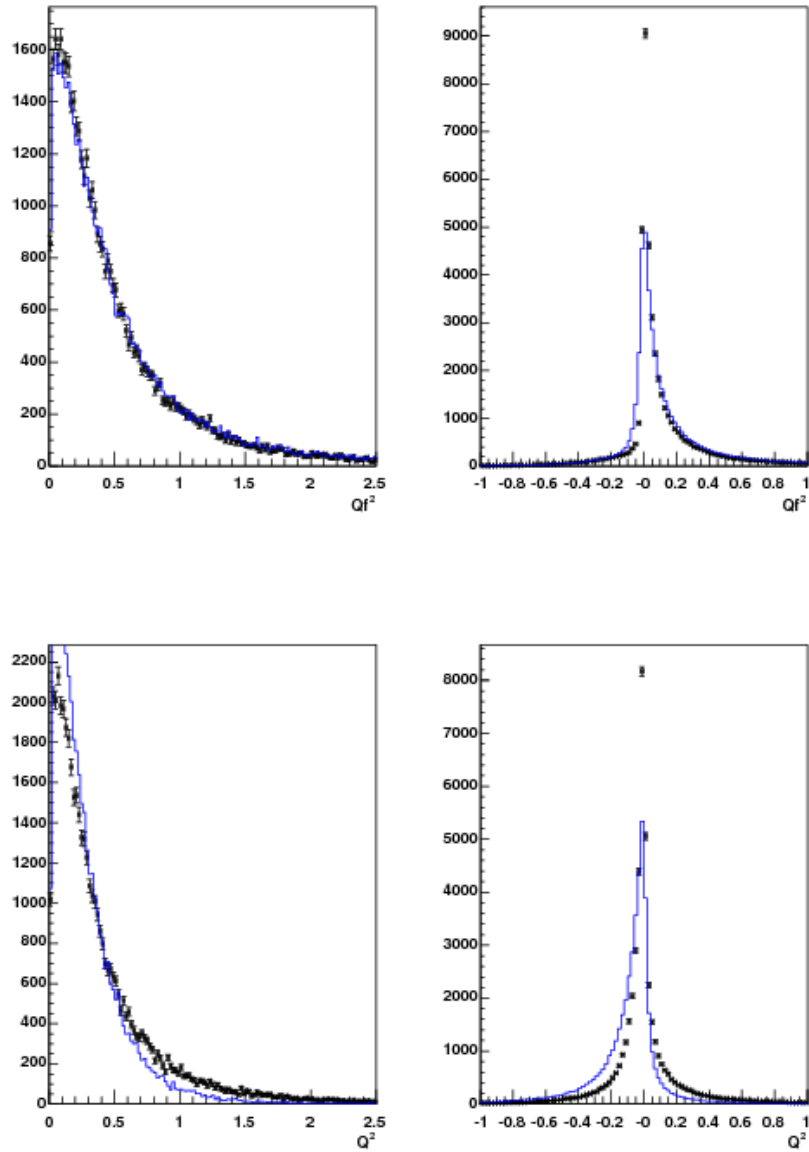


Figure 5.45: Comparison of reconstructed neutrino Q^2 for StancuFull and One-track (top) and StancuFlux and One-track corrected (bottom). On the left are the data distributions with One-track as points with error bars and StancuFull as blue curve normalized to the same number of events. On the right are the resolution plots for each.

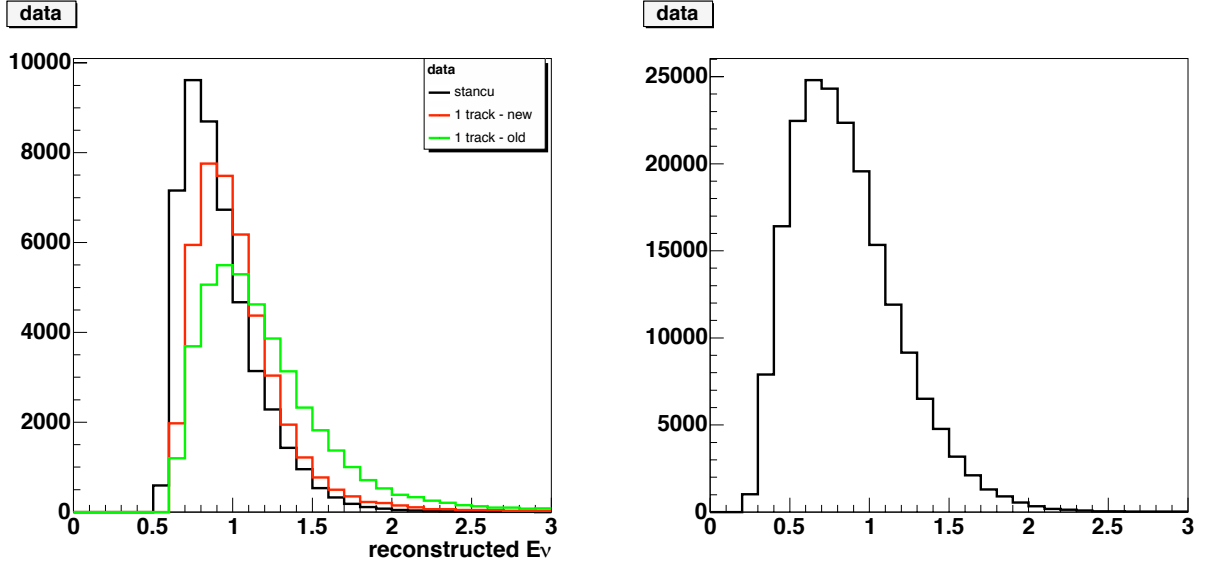


Figure 5.46: Reconstructed neutrino energy for neutrino mode data for $CC\pi^+$ (left) and $CCQE$ (right). For $CC\pi^+$ the Stancu fitter (black) is compared with two versions of one-track fitter, original (old - green) and with muon energy adjustment (new - red).

figure 5.48 the distributions of generated neutrino energy for the $CC\pi^+$ sample and for all generated events are shown. From the comparison of the generated and reconstructed neutrino energy distributions in figures 5.47 and 5.48 the one-track reconstructed distribution is the most similar to the generated one.

The signal fraction and cut efficiency for $CC\pi^+$ events reconstructed with the three different fitters (S-Fitter, P-Fitter, and calibrated P-Fitter) are compared in figure 5.49. It is worth notice that the signal fraction for the P-Fitter is higher than that for the S-Fatter. The purity of the $CC\pi^+$ sample is higher when cuts are applied on P-Fitter variables. The difference in the cut efficiency between the S-Fitter and the P-Fitters comes from the fact that more events are reconstructed with the former.

The unfolding matrices for the three reconstructions of the $CC\pi^+$ sample are presented in figure 5.50. From this figure we can see that indeed the reconstructed neutrino energy distribution for one-track has a shape close to the generated energy distribution, and the unfolding matrix is mostly diagonal, while for the other two cases the highest elements are

shiften one or two bins to the right of the diagonal.

In figure 5.51 the reconstructed neutrino energy distributions corrected for the background and the unfolded neutrino energy distributions are shown. The distributions in unfolded energy for all fitters look the same, confirming that the unfolding procedure works well.

Finally, in figure 5.52 the $CC\pi^+$ to $CCQE$ ratios for all fitters are compared. The differences among the results obtained are negligible and we can draw the conclusion that the analysis in general and the unfolding procedure in particular are not sensitive to the reconstruction scheme used.

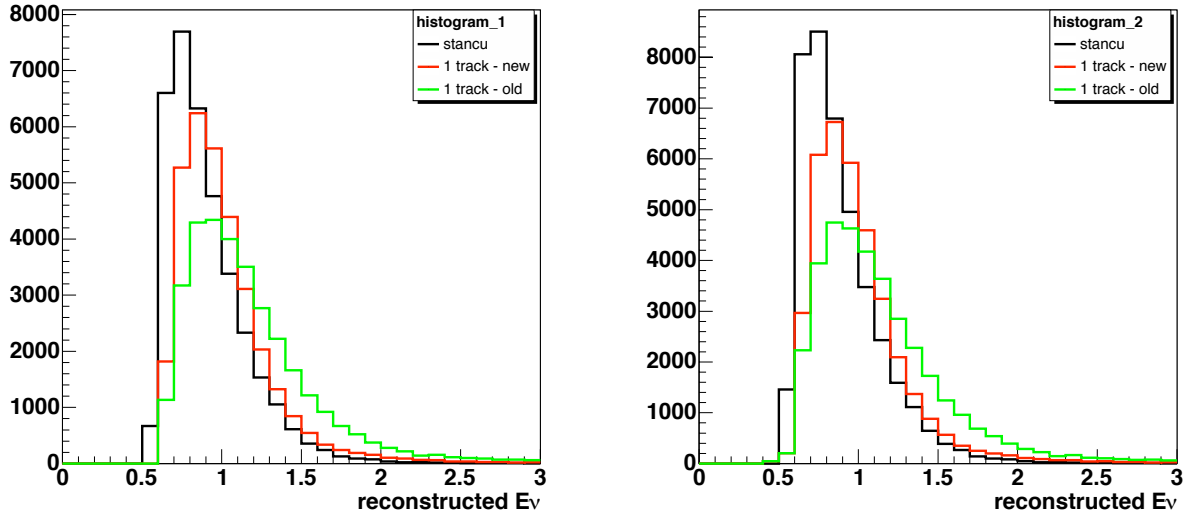


Figure 5.47: The reconstructed energy distributions for selected $CC\pi^+$ events before (right) and after (left) cuts.

5.7.3 Q^2 Reweighting

The $CC\pi^+$ sample exhibits significant disagreement between data and Monte Carlo in reconstructed Q^2 (see figure 5.53). This discrepancy may be symptomatic of problems with the Rein-Sehgal model for pion production used in the MC. A simple reweighting check was done to test whether the Q^2 disagreement has an effect on the $CC\pi^+$ to $CCQE$

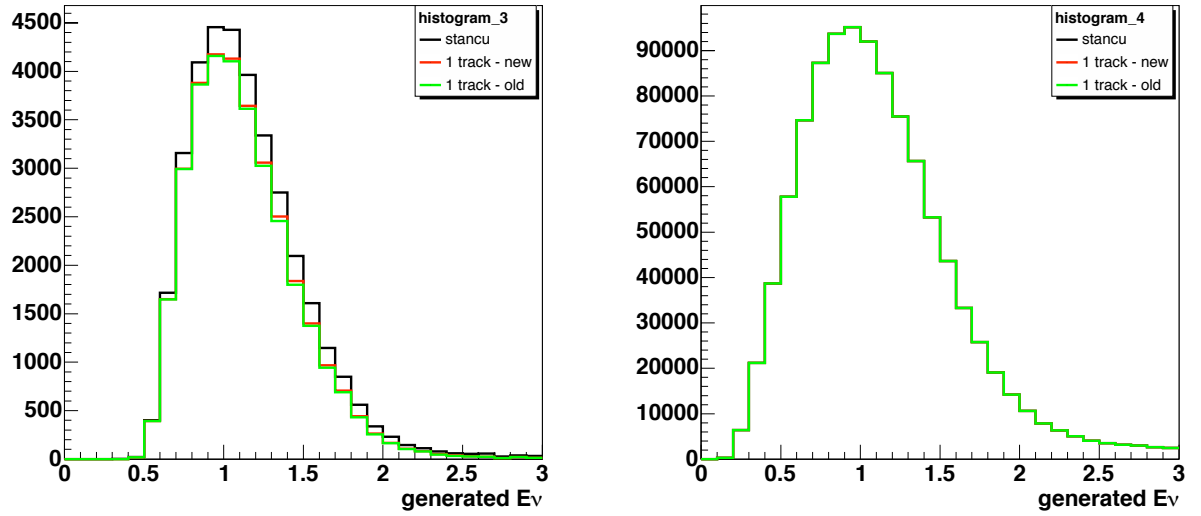


Figure 5.48: The generated neutrino energy distribution for the reconstructed $CC\pi^+$ events after cuts (left) and neutrino energy distribution for all events in the Monte Carlo sample (right).

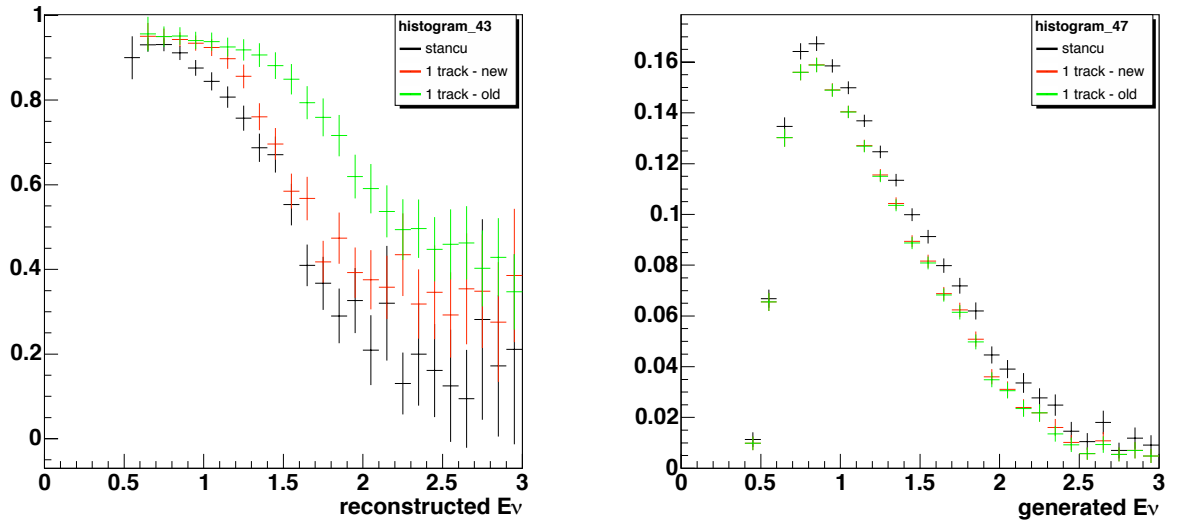


Figure 5.49: The signal fraction (left) and cut efficiency (right) for the $CC\pi^+$ sample for three fitters.

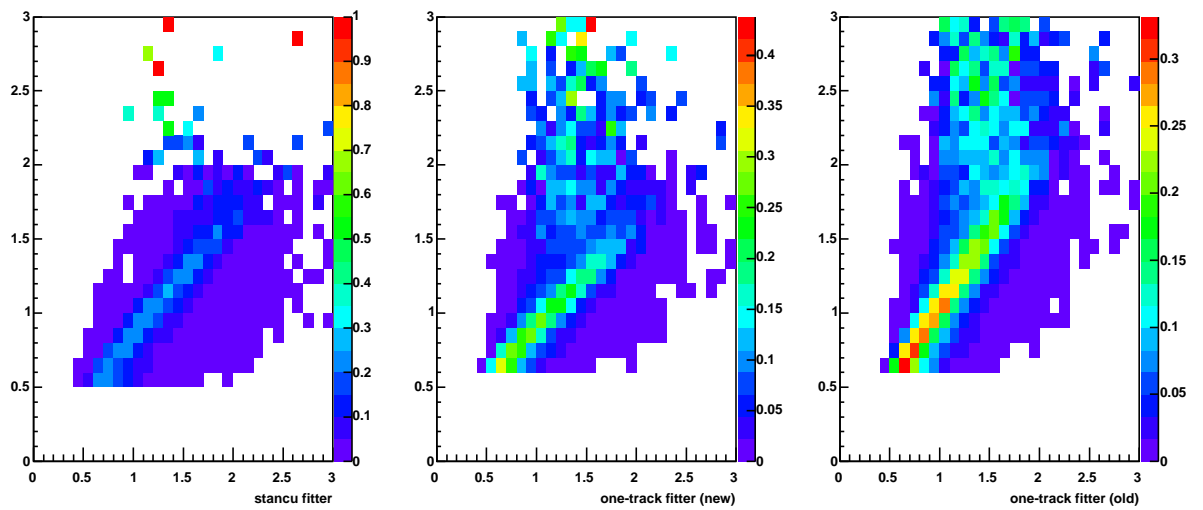


Figure 5.50: The unsmeared matrices for the three fitters.

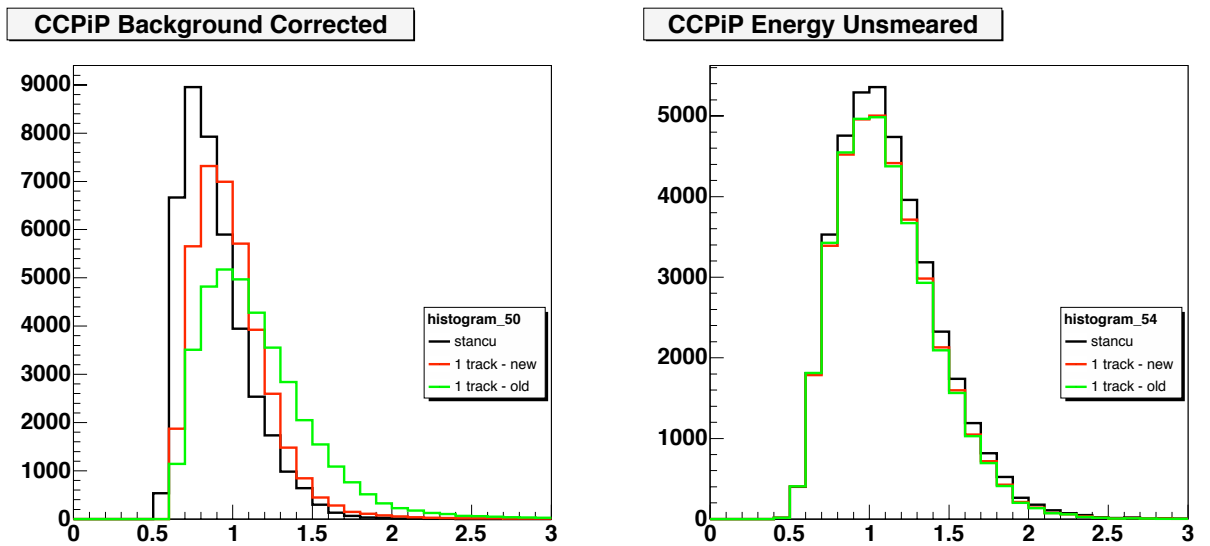


Figure 5.51: The background corrected reconstructed neutrino energy distribution (left) and unsmeared energy distribution (right) for the $CC\pi^+$ data sample.

ratio. A Monte Carlo sample was reweighted to agree with the data in Q^2 , and the analysis was repeated using this sample. The results are shown in figures 5.54 and 5.55. The reweighting has only a small effect on the ratio, and that only above about 1.1 GeV. We can conclude that the Q^2 disagreement is not indicative of some underlying problem in $CC\pi^+$ reconstruction. The reweighted Q^2 variation was included in our uncertainties.

5.7.4 Pion Momentum

A simple check was performed to test how sensitive the ratio we calculate is to possible errors in the predicted momentum distribution of the pions produced in $CC\pi^+$ interactions. To constrain the π^0 background in the MiniBooNE oscillation analysis, the measured π^0 production was used to obtain correction factors, as a function of pion momentum, to be applied to the Monte Carlo. Although this reweighting applies to π^0 and not π^+ production, it can be taken as a very rough estimate of the size of a one-sigma variation in the predicted π^+ momentum distribution. To perform the pion momentum check, we reweighted all $CC\pi^+$ events by pion momentum, using the event weights obtained from the π^0 measurement. Moreover, the check was performed using both StancuFlux and StancuFull reconstructions (cf. section 6); this was done in order to check whether one or the other reconstruction was preferable in that it was less sensitive to this variation.

Figure 5.56 compares the result for the ratio using this π^+ variation with that for the central value Monte Carlo, for both StancuFlux and StancuFull reconstructions. The reweighted and unreweighted distributions agree rather closely up to about 1 GeV; above 1 GeV the reweighted distribution is about 5-15% lower. This discrepancy is roughly the same size for both reconstructions. This π^+ variation (with StancuFlux reconstruction) was included in our systematic uncertainties.

5.7.5 Nucleon Momentum

Throughout the main analysis, we have treated the target nucleus using the relativistic Fermi Gas model. Uncertainties on the Fermi momentum (p_F) and binding energy (E_B)

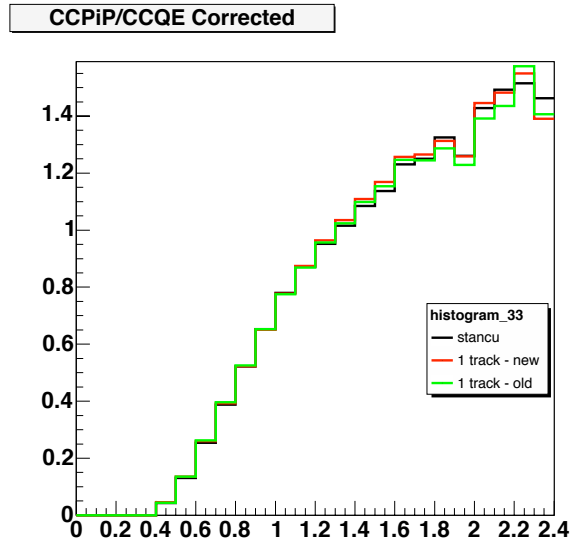


Figure 5.52: The $CC\pi^+$ to $CCQE$ ratio for stancu fitter and one track fitter without energy adjustment.

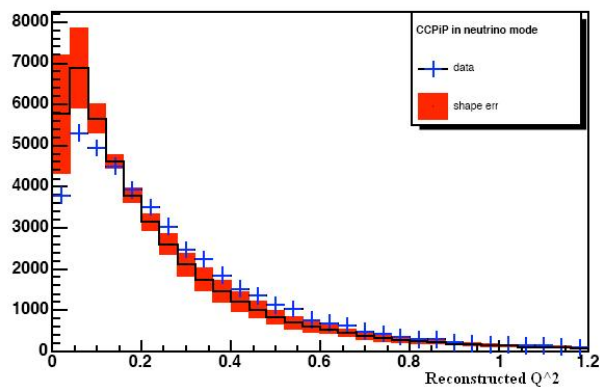


Figure 5.53: Data - Monte Carlo comparison of Q^2 in $CC\pi^+$. Black: Monte Carlo; blue: data.

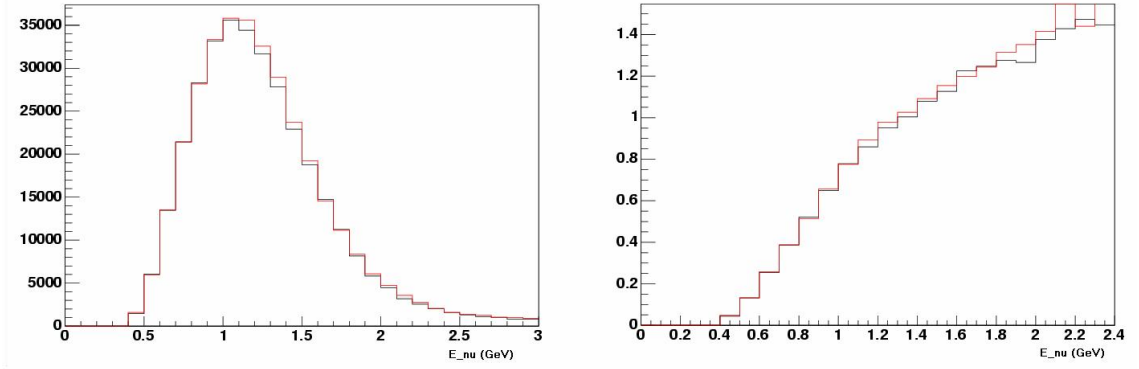


Figure 5.54: Left: corrected $CC\pi^+$ data; right: $CC\pi^+$ to $CCQE$ ratio. Black: central value; red: reweighted

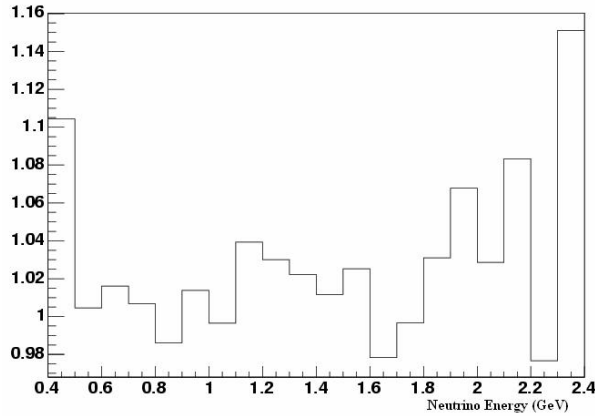


Figure 5.55: Ratio of corrected $CC\pi^+$ data with q^2 reweighting to corrected data without reweighting.

parameters in the Fermi Gas model are included in the error calculation for the ratio analysis. However, the question might be posed whether these uncertainties are sufficient to cover the dependence of the ratio result on the nucleon momentum distribution. In particular, it might be asked how sensitive the ratio analysis is not only to the values of the parameters of the nuclear model but also to the choice of nuclear model itself.

Note that such an effect would not be corrected by our energy unfolding procedure. A basic assumption of any energy unfolding scheme is that the mapping from true energy to reconstructed energy is the same in the simulation as it is in the data. If the nuclear model used in our Monte Carlo were incorrect, then the Monte Carlo would not correctly predict the reconstructed energy distributions that would arise from interactions at a given true

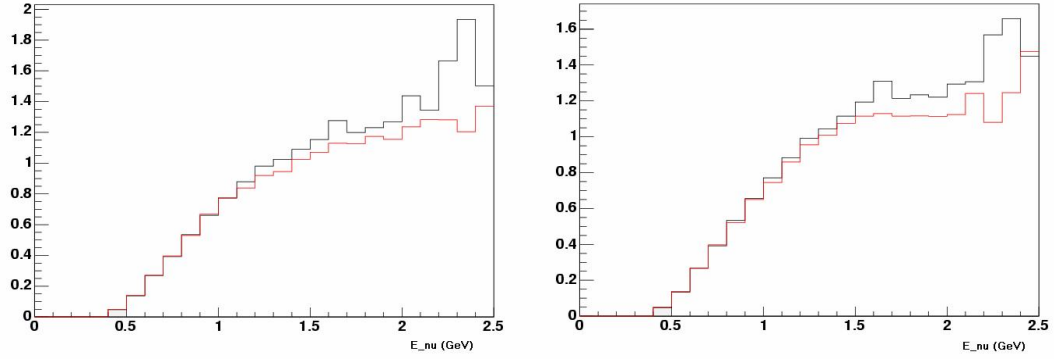


Figure 5.56: $CC\pi^+$ to $CCQE$ ratio with CV Monte Carlo (black) and with the reweighted π^+ variation (red). Left: StancuFlux reconstruction; right: StancuFull reconstruction.

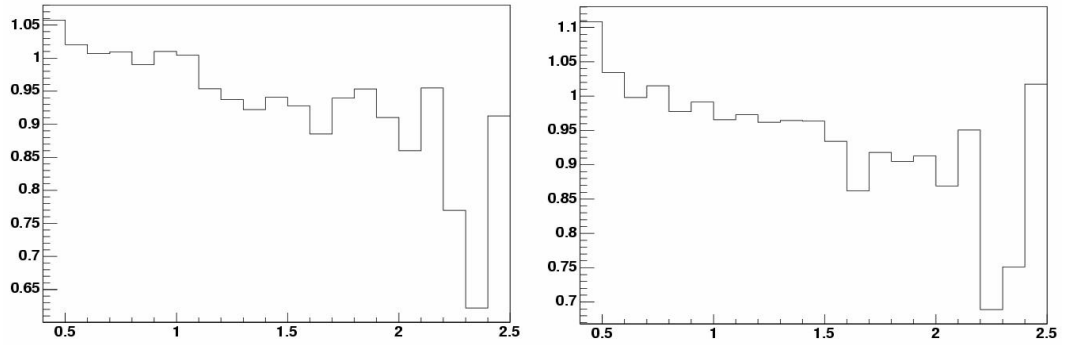


Figure 5.57: Ratio of ratio result with π^+ unisim to result with CV MC. Left: StancuFlux reconstruction; right: StancuFull reconstruction.

energy. Thus, error in the nuclear model translates into error in our unfolded distributions, without being removed by unfolding.

In [99], Benhar *et al.* compare the neutrino energy reconstruction obtained using the Fermi Gas model with that using a Spectral Function for $CCQE$. Figure 5.58 reproduces a plot from their paper showing the neutrino energy distributions corresponding to two choices of E_μ and θ_μ under the Fermi Gas (FG) model and under the Spectral Function (SF) model. The arrows indicate the reconstructed neutrino energy for those parameters, assuming constant binding energy and a target neutron at rest (see eq. 4.19). One may note that the SF distribution looks something like the FG distribution shifted upward one bin in energy. This effect is shown in figure 5.59, which reproduces the top panel of figure 5.58 and overlays the FG distribution from that figure shifted upward by 30 MeV. The shifted FG distribution agrees well with the SF everywhere except at the peak of the distribution. With this in mind, we repeated the ratio analysis using three MC variations in which all generated neutrino energies are shifted upward by 10, 20, and 30 MeV. These variations are intended to approximate the effect of using an alternative nuclear model, such as the SF, which would require a completely new neutrino interaction simulation.

Figure 5.60 shows the distributions in generated energy for the FSI-corrected signal events before and after cuts and the corresponding cut efficiencies for each of the three energy shifts. These can be compared with figure 5.61, which shows the cross-section multisim excursions for the FSI-corrected analysis, as described in section 5.6.1. The same sets of figures for the observed ($CC\pi^+$ -like and $CCQE$ -like) samples are presented in figures 5.64 and 5.65. In figures 5 (FSI-corrected) and 9 (observed), the background-corrected data is shown in reconstructed energy (upper panel) together with the unfolded and efficiency-corrected distributions, again using the CV and generated energy shifted MC variations. Plots of the cross-section multisim excursions for the same quantities are shown in figures 5.63 and 5.67. The $CC\pi^+$ to $CCQE$ ratios (both observed and FSI-corrected) obtained using the modified generated energies are shown in figure 5.68 and are compared with the ratios obtained in the cross-section multisim excursions for the main analysis.

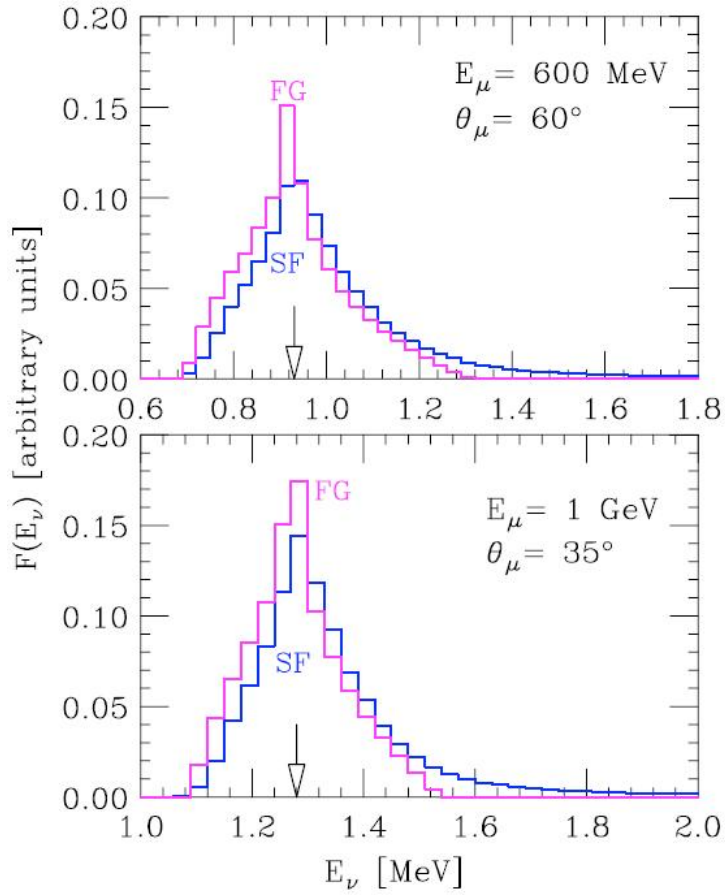


Figure 5.58: For two choices of E_μ and θ_μ , the neutrino energy distributions that contribute to $CCQE$ interactions with the given kinematics under the Fermi Gas model and under the Spectral Function model. The arrows indicate the neutrino energy that will be reconstructed for the given kinematics, assuming a two-body collision.

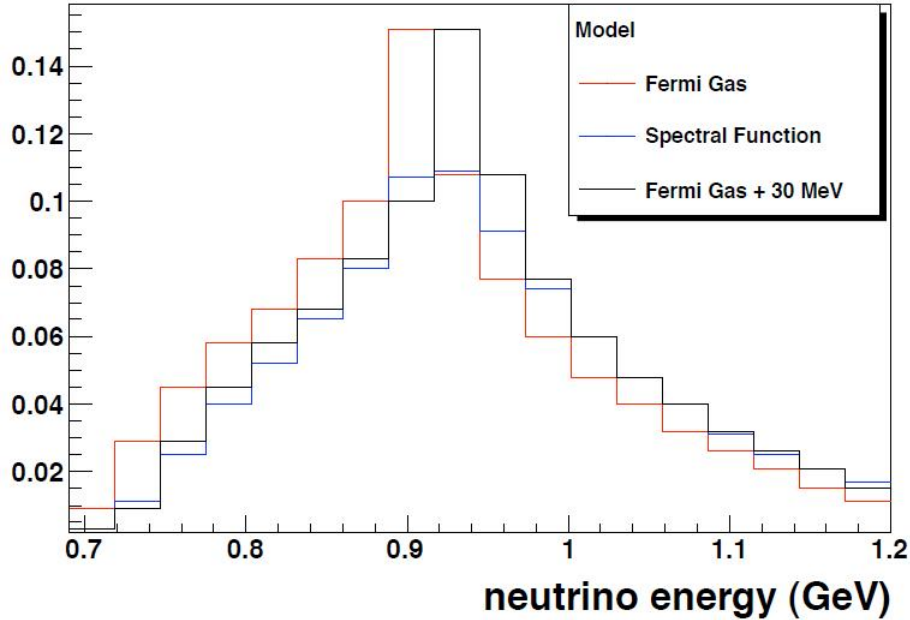


Figure 5.59: For $E_\mu = 600$ MeV and $\theta_\mu = 60^\circ$, the neutrino energy distributions that contribute to $CCQE$ interactions with the given kinematics under the Fermi Gas model (red), the Spectral Function model (blue), and the Fermi Gas model shifted upward by 30 MeV.

Comparing the results with the modified generated energy (figures 5.60, 5.64, 5.62, 5.66, 5.68) with the cross-section multisim excursions (figures 5.61, 5.65, 5.63, 5.67, and 5.68), one can see that the spread of the modified energy variations lies within the spread of the multisim excursions. In other words, the effects of varying the cross-section parameters (including p_F and E_B) are larger than the effects of altering the nuclear model in a reasonable way. We can conclude that the cross-section uncertainties calculated for the ratio already cover the possible effects of an incorrect nuclear model, and we do not need to introduce any additional systematic uncertainty to account for this.

5.8 Results

We present here the results of the cross-section ratio measurement calculated using the method outlined in sections 5.2 - 5.5. Figure 5.69 shows the effective $CC\pi^+$ to $CCQE$ cross-section ratio. Figure 5.70 shows the FSI-corrected ratio. Table 5.7 provides our

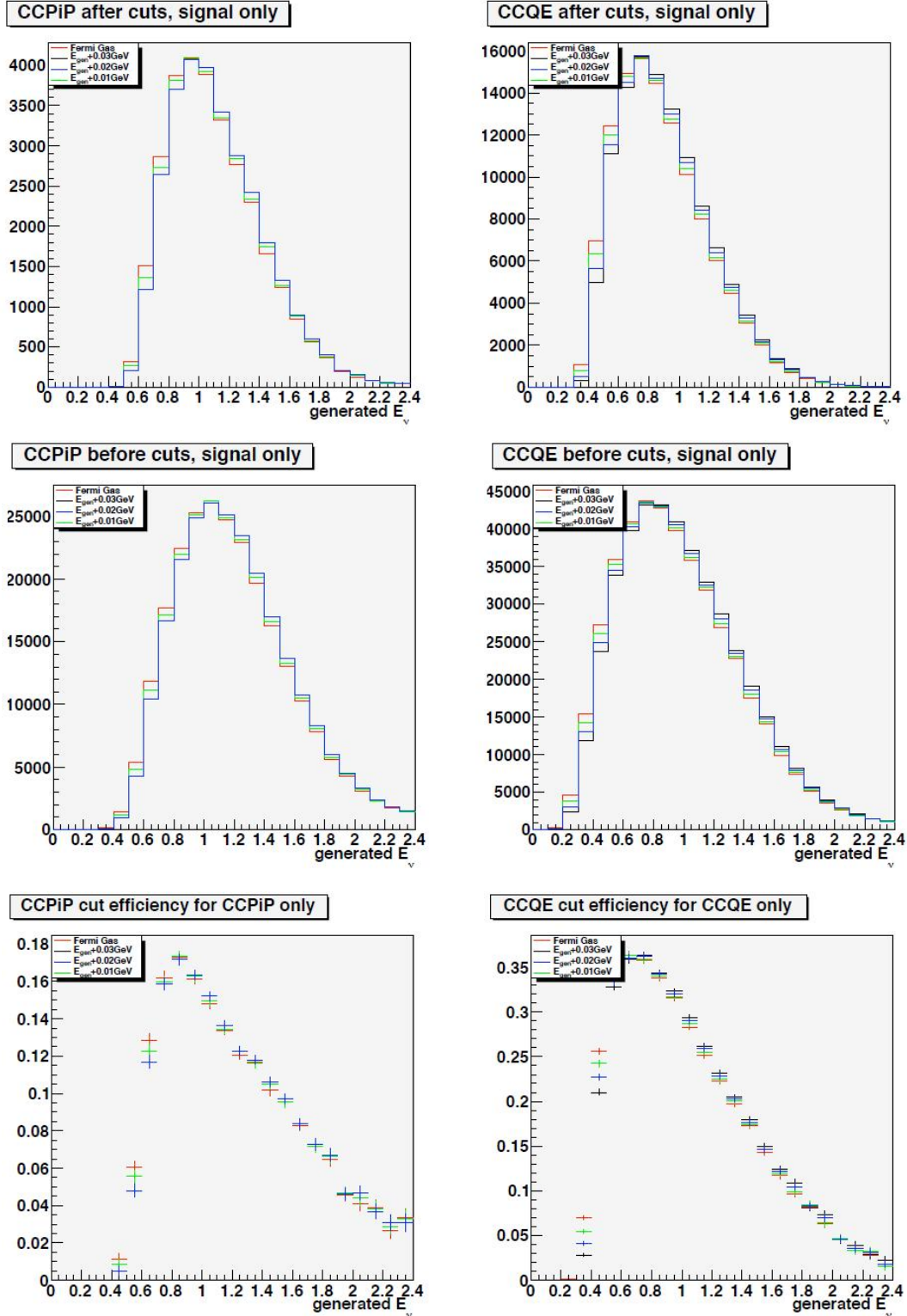


Figure 5.60: $CC\pi^+$ and $CCQE$ distributions in generated neutrino energy before (top) and after (middle) cuts and $CC\pi^+$ and $CCQE$ cut efficiencies (bottom) with standard Fermi gas model (red) and with Fermi Gas model shifted upward by 10 (green), 20 (blue), and 30 (black) MeV.

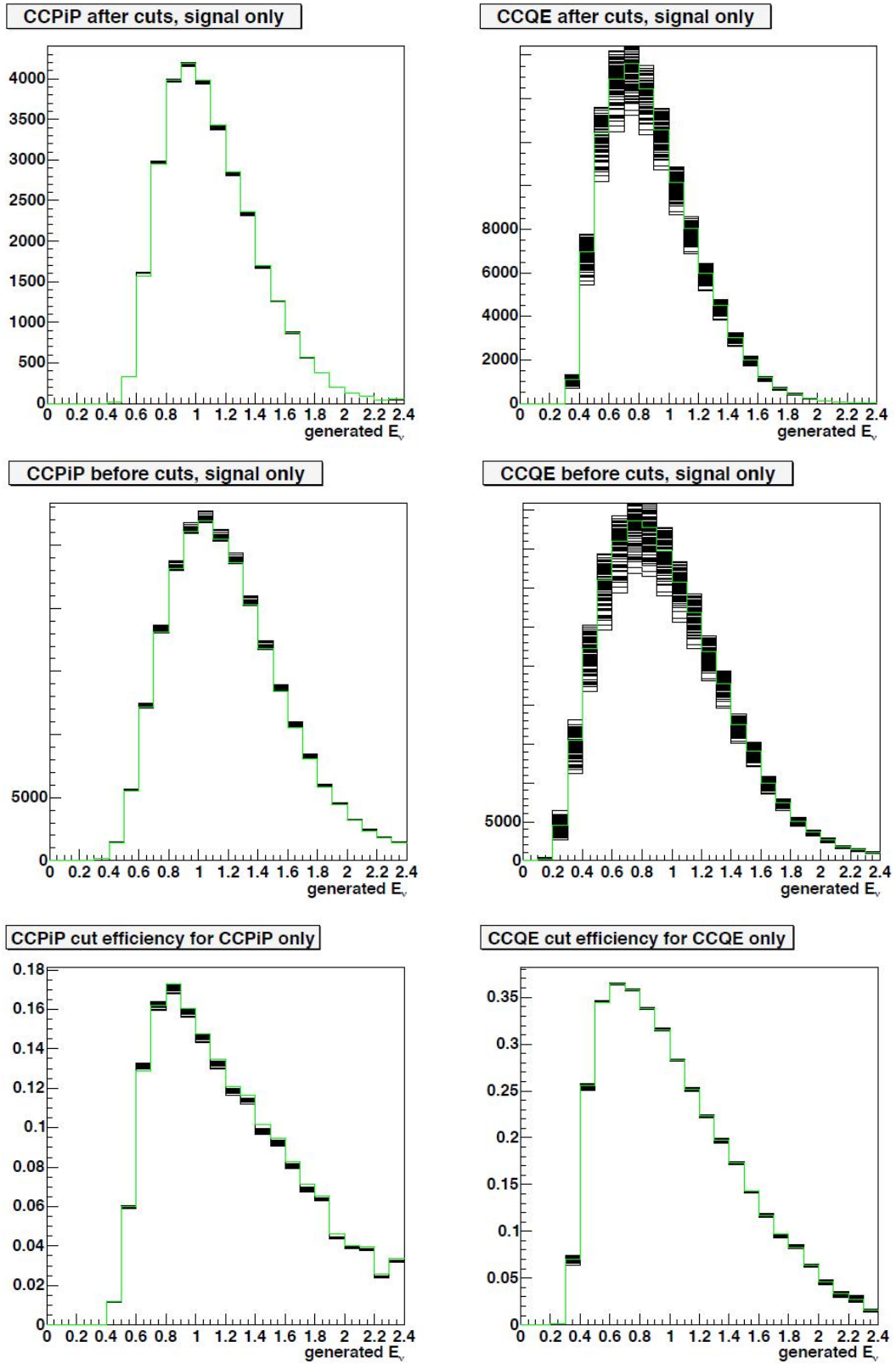


Figure 5.61: $CC\pi^+$ and $CCQE$ distributions in generated neutrino energy before (top) and after (middle) cuts and $CC\pi^+$ and $CCQE$ cut efficiencies (bottom), with cross-section multisim excursions.

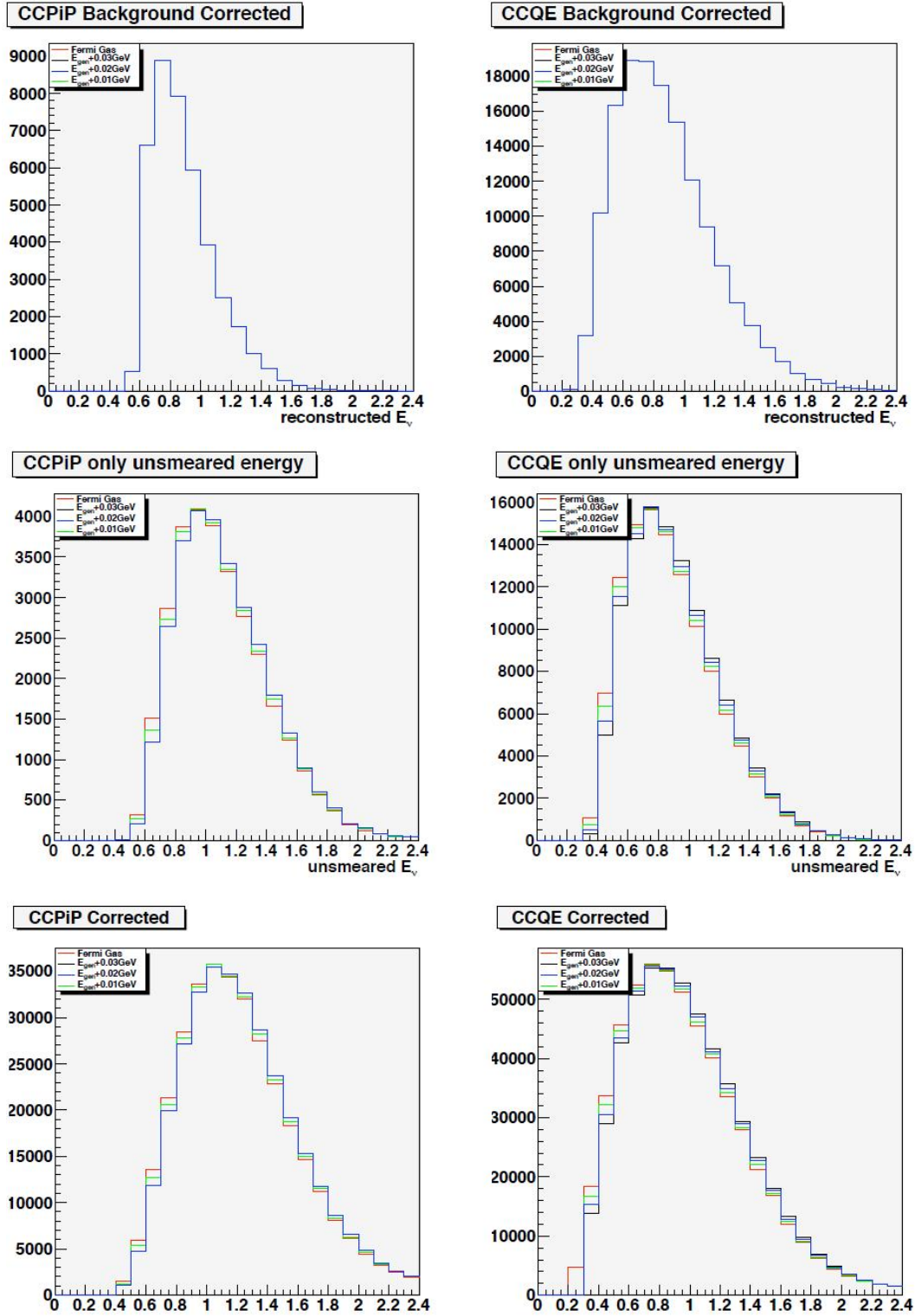


Figure 5.62: Background-corrected (top), unfolded (middle), and fully corrected (bottom) $CC\pi^+$ and $CCQE$ distributions in reconstructed neutrino energy with standard Fermi gas model (red) and with Fermi Gas model shifted upward by 10 (green), 20 (blue), and 30 (black) MeV.

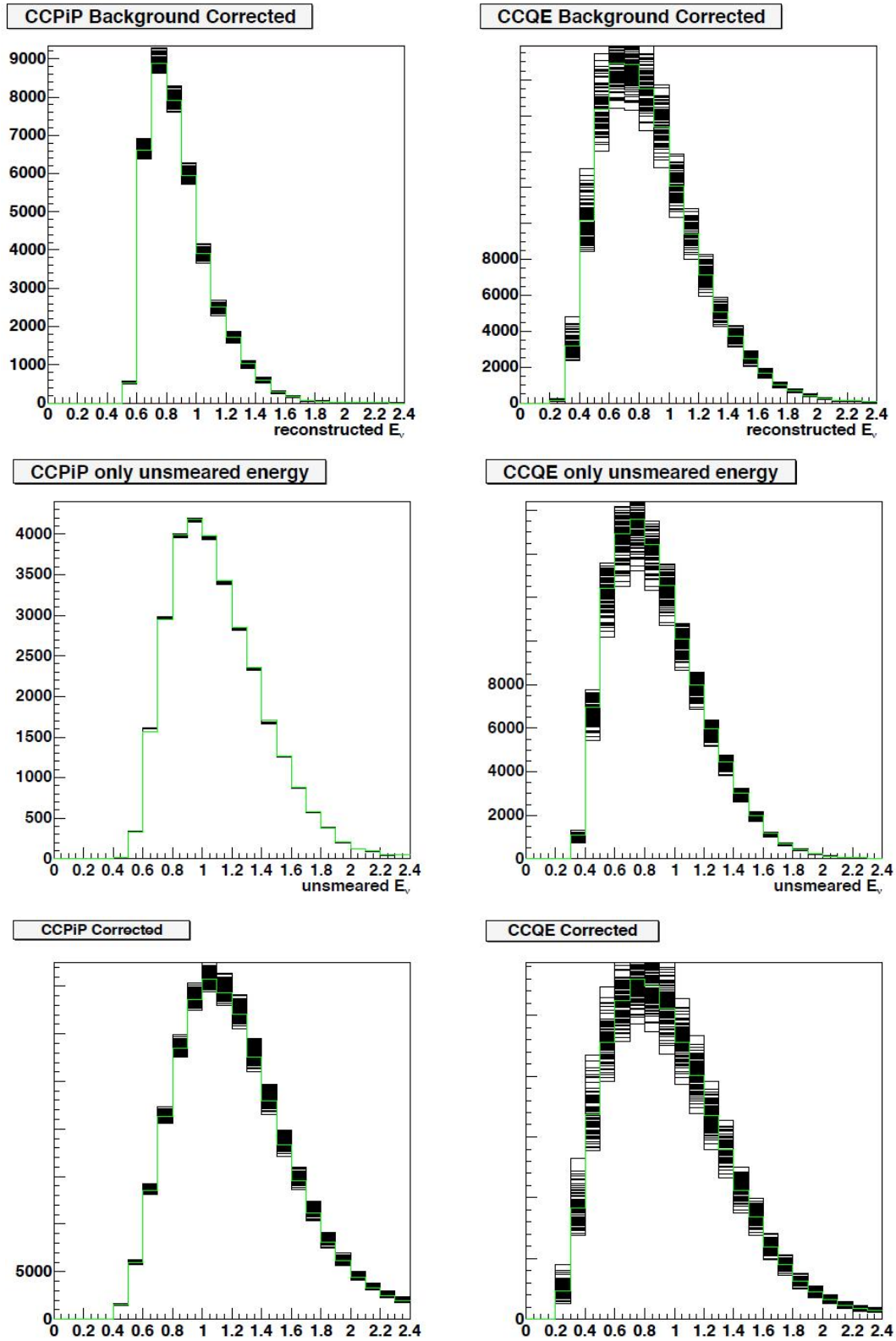


Figure 5.63: Background-corrected (top), unfolded (middle), and fully corrected (bottom) $CC\pi^+$ and $CCQE$ distributions in reconstructed neutrino energy, with cross-section multibin excursions.

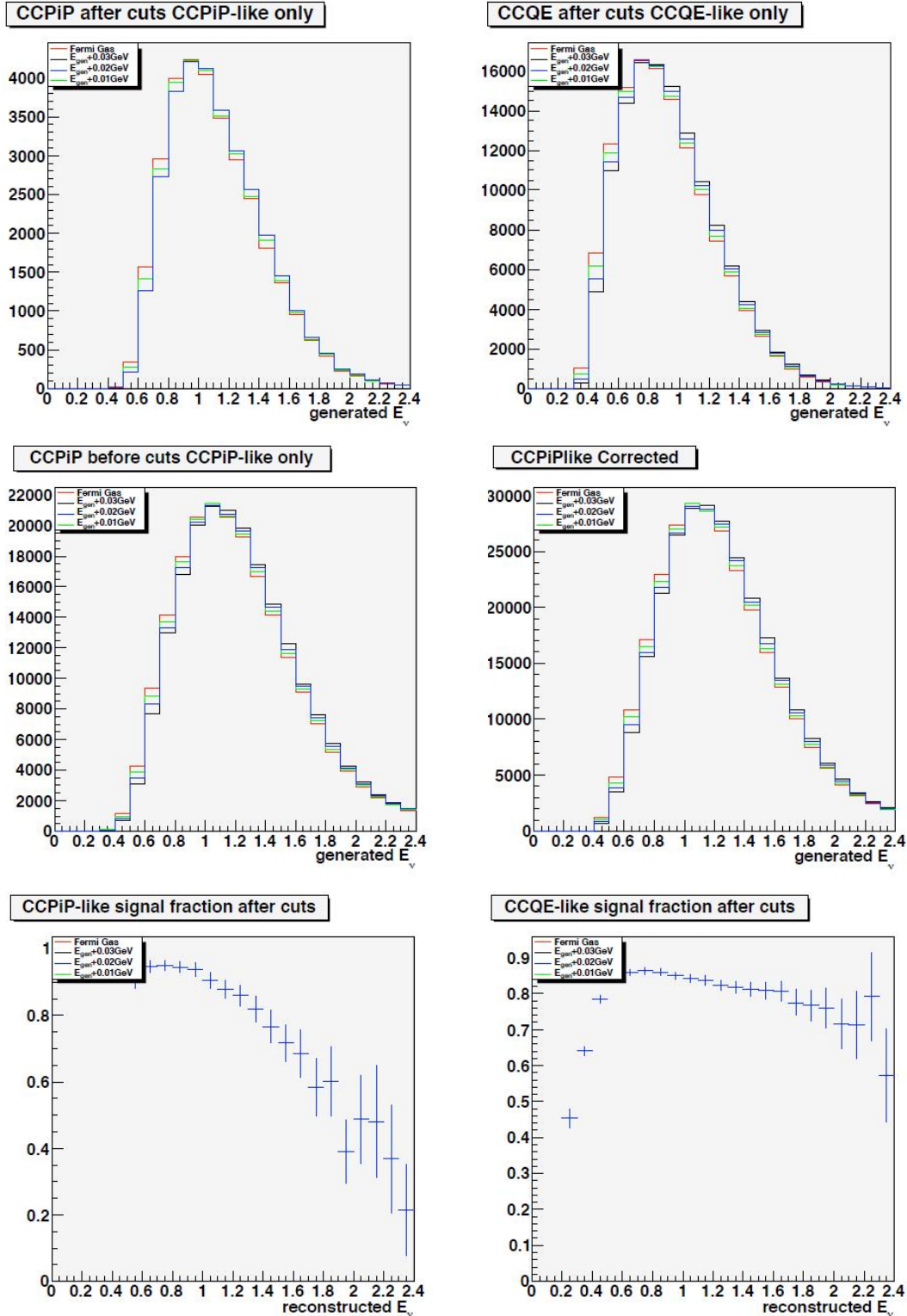


Figure 5.64: CC π^+ -like and CCQE-like distributions in generated neutrino energy before (top) and after (middle) cuts and CC π^+ -like and CCQE-like cut efficiencies (bottom) with standard Fermi gas model (red) and with Fermi Gas model shifted upward by 10 (green), 20 (blue), and 30 (black) MeV.

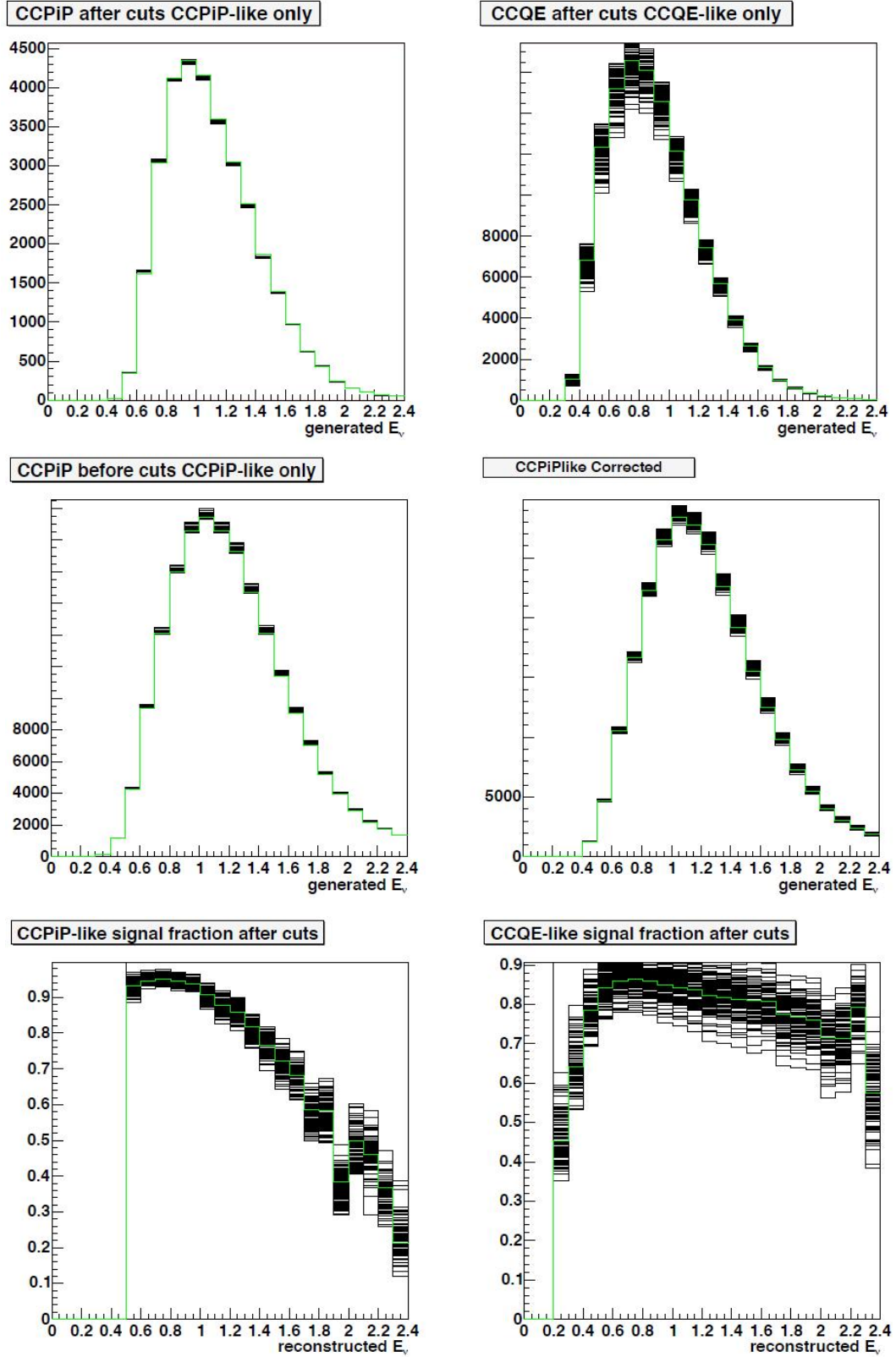


Figure 5.65: CC π^+ -like and CCQE-like distributions in generated neutrino energy before (top) and after (middle) cuts and CC π^+ -like and CCQE-like cut efficiencies (bottom), with cross-section multisim excursions.

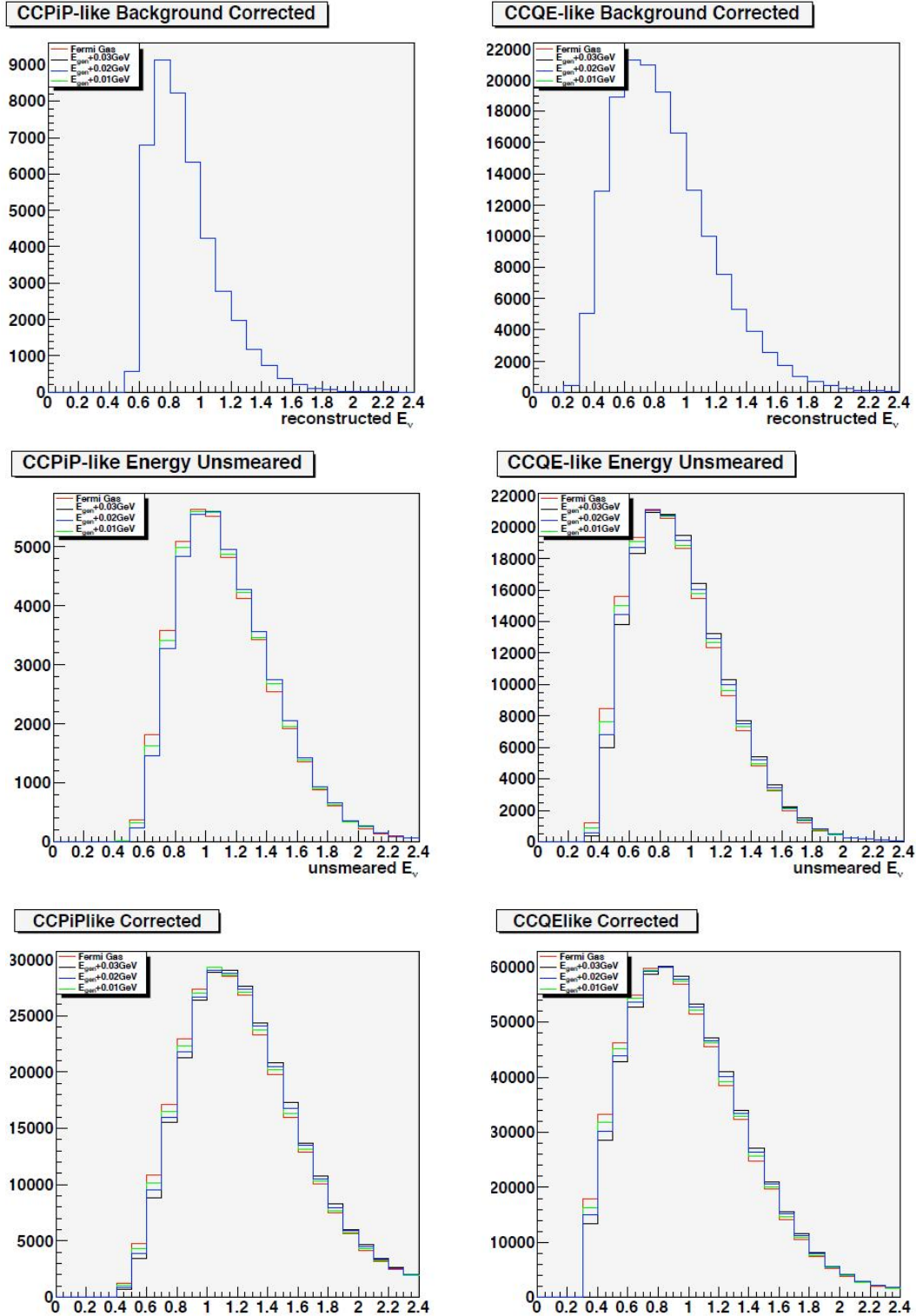


Figure 5.66: Background-corrected (top), unfolded (middle), and fully corrected (bottom) CC π^+ -like and CCQE-like distributions in reconstructed neutrino energy with standard Fermi gas model (red) and with Fermi Gas model shifted upward by 10 (green), 20 (blue), and 30 (black) MeV.

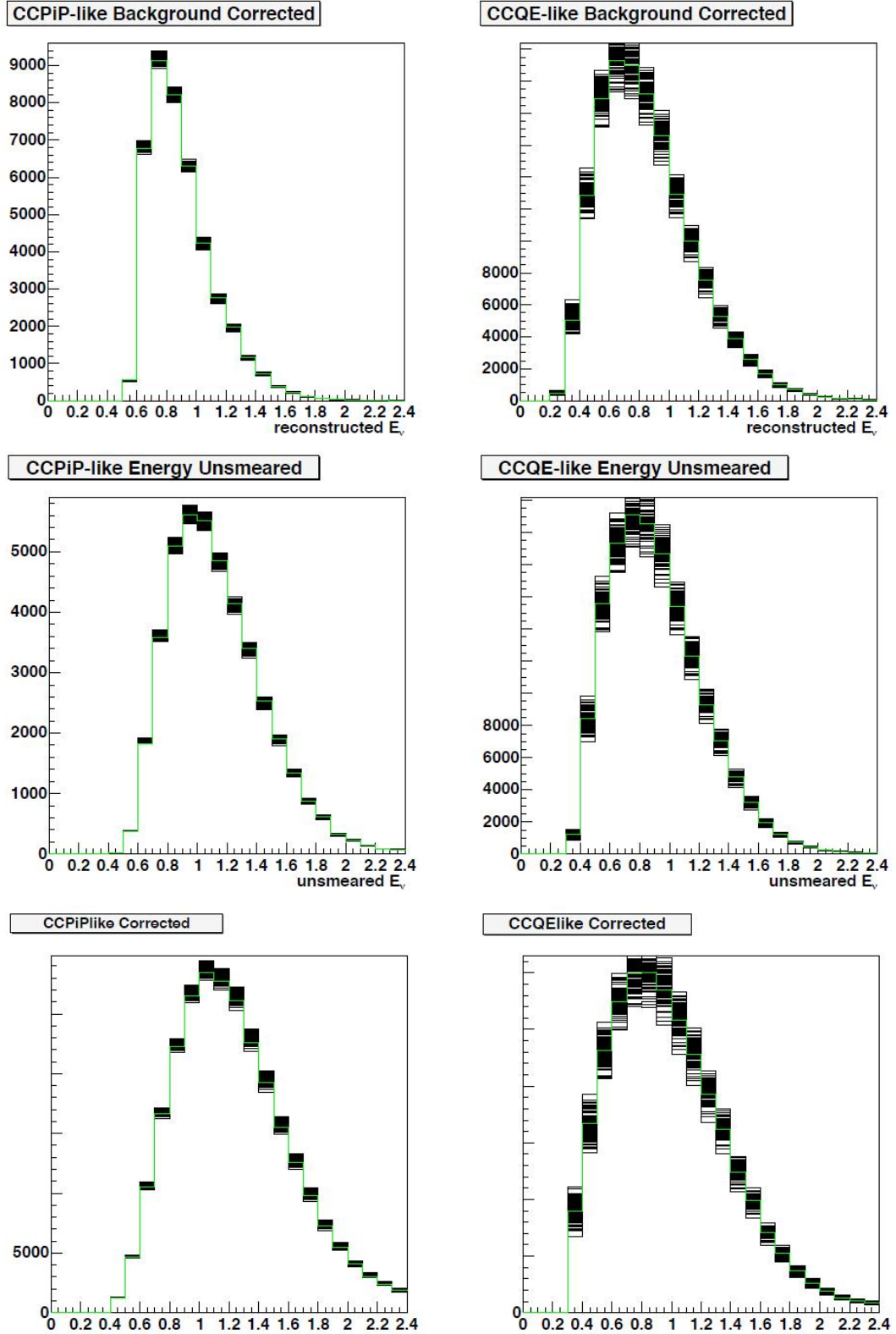


Figure 5.67: Background-corrected (top), unfolded (middle), and fully corrected (bottom) $CC\pi^+$ -like and $CCQE$ -like distributions in reconstructed neutrino energy, with cross-section multisim excursions.

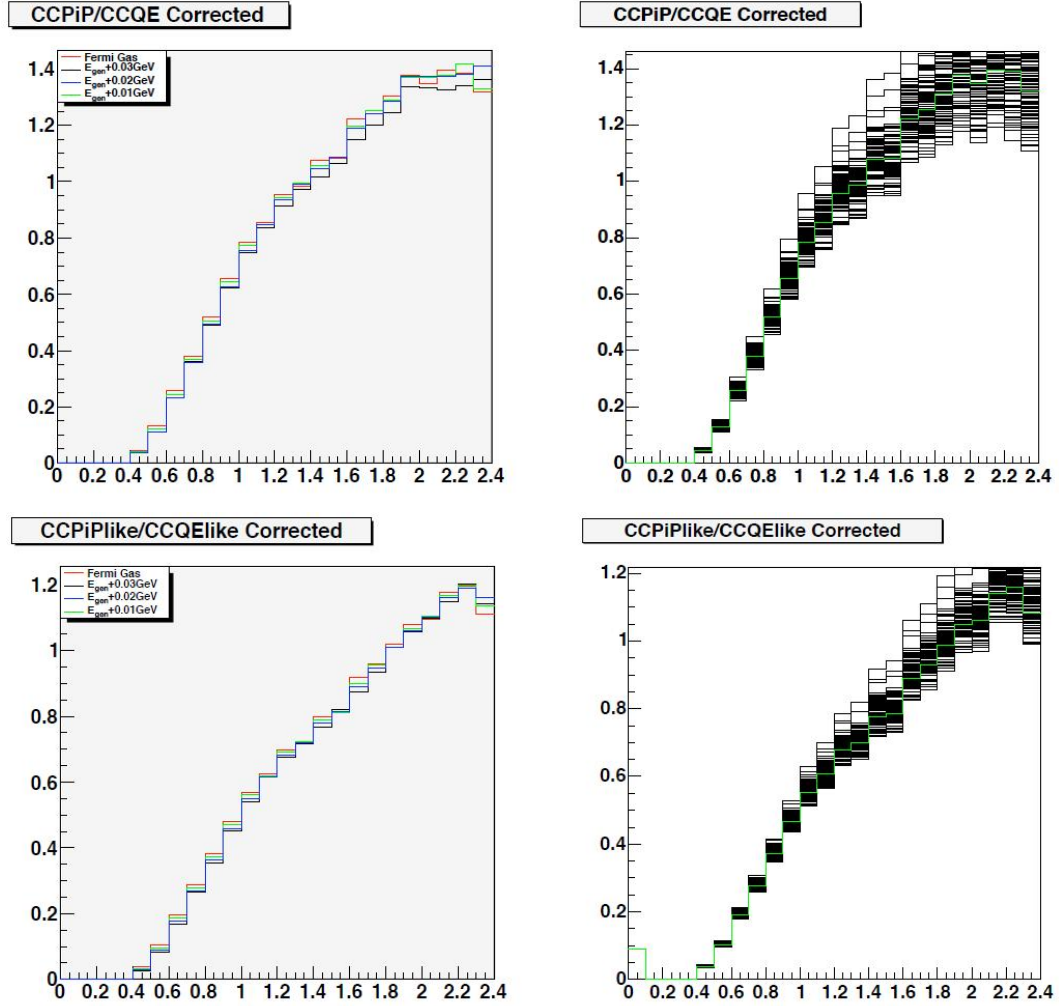


Figure 5.68: FSI-corrected (top) and observed (bottom) $CC\pi^+$ to $CCQE$ ratios with three versions of Fermi Gas model (left) and with cross-section multisim excursions (right).

measurement of both the effective and FSI-corrected ratios in each bin and with full error bars.

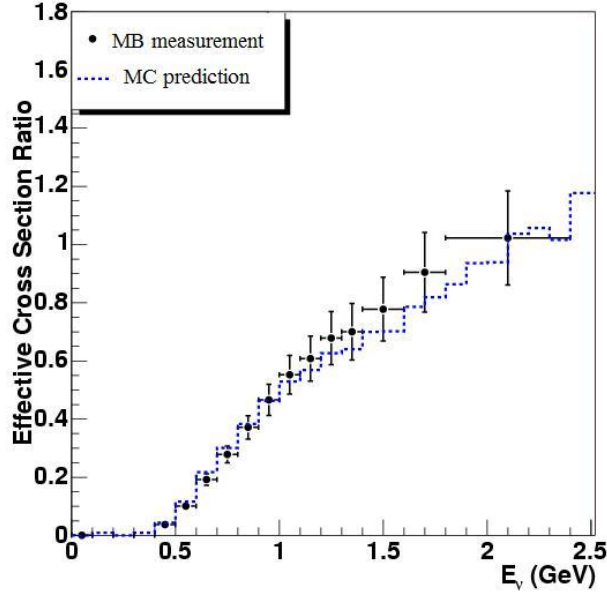


Figure 5.69: The effective $CC\pi^+$ to $CCQE$ ratio (black) compared with the NUANCE prediction (blue).

As figure 5.70 indicates, our result agrees to within errors with the both the ANL [55] and K2K [59] measurements. A rescaling of the K2K and MiniBooNE results was needed to make this comparison. The ANL measurement was on deuterium whereas K2K's was on C_8H_8 and ours was on CH_2 ; thus we have a proton to neutron ratio of 4:3 while ANL had 1:1 and K2K 7:6. Because $CCQE$ interactions can only occur on neutrons, while the dominant $CC\pi^+$ channel is on protons, we expect the $CC\pi^+$ to $CCQE$ ratio to depend on the proton to neutron ratio. Thus, to compare the three experiments, we have corrected the K2K and MB results to what they would be on a target with equal numbers of protons and neutrons. The scaling factor for K2K was taken from [59], where a similar comparison of the K2K and ANL results was made; their factor is 0.89. To obtain the scaling factor for MiniBooNE, we assume that the Monte Carlo accurately predicts the relative numbers of channel 3 (on a proton), channel 5 (on a neutron), and channel 97 (coherent) events. The scaling factor is then $\frac{3}{4}s_p + s_n + s_{coh}$ where s is the fraction of signal events in each

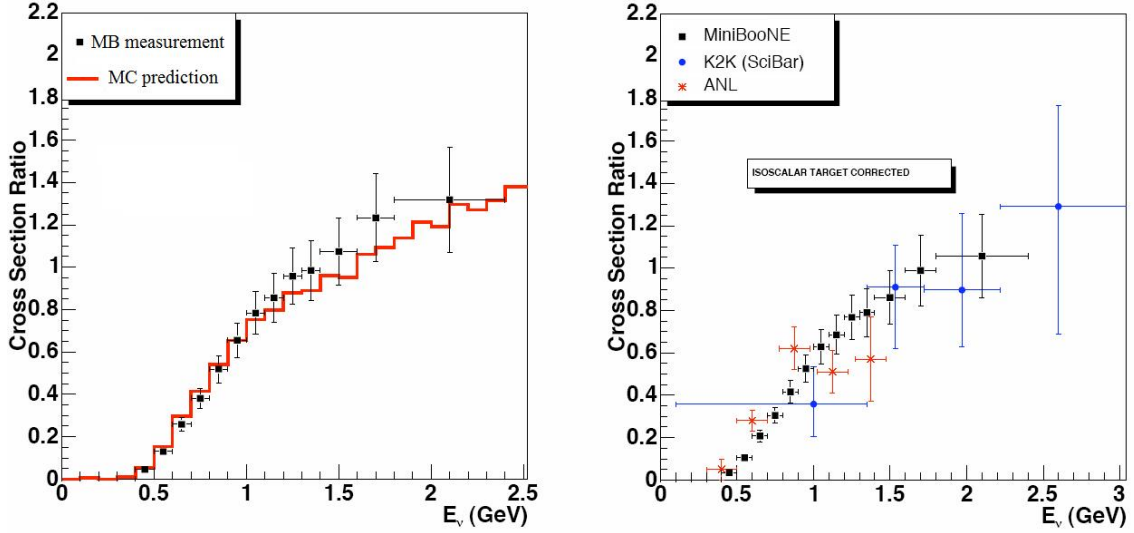


Figure 5.70: Left: Our $CC\pi^+$ to $CCQE$ ratio compared with the NUANCE prediction. Right: Our ratio compared with those measured by ANL and K2K. The MiniBooNE and K2K measurements have been rescaled for an isoscalar target to compare with ANL.

channel; the factor works out to 0.8. Note also that in the ANL measurement, an explicit cut on invariant mass $W < 1.4$ GeV was made. No cut on invariant mass was made in this analysis; however the MiniBooNE flux is such that $CC\pi^+$ events occur only in the region $W < 1.6$ GeV. Similarly, the the K2K measurement includes events in the region $W < 2$ GeV.

| E_ν (GeV) | CC1 π^+ /CCQE (FSI corrected) | CC1 π^+ -like/CCQE-like (observed) |
|------------------|--------------------------------------|---|
| 0.45 \pm 0.05 | 0.045 \pm 0.008 | 0.036 \pm 0.005 |
| 0.55 \pm 0.05 | 0.130 \pm 0.018 | 0.100 \pm 0.011 |
| 0.65 \pm 0.05 | 0.258 \pm 0.033 | 0.191 \pm 0.019 |
| 0.75 \pm 0.05 | 0.381 \pm 0.047 | 0.278 \pm 0.028 |
| 0.85 \pm 0.05 | 0.520 \pm 0.064 | 0.371 \pm 0.040 |
| 0.95 \pm 0.05 | 0.656 \pm 0.082 | 0.465 \pm 0.053 |
| 1.05 \pm 0.05 | 0.784 \pm 0.100 | 0.551 \pm 0.066 |
| 1.15 \pm 0.05 | 0.855 \pm 0.114 | 0.607 \pm 0.077 |
| 1.25 \pm 0.05 | 0.957 \pm 0.132 | 0.677 \pm 0.091 |
| 1.35 \pm 0.05 | 0.985 \pm 0.141 | 0.700 \pm 0.097 |
| 1.5 \pm 0.1 | 1.073 \pm 0.157 | 0.777 \pm 0.109 |
| 1.7 \pm 0.1 | 1.233 \pm 0.207 | 0.904 \pm 0.137 |
| 2.1 \pm 0.3 | 1.318 \pm 0.247 | 1.022 \pm 0.161 |

Table 5.7: The MiniBooNE measured $CC\pi^+$ to $CCQE$ (Figure 5.70) and $CC\pi^+$ -like to $CCQE$ -like (Figure 5.69) cross section ratios on CH_2 including all sources of statistical and systematic uncertainty.

Chapter 6

Conclusion

Charged current single pion production and charged current quasi-elastic scattering are the two most abundant event channels for neutrinos on the order of 1 GeV. This dissertation has presented a measurement of the ratio of the cross-sections for these two processes on mineral oil, as a function of neutrino energy. This measurement, made by the MiniBooNE experiment, represents an improvement of an order of magnitude in statistics over any previous $CC\pi^+$ or $CCQE$ measurement, and is the most precise determination of the cross-section ratio to date. This is also the first analysis to report results for observed ($CC\pi^+$ -like and $CCQE$ -like) events after final state interactions in addition to the FSI-corrected result. The observed result does not attempt to use a nuclear model to account for pion absorption and charge exchange within the target nucleus and thus it is more model-independent than the FSI-corrected result. It is also more precise, because uncertainties on intra-nuclear re-scattering do not enter into the systematic errors.

A comparison of this measurement with two previous measurements of the $CC\pi^+$ to $CCQE$ ratio was shown in figure 5.70. Several other experiments have measured $CC\pi^+$ and $CCQE$ cross-sections, but for simplicity we compare only with experiments that reported both cross-sections using the same binning. As can be seen from the plot, with this measurement we begin to clearly see the behavior of the cross-section ratio as a function of neutrino energy.

This measurement is an important step toward understanding neutrino cross-sections for these events at low energies, but it is only a beginning. Subsequent MiniBooNE measurements of absolute differential $CCQE$ [61] and $CC\pi^+$ [62] cross-sections have been published. The ratio of these results agrees with the cross-section ratio presented here, which is in good agreement with the Smith-Moniz and Rein-Sehgal models; however, both the $CCQE$ and $CC\pi^+$ absolute measurements find cross-sections on the order of 30% larger than the prediction from their respective model. This may suggest that there is some underlying reason, common to $CC\pi^+$ and $CCQE$, that the cross-section predictions are off. In any case, it is useful to have both the ratio measurement and the absolute cross-section measurements. Future results from SciBooNE, MINOS, MINER ν A, NO ν A, MicroBooNE, and other experiments promise to continue to improve our understanding of these interactions and may solve remaining puzzles such as the 30% discrepancy in both channels and the conflicting evidence for coherent pion production.

In the near-term, this result provides much-needed data for modelling resonant pion production by neutrinos and, in particular, for testing proposed improvements to the Rein-Sehgal model. Since its publication, several theorists and phenomenologists [100, 101, 102, 103, 104, 105, 106, 107] have used this measurement. Farther ahead, the result presented here will help to constrain the $CC\pi^+$ background to $CCQE$ in future ν_μ disappearance searches; it is thus a small step on the road toward answering the great open questions of neutrino physics.

Bibliography

- [1] J. Chadwick, *Nature* **129**, 312 (1932).
- [2] H. Bethe and R. Peierls, *Nature* **133**, 532 (1934).
- [3] E. Fermi, *Z. Phys.* **88**, 161 (1934).
- [4] F. Reines and C.L. Cowan, *Phys. Rev.* **113**, 273 (1959).
- [5] G. Danby *et al.*, *Phys. Rev. Lett.* **9**, 36 (1962).
- [6] K. Kodama *et al.*, *Phys. Lett.* **B504**, 218 (2001).
- [7] R.J. Davis *et al.*, *Phys. Rev. Lett.* **20**, 1205 (1968).
- [8] J.N. Bahcall, *Phys. Rev. Lett.* **12**, 300 (1964).
- [9] K.S. Hirata *et al.*, *Phys. Lett.* **B205**, 416 (1988).
- [10] R. Becker-Szendy *et al.*, *Phys. Rev.* **D46**, 3720 (1992).
- [11] Y. Fukuda *et al.*, *Phys. Lett.* **B433**, 9 (1998).
- [12] Y. Fukuda *et al.*, *Phys. Lett.* **B436**, 33 (1998).
- [13] K.S. Hirata *et al.* *Phys. Rev. Lett.* **63**, 16 (1989).
- [14] P. Anselmann *et al.*, *Phys. Lett.* **B285**, 376 (1992).
- [15] J.N. Abdurashitov *et al.*, *Phys. Lett.* **B328**, 234 (1994).

- [16] Q.R. Ahmad *et al.*, Phys. Rev. Lett. **89**, 011301 (2002).
- [17] B. Aharmim *et al.*, Phys. Rev. **C72**, 055502 (2005).
- [18] Y. Ashie *et al.*, Phys. Rev. Lett. **93**, 101801 (2004).
- [19] K. Ichikawa, J. Phys. Conf. Ser. **120**, 022004 (2008).
- [20] C. Kraus *et al.*, Eur. Phys. J. **C40**, 447 (2005).
- [21] V.M. Lobashev *et al.*, Nucl. Phys. Proc. Suppl. **91**, 280 (2001).
- [22] P. Minkowski, Phys. Lett. **B57**, 421 (1977).
- [23] M. Gell-Mann, P. Ramond and R. Slansky, in Supergravity, ed. by D. Freedman *et al.*, North Holland (1979).
- [24] D. Rein and L.M. Sehgal, Annals Phys. **133**, 79 (1981).
- [25] E.T. Osypowski, M.G. Olsson, and E.H. Monsay, Phys. Rev. **D17**, 2938 (1978).
- [26] V.V. Lyubushkin, K.S. Kuzmin, and V.A. Naumov, Mod. Phys. Lett. **A19**, 2815 (2004).
- [27] C. Berger and L.M. Sehgal, Phys. Rev. **D76**, 113004 (2007).
- [28] C. Berger and L.M. Sehgal, Phys. Rev. **D77**, 059901 (2008).
- [29] K.R. Graczyk and J.T. Sobczyk, Phys. Rev. **D77**, 053003 (2008).
- [30] J. Nowak and W. Metcalf, MiniBooNE Technical Note 260 (2008).
- [31] K.R. Graczyk and J.T. Sobczyk, Phys. Rev. **D77**, 053001 (2008).
- [32] S.K. Singh, L. Alvarez-Ruso, and M.F. Vicente-Vascas, Phys. Rev. **C57**, 2693 (1998).
- [33] O. Lalakulich and E.A. Paschos, Phys. Rev. **D71**, 074003 (2005).
- [34] E. Hernandez, J. Nieves, and M. Valverde, Phys. Rev. **D76**, 033005 (2007).

- [35] D. Rein and L.M. Sehgal, Nucl. Phys. **B223**, 29 (1983).
- [36] A. Kartavtsev, E.A. Paschos, and G.J. Gounaris, Phys. Rev. **D74**, 054007 (2006).
- [37] S. Hirenzaki, L. Alvarez-Ruso, L.S. Geng, M.J. Vicente-Vacas, Phys. Rev. **C75**, 055501 (2007).
- [38] J. Nieves, J.A. Amaro, E. Hernandez, and M. Valverde, Phys. Rev. **D79**, 013002 (2009).
- [39] M. Hasegawa *et al.*, Phys. Rev. Lett. **95**, 252301 (2005).
- [40] K. Hiraide *et al.*, Phys. Rev. **D78**, 112004 (2008).
- [41] A.A. Aguilar-Arevalo *et al.*, Phys. Rev. **B664**, 41 (2008).
- [42] A.A. Aguilar-Arevalo *et al.*, Phys. Rev. **D81**, 013004 (2010).
- [43] Y. Kurimoto *et al.*, arXiv:1005.0059v1 [hep-ex] (2010).
- [44] C.H. Llewellyn-Smith, Phys. Rept. **3**, 261 (1972).
- [45] R.A. Smith and E.J. Moniz, Nucl. Phys. **B43**, 605 (1972); *erratum: ibid.* **B101**, 547 (1975).
- [46] S. Barish *et al.*, Phys. Rev. **D16**, 3103 (1977).
- [47] D. Allasia *et al.*, Nucl. Phys. **B343**, 285 (1990).
- [48] N.J. Baker *et al.*, Phys. Rev. **D23**, 2499 (1981).
- [49] M. Pohl *et al.*, Nuovo Cimento **26**, 332 (1979).
- [50] T. Kitigaki *et al.*, Phys. Rev. **D28**, 436 (1983).
- [51] S.V. Belikov *et al.*, Z. Phys. **A320**, 625 (1985).
- [52] V.V. Ammosov *et al.*, Sov. J. P. Nuc. **23**, 283 (1992).

- [53] J. Campbell *et al.*, Phys. Rev. Lett. **30**, 335 (1973).
- [54] S. Barish *et al.*, Phys. Rev. **D19**, 2521 (1979).
- [55] G.M. Radecky *et al.*, Phys. Rev. **D25**, 1161 (1982).
- [56] P. Allen *et al.*, Nucl. Phys. **B264**, 221 (1986).
- [57] T. Kitigaki *et al.*, Phys. Rev. **D34**, 2554 (1986).
- [58] J. Bell *et al.*, Phys. Rev. Lett. **41**, 1008 (1978).
- [59] A. Rodriguez *et al.*, Phys. Rev. **D78**, 032003 (2008).
- [60] H.J. Grabosch *et al.*, Z. Phys. **C41**, 527 (1989).
- [61] A.A. Aguilar-Arevalo, Phys. Rev. **D81**, 092005 (2010).
- [62] M.J. Wilking, FERMILAB-THESIS-2009-1
- [63] A.A. Aguilar-Arevalo *et al.*, Phys. Rev. Lett. **98**, 231801 (2007).
- [64] A.A. Aguilar-Arevalo *et al.*, Phys. Rev. Lett. **103**, 111801 (2009).
- [65] T. Kobilarcik, J. Monroe, D. Finley, and H. Meyer, MiniBooNE-Technical-Note-87 (2003).
- [66] A.A. Aguilar-Arevalo *et al.*, Phys. Rev. **D79**, 072002 (2009).
- [67] A.A. Aguilar-Arevalo *et al.*, Nucl. Instr. Meth. **A599**, 28 (2009).
- [68] S.J. Brice *et al.*, Nucl. Instr. Meth. **A562**, 97 (2006).
- [69] S. Agostinelli *et al.*, Nucl. Instr. Meth. **A506**, 250 (2003).
- [70] R.J. Glauber, *Lectures in Theoretical Physics, Volume 1* (1959).
- [71] N.V. Mokhov *et al.*, MARS Code Developments, [nucl-th/9812038] (1998).
- [72] A. Ferrari, P.R. Sala, A. Fasso, and J. Ranft, CERN-2005-010.

- [73] J.R. Sanford and C.L. Wang, BNL Note 11299 (1967).
- [74] M. Catanesi *et al.*, Eur. Phys. J. C **52**, 29 (2007).
- [75] I. Chemakin *et al.*, Nucl. Phys. A **639**, 407 (1998).
- [76] F. Abe *et al.*, Phys. Rev. **D36**, 1302 (1987).
- [77] Y.D. Aleshin, I.A. Drabkin, and V.V. Kolesnikov, ITEP-80-1977 (1977).
- [78] T. Abbott *et al.*, Phys. Rev. **D45**, 3906 (1992).
- [79] J.V. Alleby *et al.*, CERN Report No. 70-12 (unpublished).
- [80] D. Dekkers *et al.*, Phys. Rev. **137**, B962 (1965).
- [81] T. Eichten *et al.*, Nucl. Phys. **B44**, 333 (1972).
- [82] R.A. Lundy *et al.*, Phys. Rev. Lett. **14**, 504 (1965).
- [83] G.J. Marmer *et al.*, Phys. Rev. **179**, 1294 (1969).
- [84] I.A. Vorontsov *et al.*, ITEP-88-011 (1988).
- [85] D. Casper, Nucl. Phys. Proc. Suppl. **112**, 161 (2002).
- [86] CERN Program Library Long Writeup W5013 (1993)
- [87] A.A. Aguilar-Arevalo *et al.*, Phys. Rev. Lett. **100**, 032301 (2008).
- [88] M. Gluck, E. Reya, and A. Vogt, Eur. Phys. J. C **5**, 461 (1998).
- [89] A. Bodek and U.K. Yang, AIP Conf. Proc. **670**, 110 (2003).
- [90] C. Zeitnitz and T. A. Gabriel, Nucl. Inst. Meth. **A349**, 106 (1994).
- [91] C. Ashery *et al.*, Phys. Rev. **C23**, 2173 (1981).
- [92] H. Meyer, MiniBooNE-Technical-Note-90 (2003).

- [93] D. Toptygin, MiniBooNE-Technical-Note-122 (2004).
- [94] R.B. Patterson, FERMILAB-THESIS-2007-19
- [95] A. Bazarko *et al.*, MiniBooNe-Technical-Note-144 (2004).
- [96] B.C. Brown *et al.* IEEE Nuclear Science Symposium Record 1, 652 (2004).
- [97] CERN Program Library entry **D506**. Available at <http://wwwasdoc.web.cern.ch/wwwasdoc/minuit/minmain.html>.
- [98] G. D'Agostini, Nucl. Instr. Meth. **A362**, 487 (1995)
- [99] O. Benhar and D. Meloni, Phys. Rev. **D80**, 073003 (2009).
- [100] T. Leitner and U. Mosel, Phys. Rev. **C81**, 064614 (2010).
- [101] M. Martini, M. Ericson, G. Chanfray, and J. Marteau, Phys. Rev. **C80**, 065501 (2009).
- [102] M. Martini *et al.*, Phys. Rev. **C81**, 045502 (2010).
- [103] M. Antonello *et al.*, Acta Phys. Polon. **B40**, 2519 (2009).
- [104] K.M. Graczyk, D. Kielczewska, P. Przewlocki, and J.T. Sobczyk, Phys. Rev. **D80**, 093001 (2009).
- [105] M. Sajjad Athar, S. Chauhan, and S.K. Singh, J. Phys. **G37**, 015005 (2010).
- [106] M. Sajjad Athar, S. Chauhan, and S.K. Singh, Eur. Phys. J. **A43**, 209 (2010).
- [107] C. Juszczak, J.T. Sobczyk, and J. Zmuda, arXiv:1007.2195v1 [nucl-th] (2010).